Front cover: Temperature profile during the first mass transfer episode in a simulation of the core-degenerate scenario.

Back cover: The development of a detonation in a direct collision between a helium-core white dwarf and a carbon-oxygen one. Clockwise from top-left: density, temperature, and titanium and iron abundances.

Gabriela Aznar Siguan

UNIVERSITAT POLITÈCNICA DE CATALUNYA

INSTITUT D'ESTUDIS ESPACIALS DE CATALUNYA

PhD Thesis

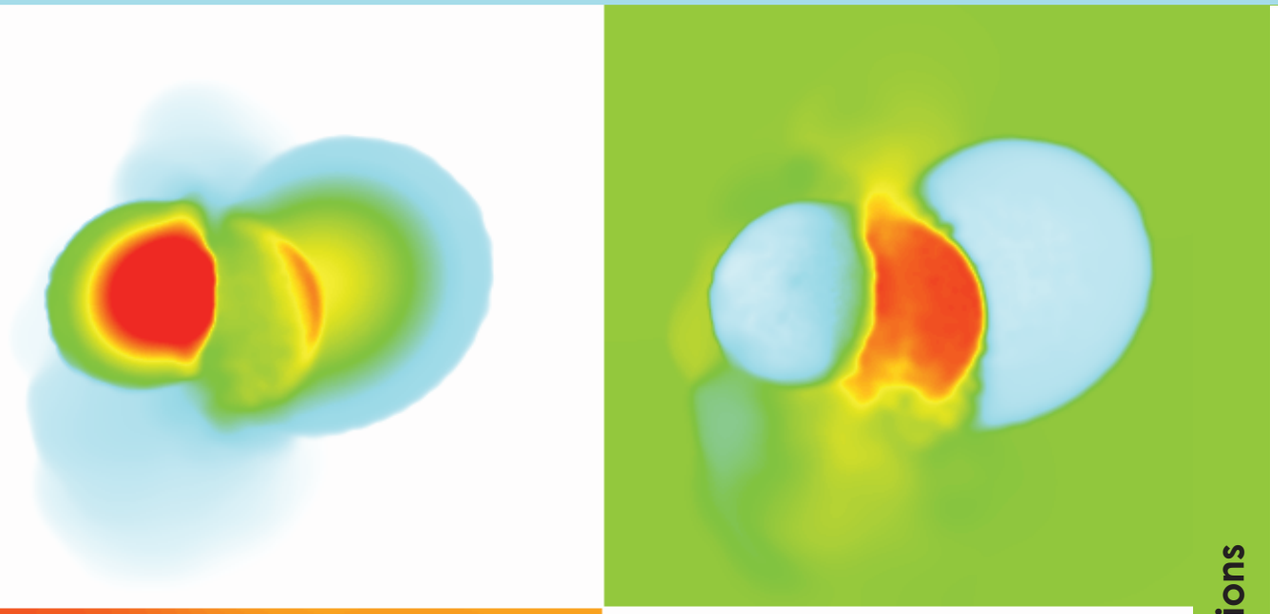

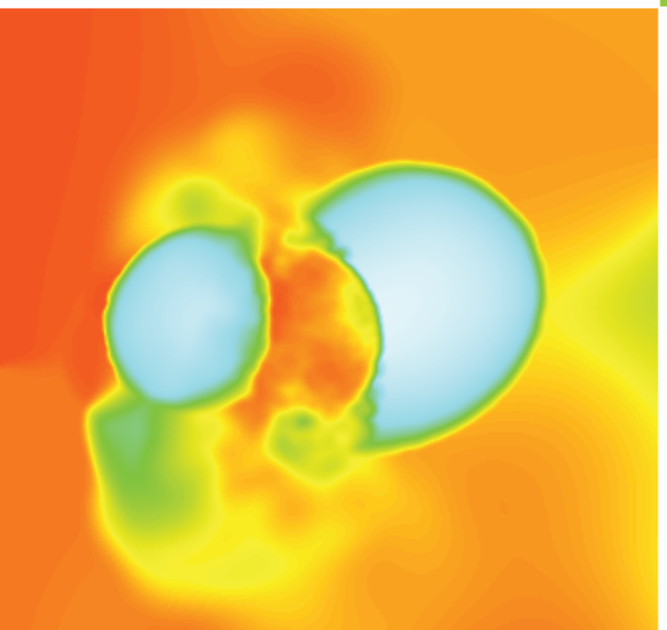

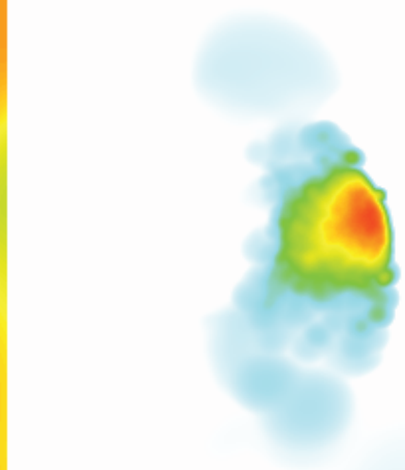

WHITE DWARF DYNAMICAL INTERACTIONS

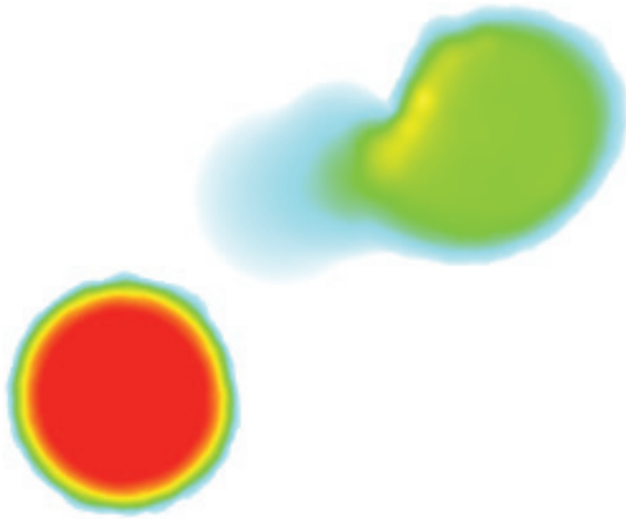

Gabriela Aznar Siguan

White dwarf dynamical interactions

Universitat Politècnica de Catalunya
Departament de Física Aplicada

White dwarf

dynamical interactions

by

Gabriela Aznar Siguan

A thesis submitted fot the degree of Doctor of Phylosophy

Advisors:
Enrique García–Berro Montilla
Pablo Lorén Aguilar

Castelldefels, Enero de 2015

UNIVERSITAT POLITÈCNICA DE CATALUNYA
BARCELONATECH
Escola de Doctorat

Curso académico:

Acta de calificación de tesis doctoral

Nombre y apellidos

Programa de doctorado

Unidad estructural responsable del programa

Resolución del Tribunal

Reunido el Tribunal designado a tal efecto, el doctorando / la doctoranda expone el tema de la su tesis doctoral titulada _____

_____.

Acabada la lectura y después de dar respuesta a las cuestiones formuladas por los miembros titulares del tribunal, éste otorga la calificación:

☐ NO APTO ☐ APROBADO ☐ NOTABLE ☐ SOBRESALIENTE

(Nombre, apellidos y firma) Presidente/a		(Nombre, apellidos y firma) Secretario/a
(Nombre, apellidos y firma) Vocal	(Nombre, apellidos y firma) Vocal	(Nombre, apellidos y firma) Vocal

_____, _____ de _____ de _____

El resultado del escrutinio de los votos emitidos por los miembros titulares del tribunal, efectuado por la Escuela de Doctorado, a instancia de la Comisión de Doctorado de la UPC, otorga la MENCIÓN CUM LAUDE:

☐ SÍ ☐ NO

(Nombre, apellidos y firma) Presidente de la Comisión Permanente de la Escuela de Doctorado	(Nombre, apellidos y firma) Secretario de la Comisión Permanente de la Escuela de Doctorado

Barcelona a _____ de _____ de _____

Summary

Because of their well known observational properties Type Ia, or thermonuclear, supernovae are used as standard candles, and have allowed the discovery of the accelerating expansion of the Universe. Yet, despite their importance, we still do not know exactly which stellar systems produce them. However, we do know the physical mechanism that powers the explosion. Type Ia supernovae originate from the explosion of carbon-oxygen white dwarfs. It has long been suggested that a white dwarf in a binary system — with either another white dwarf, through the so-called double-degenerate channel, or a main-sequence or red giant companion through the single-degenerate channel — could give rise to a Type Ia supernova event. Yet, despite the recent breakthrough detections of relatively nearby SNe Ia, including 2011fe and 2014J, no normal stellar progenitor has ever been directly identified. Overall, the challenging, unsolved stellar progenitor problem for SNe Ia stands in marked contrast to the case of core-collapse supernovae, whose stellar progenitors are highly-luminous, massive stars. Observational evidence favors the double-degenerate channel, but significant discrepancies exist between observations and theory. There are approximately a few hundred million double white dwarf systems in the Milky Way alone and their study would help to establish whether one can produce sufficient type Ia supernovae via this route. Nevertheless, even if a white dwarf merger does not succeed in exploding, other interesting phenomena might result. R Coronae Borealis, magnetars and high-field magnetic white dwarfs, could be the product of white dwarf mergers.

In this work we simulate and study several scenarios which involve interacting white dwarfs. One of the classical scenarios is the double-degenerate one, in which the merger of both white dwarfs in the binary system occurs after gravitational radiation has brought the stars close enough to overflow the Roche lobe. In this case a circular orbit with synchronized stars is the expected initial configuration of the interaction. However, other mechanisms that make two white dwarfs interact exist that have not been carefully studied. We first consider the so-called core-degenerate scenario, in which both white dwarfs merge just at the end of the common envelope phase. In this case the merger is driven by the interaction with the circumbinary disk resulting from previous evolution. Within this scenario the transfer of angular momentum from the binary to the disk decreases the separation of the pair whilst the eccentricity of the system increases. This results in an eccentric binary system in which the core

of the AGB star is hot. Secondly, we study close encounters of two white dwarfs in dense stellar environments, like the cores of old globular clusters or the central regions of galaxies. In some cases these close encounters lead to collisions. We analyze how the different initial conditions change the type of interaction obtained, the outcome of such interactions and the characteristics of the remnants. We also study the observational imprints of these interactions. These include the emission of gravitational waves, the X-ray luminosities, the thermal neutrino emission and the bolometric light curves. Finally, we analyze two possible outcomes of the merger of white dwarfs. Namely, we study if a merger of two white dwarfs can produce high-field magnetic white dwarfs or anomalous X-ray pulsars.

I have hardly ever known a mathematician who was able to reason.

Stephen Hawking

Acknowledgments

Decidí empezar la tesis doctoral después de haber realizado el proyecto final de máster bajo la supervisión de los doctores Enrique García-Berro Montilla y Pablo Lorén Aguilar. Tal y como dijo Enrique entonces, la colaboración en investigación es como un noviazgo. En mi caso fue así, una vez conocidos decidimos formalizar y continuar la relación durante cuatro años más. Fruto de esta relación ha sido diversos artículos científicos y nuevos caminos abiertos para una eventual investigación futura. Aunque yo considero que he aprendido mucho de Pablo y Enrique, Enrique todavía opina que no ha conseguido hacerme superar mis prejuicios matemáticos. Creo que no he llegado a formar parte de los pocos matemáticos a los que se refiere Stephen Hawking, sobre todo porque no he tenido el placer de conocerlo, sin embargo tengo la sensación de que gracias a vosotros el razonamiento físico me ha quedado mucho más al alcance. Debo agradeceros a los dos la dedicación y el interés que me habéis prestado. Muchísimas gracias Enrique y Pablo.

También me gustaría agradecer a los doctores Santiago Torres y Jorge Rueda por haberme permitido colaborar con ellos. El Dr. Torres puso a mi disposición los cálculos de síntesis de poblaciones que se detallan en el capítulo dedicado a las enanas blancas con campos magnéticos elevados. El Dr. Rueda me inició en el estudio de los púlsares anómalos de rayos X. Sin la ayuda de ambos esta tesis sería imcompleta.

I would like to thank doctor Stephan Rosswog and its computational high-energy astrophysics group of the Stockholm University the warm welcome they offered me during my stay. I really enjoyed the weekly meetings and interesting talks about astrophysics that I witnessed and held. Thank you very much Stephan, Oleg, Iván and Emilio. I hope to see you again. También estoy muy agradecida a Illa, una buena amiga que hizo mi estancia más agradable.

During this time we have collaborated with the nice group from the University of Massachusetts Dartmouth of doctor Robert Fisher. I liked to get to know you in Cefalù, Rahul and Robert, and hope to keep in touch. I also owe my gratitude to doctor Noam Soker, it was very interesting to listen to you in Cefalù and to work with you.

Aquesta feina desenvolupada durant tants anys s'ha dut a terme rodejada d'una molt bona companyia. Aïllats del món, a Castelldefels hi ha un despatx de doc-

torands del departament de física aplicada molt ben avingut. Especialment valoro haver conegut a unes amigues amb les que he compartit molts bons i mals moments, i en tots ells, elles sempre s'han comportat superant les meves expectatives. Gràcies Anna, Estel, Ruxandra, Araceli i Maria. Juntament amb el Fran, el Milad, el Charlie, el Shervin, el Fugqiang i la Isa hem aconseguit estar ben entretinguts. Impartir classes amb els bons professors d'aquesta secció també ha estat un plaer. I poder haver consultat dubtes als sempre propers astrofísics Jordi i Pilar m'ha ajudat molt, gràcies. També les lliçons informàtiques que m'han donat el Toni i el Jordi m'han resultat molt útils, gràcies també.

Ara és el torn de referir-me a les amistats més properes. Amb aquest parell de línies no puc expressar tota la felicitat i gratitud cap a vosaltres, sinó que espero que seguim alimentant aquesta relació dia a dia durant moltíssims anys més. Estic molt contenta de poder contar amb la bona amistat dels meus amics de mates. Sense els dinars del mes aquests anys no haurien estat el mateix. Només vosaltres sou capaços d'inventar una tradició com aquesta, serà que sí que som diferents. Laura, tu sempre em sorprens quan menys m'ho espero. Desitjo que també sigui així en un any i poguem conviure a Madrid. Les meves grans amigues del cole també mereixen una menció especial, Laura, Anna, Cris i Marta. Aprecio molt la vostra incondicional amistat. Va especialment per tu, Laura.

Puc considerar que ets casi de la família, Sarah. I agraint-te a tu el teu suport, vull començar el reconeixament cap a la meva estimada família. Tengo mucho que agradeceros a todos y cada uno. Cuando el abuelo me dijo que acabaría calculando órbitas de la basura espacial probablemente despertó en mí una curiosidad que ahora empieza a reflejarse en mis decisiones profesionales. El carácter alemán al que tanta referencia hace mi tutor Enrique se lo debo y agradezco a la abuela. A los tetes les debo la visión alegre de vivir la vida. La yaya ya decía que no era bueno trabajar tanto, tal y como hacían mis padres. Anabel y José me han ayudado mucho con sus consejos y bibliografía a adentrarme en el mundo aeroespacial. Y Jordi siempre ha estimulado nuestras ganas de saber con sus preguntas y sus regalos del museo de la ciencia. Agradezco a Toña y a la tía todo su cariño y apoyo. También al tío Pedro su muestra de disciplina. Manolita siempre ha estado dispuesta a enseñarme, desde coser y jugar al póquer hasta francés, y alimentarme. Así como también ha sido alimentado y querido Drapp por Enrique. También he aprendido de mis primos pequeños pero grandes, Marina y Miguel. Espero que Miguel en cambio no haya aprendido demasiado de mí y siga una exitosa trayectoria en físicas, incluso en física teórica. Mis primas Judit y Melina nos hicieron de canguro a Andrés y a mí cuando éramos pequeños, y les agradezco muchísimo que lo sigan haciendo. Finalmente, a quien más agradezco que todo haya salido bien, o lo mejor posible, es a mis padres y a mi hermano. Cuando Andrés no ha estado chinchándome, en él siempre he podido encontrar a mi mejor amigo. Y a Marisa y Eduardo les agradezco muchísimo sus consejos, su apoyo, su cariño y su absoluta disposición para escuchar y ayudar.

Contents

List of Figures

List of Tables

Chapter 1

Introduction

A large fraction of stars belong to binary systems or, more generally, to multiple systems. A substantial number of these binary systems are so close that at a given time of their lifes a mass transfer episode will occur. This process influences the structure of both stars and their subsequent evolution. While the exact numbers are still somewhat uncertain, large surveys suggest that the percentage of interacting binaries ranges between 30% and 50%. Besides, in triple star systems the inner binary orbit can be perturbed in such an extent that detached binaries may eventually become interacting. Moreover, in dense stellar systems single stars pass very close each other. This occurs, for instance, in old globular clusters and galactic nuclei. In globular clusters, where the density of stars is roughly a million times that of the Solar neighborhood, stellar collisions are rather frequent (Hills & Day, 1976). Actually, it has been predicted that up to 10% of the stars in the core of typical globular clusters have undergone a collision at some point during the lifetime of the cluster (Davies, 2002). Also galactic nuclei, which harbor massive black holes, like that of our own Galaxy, have stellar densities at least as large as those found in the center of the densest globular clusters. In these environments the frequency of stellar collisions is largely enhanced, since, due to the strong attraction of their central black holes, stars have much larger velocities.

The study of the interactions between two white dwarfs has received considerable interest in the last 30 years, since it has been shown that, under certain circumstances, the result of such interactions could be a Type Ia supernova outburst (Webbink, 1984; Iben & Tutukov, 1984). Supernovae are stellar explosions that radiate as much energy as any ordinary star is expected to emit over its entire life span, outshining briefly the whole hosting galaxy. They enrich the interstellar medium with higher mass elements and the resulting expanding shock triggers the formation of new stars. Additionally, Type Ia supernovae have been successfully used as standardizable distance candles, providing solid evidence for an accelerating Universe. Observational findings are consistent with the assumption that supernovae Ia are

the result of thermonuclear disruptions of carbon-oxygen white dwarfs (Hillebrandt et al., 2013). However, the many uncertainties remain still unsolved. The most important ones are the exact explosion mechanism, and the formation channels leading up to the explosion. The fact that peculiar sub-classes of Type Ia supernovae have been discovered in recent years, suggests that different progenitors and/or explosion mechanisms are able to trigger them. Generally speaking there are two main progenitor scenarios. Either the carbon-oxygen white dwarf accretes material from a non-degenerate companion, known as the single degenerate scenario, or from an other white dwarf, the double degenerate scenario. The white dwarf might accrete mass until reaching the Chandrasekhar mass limit, or a sub-Chandrasekhar system might result in a supernovae by the double detonation mechanism, which involves accretion of helium-rich material (Livne, 1990; Fink et al., 2007). When confronted by observation, the relatively well-explored single degenerate scenario faces several challenges, as the absence of a stellar ex-companion, whilst some constraints, as the delay-time distribution, favor the double degenerate scenario. Furthermore, sub-Chandrasekhar double degenerate scenarios are needed to fit the supernovae Type Ia rate from white dwarf mergers in the Milky Way-like Sbc galaxies (Badenes & Maoz, 2012).

Up to the moment, the effort of producing Type Ia supernovae in white dwarf interactions has been only partially successful, and only under certain circumstances a powerful detonation ensues. This depends on the properties of the dynamical merging phase in prompt explosions or on the subsequent evolution of the final remnant, in the rest of the cases. Even if dynamical interactions fail in producing a supernova outburst, they can still be responsible of some other interesting phenomena. For instance, since the temperatures achieved in some interactions is substantially high, and some material could be ejected from the binary system, the nuclearly processed material ejected during the interaction could pollute the surrounding environment. Besides, double white dwarfs with non-zero eccentricities, are powerful sources of gravitational waves (Willems et al., 2007), and could be eventually detected by spaceborne observatories (Lorén-Aguilar et al., 2005). The detection of gravitational waves from coalescing binaries at cosmological distances is important not only because it would provide a major new corroboration of Einstein's theory of General Relativity, but also because accurate independent measurements of the Hubble constant and mean density of the Universe could be obtained. Finally, the remnant of the interaction could lead to the formation of magnetars (King et al., 2001), hydrogen-defficient carbon-rich stars and R Coronae Borealis stars (Izzard et al., 2007; Clayton et al., 2007; Longland et al., 2011), could also be at the origin of high-field magnetic white dwarfs (Wickramasinghe & Ferrario, 2000; García-Berro et al., 2012), and could explain some of the characteristics of soft γ-ray repeaters (SGRs) and of anomalous X-ray pulsars (AXPs) (Malheiro et al., 2012). Also, some hot and massive white dwarfs members of the Galactic halo could be the result of the coalescence of a double white dwarf binary system (Schmidt et al., 1992; Segretain

et al., 1997).

All in all, it seems clear that for multiple reasons the interactions of two white dwarfs is a subject that deserves to be studied in detail. In this work we study two scenarios that differ from the classical double-degenerate one. We first consider the core-degenerate scenario, where both white dwarfs merge just at the end of the common envelope phase, due to the interaction with the circumbinary disk formed during the previous evolution of the system. In a second step we perform a deep study of the close encounters of two white dwarfs in dense stellar environments, like the cores of old globular clusters or the central regions of galaxies. In some cases these close encounters lead to collisions. We analyze how the different initial conditions change the type of interaction obtained, the outcome of such interactions and the characteristics of the remnants. We also study the observational imprints of these interactions. These include the emission of gravitational waves, the X-ray luminosities, the thermal neutrino emission and the bolometric light curves. Finally, we analyze two possible outcomes of the merger of white dwarfs. Namely, we study if a merger of two white dwarfs can produce high-field magnetic white dwarfs or anomalous X-ray pulsars. The calculations presented in this work have been done using Smoothed Particle Hydrodynamics. Our code has been used previously to simulate similar scenarios, has proven to be well suited for our purposes. The main characteristics of this code can be found in Appendix A.

1.1 The core-degenerate scenario

In a low-mass or intermediate-mass binary system, typically the more massive (primary) component fills its Roche lobe while traversing the Hertzsprung gap in the Hertzsprung-Russell diagram and mass transfer is stable to the companion. The primary star then evolves into a carbon-oxygen white dwarf. Later, the initially secondary star fills its Roche lobe when it is an evolved star. This time the combination of a deep convective envelope and an extreme mass ratio causes an unstable mass transfer to the white dwarf and a common envelope ensues. When the common envelope is dispersed, a final binary system made of two white dwarfs is obtained. Normally, in this case the second white dwarf formed is the more massive one (Webbink, 1984). Gravitational wave radiation finally brings both white dwarfs closer and a merger starts. All this sequence of events is known as the the double-degenerate scenario. However, it might be also possible that at the final stages of the common envelope phase, $\sim 1 - 10\%$ of the ejected envelope remains bound to the post-AGB core and the companion white dwarf, forming a circumbinary disk (Sandquist et al., 1998; De Marco et al., 2011; Kashi & Soker, 2011). The interaction of the circumbinary disk with the binary system will reduce the orbital separation, favoring a merger at the end of the common envelope phase, or a short time after, during the planetary nebula phase, while the core is still hot. This is known as the core-degenerate

scenario (Livio & Riess, 2003; Kashi & Soker, 2011; Ilkov & Soker, 2012, 2013).

Note, however, that there are two significant differences between the double- and the core-degenerate scenarios. In a double-degenerate merger both white dwarfs are brought together by gravitational wave radiation, a process which lasts for long timescales. Consequently, it is expected that both components of the binary system are cool, and have nearly circular orbits. Moreover, it is also foreseen that both white dwarfs will be synchronized. In contrast, in the core-degenerate scenario the merger of both stars is triggered by the interaction with the circumbinary disk. Consequently, it turns out that in a sizable number of cases as the binary system transfers angular momentum to the circumbinary disk, the separation of the pair decreases and the eccentricity of the system increases (Artymowicz et al., 1991) while the core is still hot (Kashi & Soker, 2011). However, it might be also possible that, if the circumbinary disk is not massive enough, the merger takes place after the circumbinary disk has been already ejected. In this case the driver of the merger is again the emission of gravitational waves, so the orbits will have a small eccentricity and the temperature of the core of the post-AGB star will be low. In summary, in the core-degenerate scenario a considerably large range of eccentricities of the binary system and of temperatures of the naked core of the AGB star are expected, at odds with what it is foreseen for the double-degenerate channel.

None of the scenarios described so far specifies at which evolutionary stage the explosion takes place. In violent mergers, while the merger is still ongoing, a prompt thermonuclear explosion might occur (Pakmor et al., 2010; Dan et al., 2014; Moll et al., 2014). However, for double-degenerate mergers powerful explosions only occur when both white dwarfs are relatively massive ($M \gtrsim 0.8\,M_{\odot}$), and the mass ratio is close to one. In the rest of the cases, very long delays from merger to explosion are expected, if it finally occurs. For instance, it has been proposed that rapid rotation keeps the remnant structure overstable (Tornambé & Piersanti, 2013). Also, it has been shown that in some cases accretion induced collapse cannot be avoided (Saio & Nomoto, 1985). Finally, it is worth mentioning that in general the remnant of the white dwarf merger can have a mass larger that the Chandrasekhar limiting mass (Webbink, 1984; Iben & Tutukov, 1984), leading to a normal Type Ia supernovae, whereas in other cases sub-Chandrasekhar mergers can also lead to a delayed Type Ia supernovae (van Kerkwijk et al., 2010).

All this results hold for the double-degenerate scenario. To this regard, it is important to realize that while several simulations of the double degenerate progenitor channel have been already performed over the last two decades, no full three-dimensional simulation of the core degenerate scenario has been done so far. One of the aims of the present work is to study the merger events within the core-degenerate scenario. More specifically, it would be desirable to study how the initial conditions affect the evolution of the merger process and the final characteristics of the merger remnant. All this is examined in the second chapter of this work.

1.2 White dwarf collisions

In contrast to the classical double-degenerate scenario and the core-degenerate scenario, a collision of two white dwarfs may be at the origin of some Type Ia supernovae. This type of interactions can be the result of either a serendipitous approach due to the high stellar density of the considered stellar system or the result of the interaction of a binary system containing two white dwarfs and a third star in a triple or multiple system. For example, the so-called Kozai-Lidov mechanism in triple systems can increase the eccentricities of the orbits. This caused by the perturbation from highly inclined tertiaries (perturbers) in hierarchical triple systems (Kozai, 1962). The details of how the intervening stars are brought close enough to experience such dynamical encounters do not play an important role in the result of the interaction, so the outcome of the interaction is independent of these details, and the gross features of the hydrodynamical evolution are totally general.

In most cases stellar interactions change the characteristics of the colliding stars. This is true not only for the masses of the interacting stars, but also the dynamical interaction affects the evolutionary state of the intervening stars, hence its type (Colgate, 1967). In addition, large amounts of energy can be released directly or indirectly during and after the collision. Thus, stellar collisions are important for understanding the evolution of both the total luminosity and the luminosity function of dense stellar clusters (Shara & Shaviv, 1977). Shara & Shaviv (1977) were the first to simulate a collision involving a white dwarf. Specifically, they studied the interaction of a white dwarf and a main-sequence star. They simulated head-on collisions in two dimensions using a grid-based method and modelling the white dwarf as a point mass. Later, Soker et al. (1987) improved and extended these preliminary calculations performing full three-dimensional off-axis collisions using a pseudo-particle method. They showed that a wide range of encounters resulted in the formation of a massive disk around the white dwarf. This was the same result obtained by Benz et al. (1989), who studied the case of collisions between two white dwarfs. Benz et al. (1989) used a Smoothed Particle Hydrodynamics code with a resolution of only 5,000 particles. The increased numerical resolution available by Rosswog et al. (2009) and the advanced techniques used in their work showed that the head-on collisions of Benz et al. (1989) were explosive. They obtained no bounded remnant and lightcurves and spectra that resemble Type Ia supernovae. Since then, the study of white dwarf collisions has received a renewed interest.

In the present work we perform simulations of a post-capture scenario of a white dwarf system. Therefore, our orbits are always elliptical, in contrast to the most simulated cases, for which parabolic or hyperbolic trajectories (Raskin et al., 2009, 2010) were adopted. Besides, most authors have studied the collision of two white dwarfs with fixed masses. This, for instance, was also the approach adopted by Lorén-Aguilar et al. (2010), where the masses of the intervening white dwarfs ($0.6\,M_{\odot}$ and $0.8\,M_{\odot}$) were kept fixed, while their initial relative velocity and distance were varied.

They found that the outcome of the interaction could be either a direct collision, a lateral one, or could be the formation of an eccentric binary system. Nevertheless, these outcomes depend on the masses (and on the core chemical composition) of the interacting white dwarfs. Here, we pay more attention to study the effects of the masses of the interacting stars, covering a broad range of masses and initial conditions. The results of our study are explained in chapter 3.

Chapter 4 of the present thesis is devoted to study the observational signatures of the dynamical interactions presented in chapter 3. This is a sorely needed study that, besides of its intrinsic importance, it has never been undertaken before. This is in contrast with the case in which two neutron stars merge or collide — see, for instance, (Rosswog et al., 2013), and references therein — for which a considerable deal of work has been done on describing the observational outcomes. It is worth pointing out that, quite naturally, large efforts have been invested in modelling the dynamical evolution of white dwarf mergers, while little attention has been paid to scrutinize its observational manifestations. In this thesis we aim at filling this gap by computing the gravitational waveforms, the corresponding light curves for those events in which some ^{56}Ni is synthesized, the associated emission of neutrinos, and the X-ray luminosity of the fallback material. All of them individually, or used in combination, would hopefully allow us to obtain useful information about these events.

The emission of gravitational waves in these iteractions should be quite apparent, given that the two interacting white dwarfs are subject to large accelerations, and that in most of the situations there is no symmetry. Although gravitational waves have not been yet detected, with the advent of the current generation of terrestrial gravitational wave detectors and of space-borne interferometers, it is expected that the first direct detections will be possible in a future. In particular, much hope has been placed on the space-based interferometer eLISA, a rescoped version of LISA, which will survey for the first time the low-frequency gravitational wave band (from $\sim$0.1 mHz to $\sim$1 Hz). The timescales of the close encounters of two white dwarfs correspond precisely to this frequency interval. Also, for those events in which an explosive behavior is found it is clear that some information about the dynamical interactions could be derived from the analysis of the light curves. On the other hand, neutrino emission in these events should be noticeable, given the relatively high temperatures achieved during the most violent phases of the interaction ($\sim 10^9$ K), and an assessment of their detectability is lacking. Finally, the X-ray luminosity of the fallback material interacting with the disk resulting in the aftermath of the interactions would also eventually help in identifying these events.

1.3 Remnants of the interactions

In those interactions which result in the merger of both white dwarfs and a bounded remnant is obtained, its subsequent evolution might end up in different observed astrophysical objects.

1.3.1 High-field magnetic white dwarfs

GRW+70 8247 was the first magnetic white dwarf ever discovered. First, it was determined to be a white dwarf by Kuiper (1934), turning out to be the fifth or sixth white dwarf identified. Four years later Minkowski (1938) was the first to point out its peculiar nature, when he noted the presence of broad shallow absorption features in its blue spectrum which could not be identified with known atomic or molecular transitions, the strongest occurring at 4,135 Å. It was not until 1970 that Kemp et al. (1970) discovered that the continuum radiation was strong circularly polarized, at an unprecedent level in any known astronomical object at that time, thereby establishing its magnetic nature. By the year 2000, there were some 65 isolated white dwarfs classified as magnetic and a roughly equal number found in the close interacting binaries known as the magnetic cataclysmic variables. Hitherto, the Sloan Digital Sky Survey in the northern hemisphere and the SN Ia Supernova Progenitor Survey collaboration in the southern hemisphere have largely expanded the number of white dwarfs to more than 20,000. Kleinman et al. (2013) have found hundreds of stars with Zeeman splittings indicating magnetic fields above 3×10^6 G. Specifically, they have classified 628 DAHs, 10 DBHs and 91 with mixed atmosphere high-field magnetic white dwarfs. In the local population, within 20 pc of the Sun, there are 122 white dwarfs (Holberg et al., 2008), 14 of them magnetic and 8 with magnetic fields in excess of 10^7 G. White dwarfs with moderate magnetic fields have been detected in close, detached binary systems in which the primary is a white dwarf and the companion is a low-mass main-sequence star. In fact, $\sim 10\%$ of all isolated white dwarfs have high magnetic fields and a larger fraction, $\sim 25\%$, are found in cataclysmic variables. Another observed important feature of high-field magnetic white dwarfs is that they are usually massive. The average mass of white dwarfs is $\sim 0.6\ M_\odot$, whereas high-field magnetic white dwarfs have an average mass of $\sim 0.8\ M_\odot$ (Kawka et al., 2007). Moreover, magnetic white dwarfs are not rapid rotators. Their periods lay in the range of days to weeks, though in some cases periods of hours are found.

The origin of high-field magnetic white dwarfs is not yet well known. Angel et al. (1981) suggested that magnetic white dwarfs descend from Ap/Bp stars following the fossil field hypothesis. However, detailed population synthesis studies show that the observed number of Ap/Bp stars is insufficient to explain the number of magnetic white dwarfs, and the contribution of an unseen population of weakly magnetized A/B stars needs to be invoked (Wickramasinghe & Ferrario, 2000). Therefore, other

possible evolutionary channel should also exist. The high mass, high rotation rate and age discrepancy with the close DA white dwarf companion of REJ 0317−855 suggested that this white dwarf could be the result of a double degenerate merger (Ferrario et al., 1997). But this is not the only magnetic white dwarf for which the merger hypothesis has been proposed (Wickramasinghe & Ferrario, 2000). Actually the merger hypothesis is favored because magnetism could influence the initial-final mass relationship, and may also favor the formation of more massive double degenerates in close binary evolution, hence leading more easily to Type Ia supernovae. Additionally, there are other possible evolutionary scenarios that could explain the existence of high-field magnetic white dwarfs. Most of them claim that magnetism is naturally related to binary evolution, and are mainly aimed at explaining the higher incidende of magnetic white dwarfs in cataclysmic variables. For instance, Tout et al. (2008) and Nordhaus et al. (2011) discussed the possibility that turbulence during a common envelope episode could generate strong magnetic fields. Nevertheless, Potter & Tout (2010) showed that the magnetic fields generated in this way are not durable in the resulting white dwarf. In chapter 5 we propose that in the corona of the merger product of two white dwarfs, magnetic fields of the required strength that do not decay for long timescales can be produced through an $\alpha\omega$ dynamo. These conditions are produced because of the simultaneous exitence of convection and differential rotation in those layers. This preliminary finding has been later corroborated by Schwab et al. (2012), who presented multi-dimensional hydrodynamic simulations of the evolution of white dwarf merger remnants using an α prescription for the viscosity. Finally, we also argue that long rotation periods found in most magnetic white dwarfs are the result of magnetic braking caused by magneto-dipole radiation.

1.3.2 Anomalous X-ray pulsars

The first hard X-ray burst was detected in 1976 (Grindlay et al., 1976). Two years later, when the first fully imaging X-ray telescope, the High Energy Astronomy Observatory Einstein of NASA, was launched, an enterirely new sky was discovered. Most of the brightest stars to human eye resulted dim in X-rays, whilst an entire new set of X-ray stars were shining with unexpected power. Bright X-ray stars come in many types. Most of them are tight binaries containing a compact star and an ordinary star. The high gravity of the compact star attracts gas from its companion, which interacts with the searing, turbulent disk surrounding the compact star. Additionally, the surface of the compact star is heated by the material raining down from the disk. These accretion processes release copious amounts of gravitational energy as X-rays, often with luminosities larger than $10^4\,L_\odot$ or more. There are also isolated neutron stars that emit strong X-rays. These X-rays are powered by the rotational energy that is released by magnetized young and very fast-spinning neutron stars that spin out a flow of plasma and radio waves. However, by 1994

five strange high X-ray pulsars had been detected that seemed not to be powered by neither rotation, since the rotational energy loss seemed insuficient, nor gravitational accretion, because no companion star was detected. Two years earlier, Duncan & Thompson (1992) had introduced the concept of magnetar, which consists of a neutron star whose extremely strong magnetic field decay provides an electromagnetic power, and this seemed a possible explanation for these enigmatic stars. Now these stars are classified as Anomalous X-ray pulsars (AXPs).

AXPs have spin periods clustered in a narrow range, between 2 and 12 s, and are all spinning down with spin-period derivatives in the 10^{-15} to 10^{-10} s s^{-1} range. These properties are shared with Soft Gamma-ray Repeaters (SGRs). SGRs are sporadic, intense flares of soft (low-energy) γ-rays and hard X-rays. SGRs were the first stars to be classified as possible magnetars. Given their similarity to SGRs, AXPs are believed to be also magnetars. The reason for this is that the energy balance of the pulsar spin down by magneto-dipole radiation can account for the super-Eddington soft γ-ray bursts and because, if this is the case, to reproduce the values of the period P and its derivative $\dot{P}$ large magnetic dipole strengths are needed. Nowadays, about a dozen of pulsars have been classified as AXPs or SGRs, but the relation between these sources and other classes of astrophysical objects different than magnetars is still a matter of a heated debate.

In order to explain the observed X-ray luminosity of the super-Eddington bursts of SGRs, the magnetar model needs a magnetic field larger than the critical field for vacuum polarization $B_{\rm c} = m_{\rm e}^2 c^3/(eh) = 4.4 \times 10^{13}$ G (Duncan & Thompson, 1992; Thompson & Duncan, 1995). However, the quantitative explanation of the persistent soft X-ray luminosity by magnetic field decay, the optical and infra-red properties during persistent states, the X-ray and the accompanying infra-red enhancements, and the period clustering of AXP and SGRs all seem to meet difficulties within the original frame of the magnetar model (Trümper et al., 2010). In the literature there exist other models based on neutron stars of ordinary fields $B \sim 10^{12}$ G. These models involve the accretion of fallback material from fossil disks (van Paradijs et al., 1995; Marsden et al., 2001; Trümper et al., 2010), or the generation of drift waves in the magnetosphere (Malov, 2010). Alternatively, it has been recently suggested (Malheiro et al., 2012) that SGR 0418+5729 could be a massive white dwarf, instead of a neutron star, as the pioneering works of Morini et al. (1988) and Paczynski (1990) on the AXP of 1E 2259+586 proposed. Moreover, it has been hypothesized that this explanation can be extended to all SGRs and AXPs. Actually three of the remaining AXPs — 1E 2259+586, 1E 0418+5729, and Swift J1822.3−1606 — are supposed to be low magnetic field magnetars and have been recently studied by Boshkayev et al. (2013a) as prototypes of massive, fast-rotating, highly magnetized white dwarfs. In Chapter 6 we study the case of 4U 0142+61. Initial optical images of this pulsar were given to dismiss the possibility of a large surrounding disk and to support the magnetar model (Kern & Martin, 2002), but the discovery of mid-infrared emission from a cool disk around this isolated young X-ray pulsar (Wang

et al., 2006) encouraged the search for an alternative progenitor model. In this work we show that the properties of this AXP can be well explained by a model in which the star is the remnant of a merger of two ordinary white dwarfs. Within this model, the central compact object is a massive magnetized white dwarf surrounded by the heavy accretion disk. This is done in chapter 6.

Chapter 2

Smoothed Particle Hydrodynamics simulations of the core degenerate scenario for Type Ia supernovae

The core degenerate scenario for type Ia supernovae involves the merger of the hot core of an asymptotic giant branch (AGB) star and a white dwarf, and might contribute a non-negligible fraction of all thermonuclear supernovae. Despite its potential interest, very few studies, and based on only crude simplifications, have been devoted to investigate this possible scenario, compared with the large efforts invested to study some other scenarios. Here we perform the first three-dimensional simulations of the merger phase, and find that this process can lead to the formation of a massive white dwarf, as required by this scenario. We consider two situations, according to the mass of the circumbinary disk formed around the system during the final stages of the common envelope phase. If the disk is massive enough, the stars merge on a highly eccentric orbit. Otherwise, the merger occurs after the circumbinary disk has been ejected and gravitational wave radiation has brought the stars close to the Roche lobe radius on a nearly circular orbit.

2.1 Introduction

It has long been suggested that a white dwarf in a binary system — with either another white dwarf — through the so-called double-degenerate scenario (Webbink, 1984; Iben & Tutukov, 1984) — or a main-sequence or red giant companion — through the single degenerate scenario (Whelan & Iben, 1973; Nomoto, 1982; Han & Podsiadlowski, 2004) — could give rise to a SN Ia event. More recent scenarios — see the reviews of Wang & Han (2012) and Maoz et al. (2014) — include the

double-detonation scenario, where helium-rich material is accreted by the carbon-oxygen white dwarf (e.g., Shen & Bildsten 2009; Ruiter et al. 2011), the double white dwarf collision scenario (Raskin et al., 2009; Rosswog et al., 2009; Thompson, 2011; Kushnir et al., 2013), and the core degenerate scenario (Sparks & Stecher, 1974; Livio & Riess, 2003; Kashi & Soker, 2011; Ilkov & Soker, 2012, 2013; Soker et al., 2013) to be studied here. Within the core degenerate scenario the white dwarf merges with the hot core of a massive asymptotic giant branch (AGB) star (Livio & Riess, 2003; Kashi & Soker, 2011; Ilkov & Soker, 2012, 2013). In a recent paper Tsebrenko & Soker (2015a) argue that approximately 20%, and likely many more, of all Type Ia supernovae come from the core degenerate scenario. Moreover, a recent population synthesis study suggests that the merger of the core of an AGB star and a white dwarf can indeed be very common (Briggs et al., 2015). A table summarizing these scenarios with their main advantages and drawbacks can be found in Tsebrenko & Soker (2015a).

While several simulations of the double-degenerate progenitor channel have been already performed over the last two decades (Benz et al., 1990; Segretain et al., 1997; Guerrero et al., 2004; Yoon et al., 2007; Lorén-Aguilar et al., 2009; Pakmor et al., 2010; Dan et al., 2011; Raskin et al., 2013), no full three-dimensional simulation of the core degenerate scenario has been done so far. The present work aims at filling this gap, and it is organized as follows. In section 2.2 we discuss the initial conditions considered to simulate the core degenerate scenario. It follows section 2.3, where we briefly explain the numerical techniques used. In section 4.3 we describe in depth the results of our simulations. Finally, in section 2.5 we summarize our main findings, and we draw our conclusions.

2.2 Initial conditions

2.2.1 The final phase of the common envelope

Kashi & Soker (2011) estimated that during the last stages of the common envelope phase, between $\sim 1\%$ and 10% of the ejected envelope remains bound to the binary system composed of the cold white dwarf and the hot core of the AGB star. They furthermore suggested that, due to angular momentum conservation and further interaction of the remaining common envelope with the binary system, the fallback material forms a circumbinary disk around the binary. This newly formed disk would later interact with the binary system, thus reducing the orbital separation of the pair much more than what it was reduced during the dynamical phase where the common envelope is ejected, while the eccentricity of the binary system would increase. Using the results of Artymowicz et al. (1991), Kashi & Soker (2011) obtained the rate at which the semimajor axis decreases and the rate at which the eccentricity of the orbit increases. In addition, they also took into account the rate at which the circumbinary disk losses mass during the interaction.

Kashi & Soker (2011) found that the final values of the orbital parameters critically depend on the amount of matter ejected from the system through disk winds. Specifically, they found that for disks with masses $M_{\rm disk} \gtrsim 0.12(M_{\rm core} + M_{\rm WD})$ — where $M_{\rm disk}$, $M_{\rm core}$, and $M_{\rm WD}$ are, respectively, the masses of the disk, the core of the AGB star and the white dwarf — the circumbinary disk-binary interaction leads to a merger if the speed of the disk wind is the escape velocity. For the particular case studied by Kashi & Soker (2011), where $M_{\rm WD} = 0.6\,M_\odot$, $M_{\rm core} = 0.77\,M_\odot$ and $M_{\rm env} = 4.23\,M_\odot$, the mass of the disk amounts to $\sim 4\%$ of the mass of the envelope. They also found that for less massive circumbinary disks the separation is not reduced enough to result in a merger during the interaction. In these cases, gravitational wave radiation will reduce the orbital separation and the eccentricity further. Consequently, the final merger would occur when the orbit of the binary system is almost circular. Hence, in these cases it turns out that the orbital separation, a, and the distance at closest approach are very similar, and the Roche lobe overflow occurs when $a \simeq R_{\rm L}$, being $R_{\rm L}$ the Roche lobe radius of the white dwarf. Moreover, since the timescale for gravitational wave emission is long the core of the AGB star would be cold (Kashi & Soker, 2011).

2.2.2 Orbital parameters

We compute the evolution of the orbital parameters of the binary system before the merger occurs following closely the procedure of Kashi & Soker (2011). In particular, we consider the same binary as Kashi & Soker (2011) and we adopt two different disk masses. Writing

$$M_{\rm disk} = q_{\rm disk}(M_{\rm core} + M_{\rm WD}), \tag{2.1}$$

we adopt as reference cases $q_{\rm disk} = 0.12$ — a disk with a mass just over the critical one — and $q_{\rm disk} = 0.10$ — a low-mass one. When $q_{\rm disk} = 0.12$ the merger occurs just before the disk is totally ejected from the system. Hence, the merger would occur when the orbit of the binary system is still highly eccentric, and moreover the core of the AGB star would still be hot.

The time evolution of the orbital parameters for $q_{\rm disk} = 0.12$ is displayed in the left panel of Fig. 2.1, where we show the evolution of both the orbital separation (solid line, left scale), and of the eccentricity (dashed line, right scale). The large, hollow circles correspond to the time instant at which the periastron distance equals the Roche-lobe radius ($r_{\rm min} = R_{\rm L}$) of the white dwarf, while the solid, blue circles show the point at which the mass transfer episode begins — see below for details about the mass transfer episode. Note that both times are almost coincidential. For this disk, the merger occurs at $t \sim 270$ days after the common envelope is ejected.

The equivalent diagram for the case in which $q_{\rm disk} = 0.10$ is shown in the right panel of Fig. 2.1. In this case, the disk has been totally ejected at early times (the time at which this occurs is represented using black, solid circles in this figure). For a relatively long time interval the orbital separation and the eccentricity of the pair

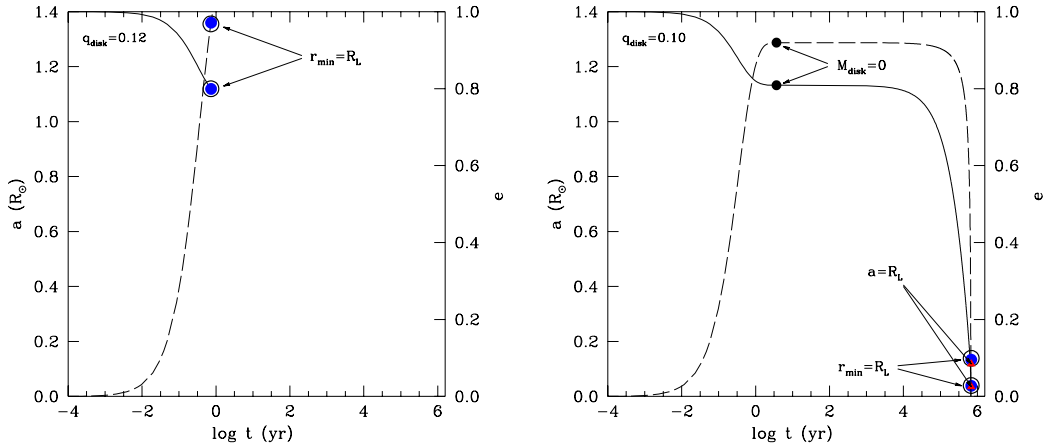

Figure 2.1: Evolution of the orbital parameters of the binary system formed by an AGB star and a white dwarf during its interaction with the circumbinary disk, once a large fraction of the envelope of the AGB star has been ejected. The left panel shows the case in which a massive circumbinary disk with $q_{\rm disk} = 0.12$ is adopted, whereas the right panel the case in which $q_{\rm disk} = 0.10$ is considered — see text for details. The solid lines and left scale show the evolution of the semimajor axis (a), and the dashed lines and the right scale display that of the eccentricity (e). The hollow, large circles indicate when the Roche-lobe radius of the white dwarf equals the periastron of the orbit, and the blue solid symbols show the point at which mass transfer begins. Finally, for the right panel, the point where the semimajor axis equals the Roche-lobe radius is indicated by a triangle. Also in this panel the time at which the circumbinary disk has been totally ejected is indicated by the solid black circles.

remain almost constant, but as time goes on the emission of gravitational waves progressively decreases the orbital distance and the eccentricity of the pair, being faster for times just before the merger begins. Eventually, at approximately 6×10^5 years after the common envelope of the system is ejected both stars merge. As in the previous case we also show in this panel the points where $r_{\rm min} = R_{\rm L}$ and the points at which the merger starts. Additionally, in this panel we also show the times for which the orbital separation equals the Roche lobe radius of the white dwarf (black triangles). Note that in this case the eccentricity is small ($e \sim 0.1$) and that we expect that, given the very long timescale of gravitational wave emission, the post-AGB star will have a cold core. In cases where merger takes place within several$\times 10^5$ yr, the SN Ia ejecta might catch up with the ejected common envelope, that once was a planetary nebula. This "SN Ia Inside a PN" is termed a SNIP (Tsebrenko & Soker, 2015a,b).

2.2.3 The temperature of the AGB core

For the sake of completeness for each of the cases described earlier we perform two simulations. For the first of these simulations we adopt a low temperature for the isothermal core of the AGB star ($T = 10^6$ K), while for the second we adopt a hot core ($T = 10^8$ K). The white dwarf is always cold, and for it we adopt $T = 10^6$ K. The adopted temperature has an effect on the initial configuration of the core of the AGB star (of mass $M_{\rm core} = 0.77\,M_\odot$). The radii are $R_{\rm core} \simeq 1.02 \times 10^{-2}\,R_\odot$ and $R_{\rm core} \simeq 9.33 \times 10^{-3}\,R_\odot$, and the central densities are $\rho_{\rm c}^{\rm core} \simeq 6.83 \times 10^6$ g cm^{-3} and $\rho_{\rm c}^{\rm core} \simeq 7.07 \times 10^6$ g cm^{-3}, for the hot and cold cores, respectively. Note that these differences are significant, of the order of a few percents, and thus may have non-negligible effects on the dynamical evolution of the merger, and on the question of whether there is an ignition upon merger (Yoon et al., 2007).

2.3 Numerical setup

The characteristics of the SPH code used for these simulations are explained in appendix A. As mentioned before, the mass transfer episode begins once the distance between the two binary members at passage through the periastron is smaller than the Roche-lobe radius. To obtain reliable configurations when both stars are at closest approach we proceeded as follows. We first relaxed independent configurations for each of the stars of the binary system and we placed them at the apastron in a counterclockwise orbit. We then evolved the system in the corotating frame to obtain equilibrium configurations at this distance. Once this relaxation process was finished, we started the simulations in the inertial reference frame. In a first set of preliminary simulations we explored at which distance the mass transfer episode ensues. This is done employing a reduced number of particles ($\sim 2 \times 10^4$ for each star). Once we know which are the orbital separation and the eccentricity of the orbit for which we obtain a Roche-lobe overflow we computed a second set of simulations with enhanced resolution. Since for highly eccentric orbits both stars are initially separated by very large distance, to save computing time in this second set of simulations we first followed the evolution of the system employing the reduced resolution and, once the stars had completed one quarter of the orbit, these low-resolution simulations were stopped and both stars were remapped using a large number of SPH particles (a factor of 10 larger). We then resumed the simulations with this enhanced resolution. This was done because for systems with large eccentricities the computing load required to follow an uninteresting phase of the orbital evolution of the pair is exceedingly large.

2.4 Results

As discussed earlier, in this chapter we simulate four different configurations for the binary system. In all cases the mass of the core of the AGB star and the white dwarf are, respectively, $0.77\,M_\odot$ and $0.60\,M_\odot$. The first configuration corresponds to a binary system that has a disk with a mass ratio equal to the critical one of $q_{\rm disk} = 0.12$ (see equation 2.1), while for the second one we have chosen a disk with a mass ratio of $q_{\rm disk} = 0.1$, which is below the critical value. For each one of these cases we have studied the coalescence when the temperature of the core of the AGB star is high ($T = 10^8$ K) and low ($T = 10^6$ K).

For the highly eccentric orbit that results when $q_{\rm disk} = 0.12$ is adopted, the first mass transfer from the white dwarf to the core occurs when the distance at closest approach is $r_{\rm min} = 0.9\,R_{\rm L}$, where $R_{\rm L}$ is the Roche lobe radius of the white dwarf. In this expression $R_{\rm L}$ is computed using the classical analytical expression of Eggleton (1983), which does not take into account tidal deformations, and is only valid for circular orbits. Hence, this difference is natural. At this time the semimajor axis is $a = 1.12\,R_\odot$ and the eccentricity is $e = 0.97$. For the less massive disk with $q_{\rm disk} = 0.10$ the merger begins when the eccentricity of the orbit is small $e = 0.095$. Accordingly, the periastron distance is very similar to the radius of the Roche lobe of the white dwarf. Specifically, we obtain that the merger occurs when $r_{\rm min} = 0.98\,R_{\rm L}$ and $a = 0.038\,R_\odot$. The orbital parameters at these times are represented by the blue dots in Fig 2.1. Particularly relevant for the discussion of our results are the values of the respective initial periods. For the case of the system with $q_{\rm disk} = 0.12$ the initial orbital period is $T_0 \simeq 10,126$ s, while for the case in which $q_{\rm disk} = 0.10$ is used the initial period is significantly shorter, $T_0 \simeq 65$ s.

2.4.1 Evolution of the merger

Fig. 2.2 shows the time evolution of the binary system during the merger for the case in which the temperature of the AGB core is 10^8 K and for $q_{\rm disk} = 0.12$. Shown are the positions of the SPH particles and their color-coded temperatures. The left column shows the evolution in the orbital plane and the right column in the meridional plane, respectively. In Fig. 2.3 we present the results in the same setting for the case in which $q_{\rm disk} = 0.10$ is adopted. The white dwarf is the object located initially at the right, and later is destroyed, while the core of the AGB star is initially located at the left.

The top panels of Figs. 2.2 and 2.3 are at the initial stages of the merger, at times $t/T_0 \simeq 0.501$ for $q_{\rm disk} = 0.12$, and $t/T_0 \simeq 0.640$ for $q_{\rm disk} = 0.10$, respectively. We remind that the orbital periods are $T_0 = 10,126$ s for $q_{\rm disk} = 0.12$, and $T_0 = 65$ s for $q_{\rm disk} = 0.10$, respectively. As can be seen the white dwarf is significantly deformed, due to tidal interactions, being the deformation larger for the case of an eccentric orbit (Fig. 2.2). For the second row of panels we have chosen slightly larger times,

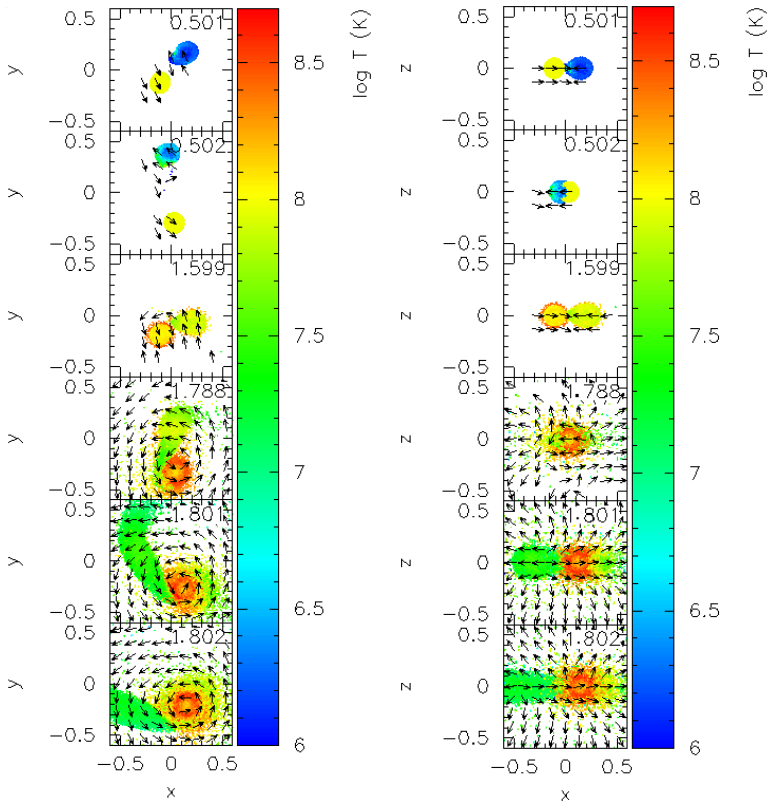

Figure 2.2: Evolution of the binary system for selected stages of the merger, as described in the main text, in the equatorial (left) and meridional (right) planes, for the case in which a hot core of the AGB star is adopted and for $q_{\rm disk} = 0.12$. The color scale shows the logarithm of the temperature, whereas the x, y and z axes are in units of 0.1 $R_\odot$. The arrows show the direction of the velocity field, but not its magnitude, in the corresponding plane. Each panel is labelled with the corresponding time in units of the initial binary period, $T_0 = 10,126$ s. The white dwarf is the object located initially at the right, and later is destroyed. These figures have been done using the visualization tool SPLASH (Price, 2007).

$t/T_0 \simeq 0.502$ and $t/T_0 \simeq 0.74$, respectively, and show that tidal deformations close to periastron are much larger for eccentric mergers. This leads to a faster heating of the external layers of the secondary star. The third rows show the systems when the system has evolved trough several passages trhough the periastron. For $q_{\rm disk} = 0.12$ (Fig. 2.2) we have chosen the sixth mass transfer episode and for $q_{\rm disk} = 0.10$ (Fig. 2.3) the twenty-third one. These correspond to times $t/T_0 \simeq 1.599$ and $t/T_0 \simeq 22.2$, respectively. As can be seen, at these evolutionary stages in both cases the secondary (the white dwarf) has increased its temperature, and more mass has been accumulated on the primary core.

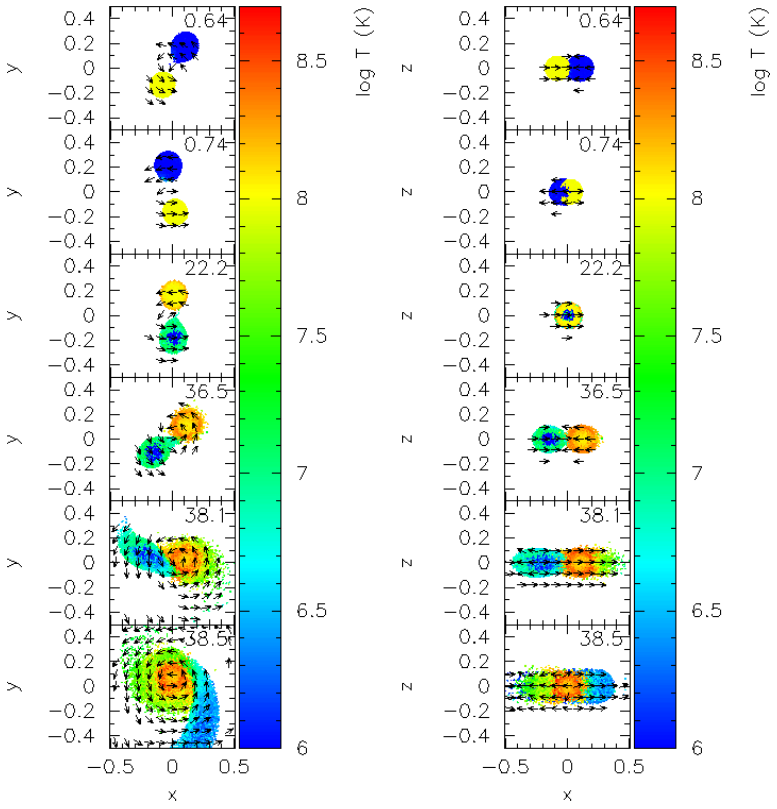

Figure 2.3: Same as Fig. 2.2, but for $q_{\rm disk} = 0.10$. In this case the initial orbital period is $T_0 = 65$ s.

The fourth rows of Figs. 2.2 and 2.3, at times $t/T_0 \simeq 1.788$ and $t/T_0 \simeq 36.5$ respectively, display the situation during the last orbit, just before the secondary white dwarfs are completely disrupted by the cores of the AGB stars. At this point, for $q_{\rm disk} = 0.12$ the white dwarf still keeps $\approx 80\%$ of its initial mass, while for $q = 0.10$ this percentage is somewhat larger, $\approx 90\%$. The fifth rows correspond to a time close to that at which the peak temperature is reached, which happens during the final infall of the secondary star onto the core of the AGB star. Specifically, we have chosen $t/T_0 \simeq 1.801$ and $t/T_0 \simeq 38.1$, respectively. As it will be discussed in more detail later, for $q_{\rm disk} = 0.12$ these temperatures are higher than for $q_{\rm disk} = 0.10$. The reason for this is twofold. First, the material of the white dwarf is hotter for $q_{\rm disk} = 0.12$, a consequence of the previous evolution. The second reason is that in this case the matter of the disrupted white dwarf falls onto the primary star with a much larger radial velocity than for $q_{\rm disk} = 0.10$. Consequently, matter is compressed more violently in this case. Finally, the last rows show the systems at late times. We have chosen times $t/T_0 \simeq 1.802$ and $t/T_0 \simeq 38.5$, respectively. As can be seen,

the material of the completely disrupted secondary white dwarf is spiralling around the primary star.

A general feature of our simulations is that the secondary star, the white dwarf, is totally disrupted after several periastron passages. In each of these periastron passages mass is transferred in a relatively gentle way. Accordingly, in all cases the density and temperature conditions for a detonation to develop are not met. As can be seen in Figs. 2.2 and 2.3, in none of the cases the peak temperature reaches 10^9 K, and hence, although nuclear reactions are important, a powerful explosion does not occur.

We emphasize that when $q_{\rm disk} = 0.12$ is adopted — that is, for those mergers for which the eccentricity is high — the successive mass transfer episodes only happen when both stars are very close. Actually, it turns out that when both stars are at closest approach the secondary white dwarf is substantially tidally deformed, and the mass transfer episode occurs just after the passage through the periastron. However, soon after this, tidal deformations become smaller, so the mass transfer episode stops, and both components of the binary system recover their initial spherical symmetry for the rest of the orbit. On the contrary, when $q_{\rm disk} = 0.10$ is employed — corresponding to mergers driven by the emission of gravitational waves — the orbits are almost circular, and although the mass transfer episodes take place also at periastron, when the secondary is significantly distorted by tidal forces, the secondary star remains tidally deformed for the entire orbit, and thus the merger process proceeds in a smoother way.

In all four cases the successive mass transfer episodes modify the mass ratio of both components of the binary system, and this in turn changes the respective orbits. Fig. 2.4 displays the trajectories of the center of mass of both components of the binary system. The left panels of this figure depict the trajectories of the centers of mass of the white dwarf components. The blue lines correspond to the cases in which the core of the AGB star is cold (labelled as CC), while the red ones show the cases in which we adopt a high temperature for the core of the AGB star (labelled as HC). In the right panels the trajectories of the center of mass of the AGB cores are displayed, using the same color coding. The top panels of this figure display the case in which $q_{\rm disk} = 0.12$. As can be seen, in this case the orbits are eccentric, while in the bottom panels, corresponding to $q_{\rm disk} = 0.10$, the orbits are initially nearly circular. As mentioned earlier, for both cases it turns out that during the first periastron passage the white dwarf transfers mass to the heavier AGB core and its radius increases. This radius increase starts a series of successive mass transfer episodes that ultimately lead to a merger.

We stress that the number of mass transfer episodes depends not only on the physical characteristics of the binary system but also on the number of SPH particles employed in the simulations, that is, on the spatial resolution. Although our resolution is enough for studying the overall properties of the dynamical interaction and the gross properties of the merged remnants, it is clear as well that our simu-

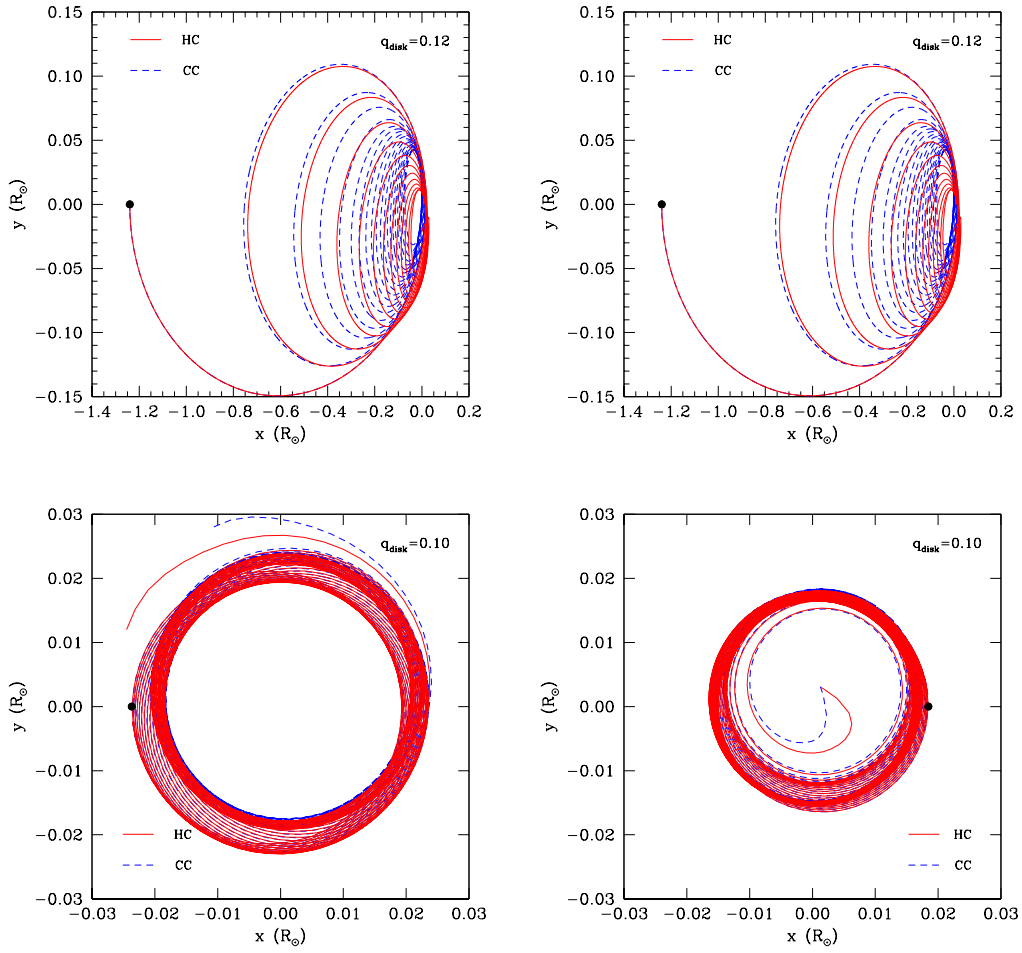

Figure 2.4: Trajectories of the centers of mass of the white dwarfs (left panel) and cores of the AGB stars (right panel) for the case in which $q_{\rm disk} = 0.12$ is adopted (top panels) and that in which $q_{\rm disk} = 0.10$ is employed (bottom panels). The blue dashed lines correspond to the case in which a cold AGB core is adopted, and the red solid lines to that in which a hot core is assumed. The solid black circles indicate the initial positions of both stars for each of the panels.

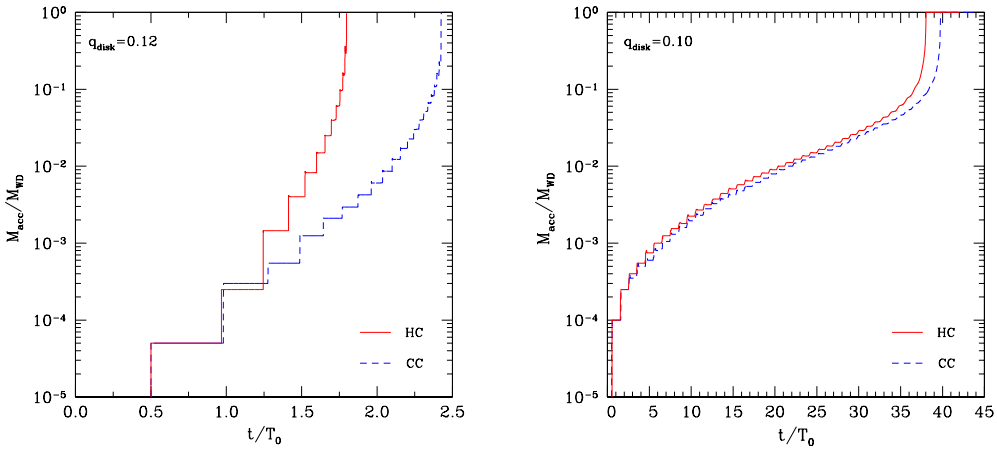

Figure 2.5: Mass accreted by the AGB core as a function of time, expressed in terms of the initial orbital period. The left panel corresponds to $q_{\rm disk} = 0.12$, while the right displays the case in which $q_{\rm disk} = 0.10$. Each step in these panels corresponds to a periastron passage. The total time span is $\simeq 25,315$ s for the left panel, and $\simeq 2,925$ s for the right one.

lations provide only a lower limit to the number of mass transfer episodes. For this reason we do not quote the number of mass transfer episodes. Note as well that for the case in which $q_{\rm disk} = 0.10$ it is quite apparent that the last orbits are not circular, but instead during the final stages of the merger the orbit becomes quite eccentric. This final infall phase also takes place in the case of eccentric mergers. However, due to the difference of scales of the axis, it cannot be well seen in the top panels of Fig. 2.4. Finally, it is also worth noting that the trajectories of the centers of mass for the case in which cold AGB cores are considered are only slightly different of those obtained in the case of hot AGB cores. Hence, the effects of the temperature of the AGB core on the overall dynamical evolution are very minor.

Figure 2.5 shows the mass accreted by the core of the AGB star ($M_{\rm acc}$), in units of the initial white dwarf mass ($M_{\rm WD}$), as a function of time in units of the initial period of the binary system, T_0. As in Fig. 2.4, the blue lines correspond to the case in which a cold merger is considered, while the red ones show the evolution for the hot merger. Again, the left panel displays the evolution for $q_{\rm disk} = 0.12$, whereas the right panel shows the same for $q_{\rm disk} = 0.10$. The mass accreted by the core of the AGB star corresponds to the total mass of those SPH particles originally belonging to the disrupted secondary for which the gravitational attraction of the core of the AGB star is larger than that of the white dwarf.

Inspecting Fig. 2.5 we find that the mass accreted during the first mass transfer episode does not depend on the temperature of the AGB core, but depends critically on the adopted eccentricity. It is also interesting to point out that for the case in

which a hot AGB core is adopted, mass is transferred faster than during the first mass transfer episode in successive passages through the periastron, for both $q_{\rm disk} = 0.12$ and 0.10. This is more noticeable for $q_{\rm disk} = 0.12$ — i.e., a merger in which the eccentricity is high. Also, it is important to realize that for the cases in which a hot AGB core is adopted the amount of mass transferred in each one of the episodes is always larger than for the cases in which a cold AGB core is considered. All this stems from the fact that for a hot AGB core the degeneracy of the material of the outer layers is smaller than that of a cold core, and thus the core of the AGB star can accommodate more accreted mass.

In all the four cases studied here the mass transferred during the second mass transfer episode is larger than that transferred during the first periastron passage. This is a consequence of the substantial change of the orbital period after the first periastron passage, especially for $q_{\rm disk} = 0.12$. Specifically, for this case the period decreases by $\approx 50\%$ as seen in Fig. 2.6. This is less evident for the case in which $q_{\rm disk} = 0.10$ is adopted because in this case the period decreases by a modest $\approx 0.2\%$. All this translates into a smoother evolution, also for the successive mass transfer episodes, for the $q_{\rm disk} = 0.10$ cases. Thus, it turns out that the duration of the mergers is shorter for the cases in which a hot AGB is adopted, being this feature more pronnounced for the case in which eccentric orbits are considered. Finally, note as well that in each accretion episode there is a small decline in the accreted mass. These declines correspond to matter, that although being initially accreted by the core of the AGB star, is bounced back to the debris region shortly after.

To better illustrate the dynamical evolution of the mergers, Fig. 2.6 displays the evolution of the periods (left panels) and eccentricities (right panels) of the binary systems studied here. As before, the top panels depict the evolution of the orbital parameters for $q_{\rm disk} = 0.12$, whilst the bottom ones show that for the case in which $q_{\rm disk} = 0.10$ is adopted. As can be clearly seen, in all four simulations after each mass transfer episode the periods of the binary systems decrease and the orbits become circularized. These general trends become more accentuated as the evolution proceeds. Although for $q_{\rm disk} = 0.10$ initially the period decreases smoothly in an almost linearly way with a shallow slope, after $t \sim 35T_0$ the white dwarf almost plunges on top of the core of the AGB star. This is in contrast with what occurs for $q_{\rm disk} = 0.12$, for which the decrease in the orbital periods occurs faster during the initial stages of the dynamical evolution, in marked steps, and the white dwarf merges with the core of the AGB star in very few orbital periods, $\sim 2T_0$. The right panels of this figure show that the eccentricity also decreases for increasing times. For $q_{\rm disk} = 0.12$ this occurs in marked steps, as it occurs with the orbital periods, a consequence of the succesive passages through the periastron, while for $q_{\rm disk} = 0.10$ the eccentricity also decreases but oscillates arroung a mean (decreasing) value. This is caused by tidal forces.

Figure 2.7 shows the average temperature of the core for the different cases considered here. To compute this temperature we averaged the temperature of those

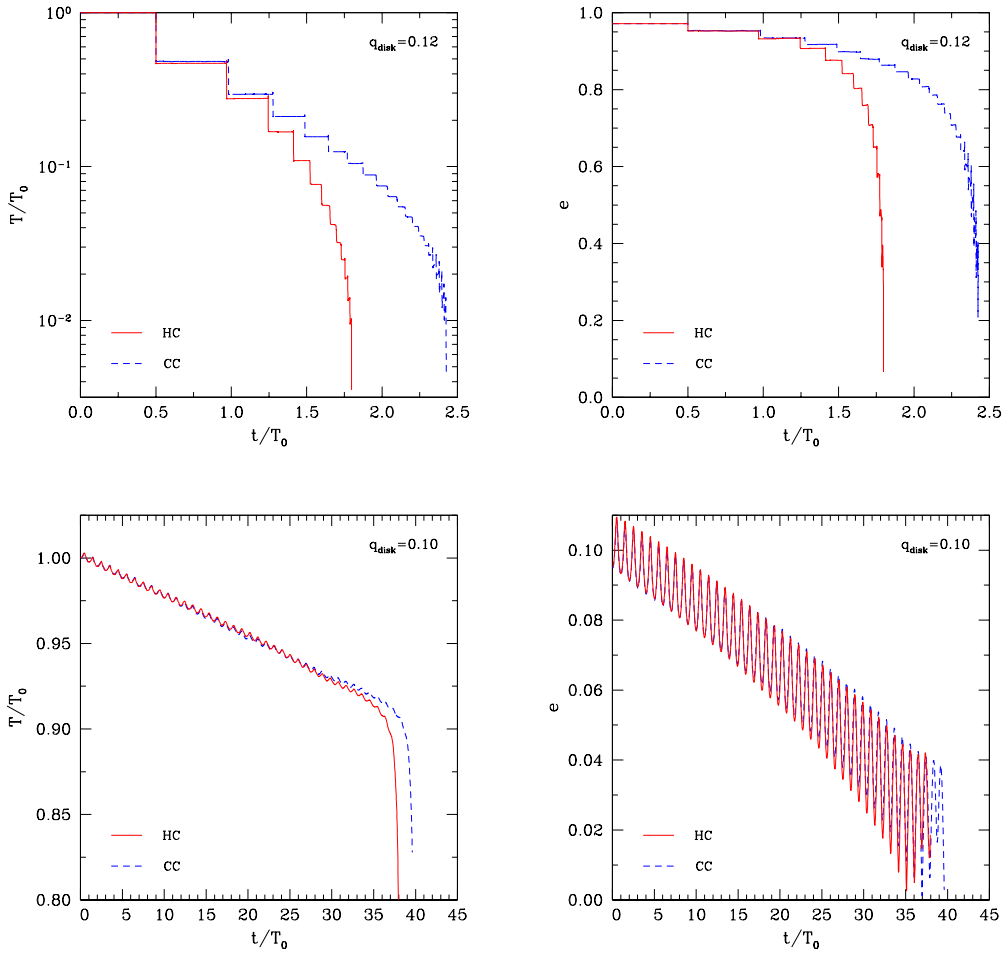

Figure 2.6: The evolution of the periods (left panels) and of the eccentricities (right panels) during the merger process. The top panels represent the case in which $q_{\rm disk} = 0.12$ is considered, and the bottom ones those in which $q_{\rm disk} = 0.10$ is adopted.

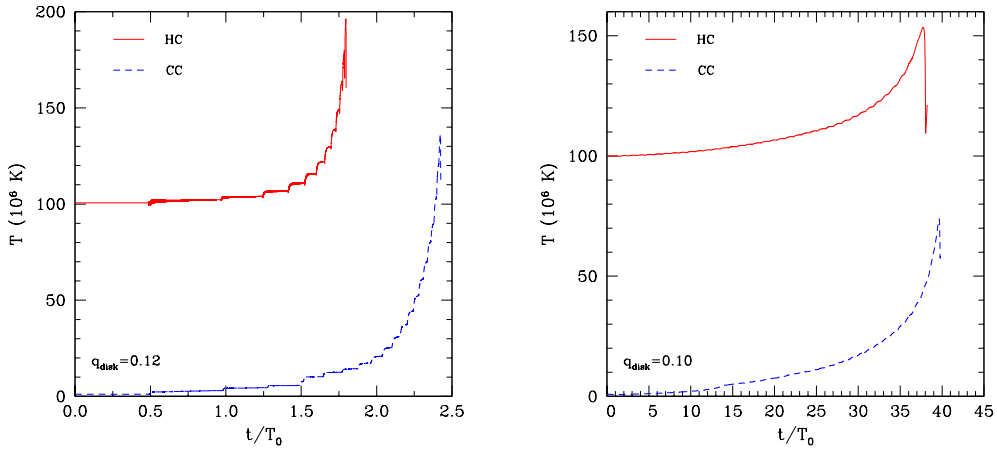

Figure 2.7: Average temperature of the core of the AGB star during the merger, for the case in which $q_{\rm disk} = 0.12$ is considered (left panel), and for that in which $q_{\rm disk} = 0.10$ (right panel).

particles which were originally used to model the core, and thus we did not take into account the accreted material from the disrupted white dwarf. This is an important detail, since the maximum temperatures during the evolution of the simulated cases of coalescence are not reached in the core of the merged remnant but in the hot corona formed during the interaction — see below. As before, the left panel and right panels represent, respectively, the cases for which $q_{\rm disk} = 0.12$ and $q_{\rm disk} = 0.10$ are adopted. As can be seen, since for eccentric orbits the amount of mass transferred during each dynamical episode is larger, the temperatures are increased more noticeably. Actually, the temperature is not raised homogenously in the entire core. Specifically, the temperature of the outer layers of the core is notably increased after every mass transfer episode, while the temperature of the very deep interior of the core remains nearly constant. As it should be expected, the final temperatures of the hot cores are much larger than their cold counterparts. Nonetheless, in both cases temperatures in excess of 10^8 K are reached, but these temperatures are far from those necessary to power a detonation.

Table 2.1 shows some relevant characteristics of the stellar interactions studied in this work. In columns three to five of this table we list, respectively, the maximum temperature reached during the dynamical interaction, $T_{\rm peak}$, the total nuclear energy released, $E_{\rm nuc}$, and the total duration of the merger, Δt. The maximum temperature always is reached at the base of the accreted layer. The nuclear energy is essentially released by carbon burning reactions and the α chains. Most of the nuclear reactions occur on top of the almost rigid surface of the core of the AGB star, as

Table 2.1: Some relevant characteristics of the merged remnants. By columns: (1) value of $q_{\rm disk}$ from equation 2.1, (2) type of run, hot (HC) or cold (CC) core of the AGB star, (3) maximum temperature attained during the dynamical interaction, (4) nuclear energy released, (5) duration of the merger, (6) Mass of the merged remnant at the end of the simulations, (7) mass of Keplerian disk at the end of the simulations, (8) mass of the extended shroud at the end of the simulations, (9) mass of fall-back material, (10) ejected mass, (11) maximum temperature of the merged remnant, (12) maximaum angular speed of the hot corona at the end of the simulations.

$q_{\rm disk}$	Run	$T_{\rm peak}$ (K)	$E_{\rm nuc}$ (erg)	Δt (s)	$M_{\rm mr}$ ($M_\odot$)	$M_{\rm disk}$ ($M_\odot$)	$M_{\rm shroud}$ ($M_\odot$)	$M_{\rm fb}$ ($M_\odot$)	$M_{\rm ej}$ ($M_\odot$)	$T_{\rm max}$ (K)	$\omega_{\rm max}$ (s^{-1})
0.12	HC	9.23×10^{8}	1.13×10^{39}	18343	0.88	0.36	9.08×10^{-2}	2.19×10^{-2}	1.74×10^{-2}	3.56×10^{8}	0.23
	CC	8.55×10^{8}	3.54×10^{37}	24784	0.88	0.35	9.84×10^{-2}	2.02×10^{-2}	1.80×10^{-2}	3.53×10^{8}	0.25
0.10	HC	8.74×10^{8}	1.12×10^{39}	2599	0.93	0.39	4.86×10^{-2}	2.43×10^{-3}	7.37×10^{-4}	2.97×10^{8}	0.30
	CC	8.18×10^{8}	4.77×10^{37}	2710	0.91	0.41	4.59×10^{-2}	2.56×10^{-3}	8.70×10^{-4}	3.10×10^{8}	0.32

the material of the disrupted white dwarf is accreted, compressed and heated. Again, we emphasize that the duration of the merger not only depends on the physical characteristics of the coalescing stars, but also on the adopted resolution. The reason for this is that, as it occurs with double-degenerate mergers, the durations of the mass transfer episodes depend on the extent to which the outer layers of the donor star can be resolved. In most practical situations the particle masses are such that the resolvable mass transfer rate is already a substantial fraction of the total system mass — see Dan et al. (2011) for a detailed discussion of this issue. Hence, these durations should be regarded as indicative, and can be only used to compare the different cases studied here, which were computed with the same spatial resolution and input physics.

Figs. 2.2, 2.3 and 2.5 reveal that the peak temperature is reached at $t = 1.8T_0$ and $t = 2.4T_0$ for the hot and cold cores of the AGB star when $q_{\rm disk} = 0.12$ and at $t = 38.1T_0$ and $t = 40.3T_0$ for the case in which $q_{\rm disk} = 0.10$. When this occurs the fraction of the secondary white dwarf that has been accreted onto the core of the AGB star is $\gtrsim 20\%$ for $q_{\rm disk} = 0.12$, whereas for $q_{\rm disk} = 0.10$ it is $\lesssim 10\%$. All this has a direct effect on the thermonuclear reaction rates, and consequently on the total nuclear energy released during the interactions. In particular, while for the case of hot cores the total nuclear energy released is $\approx 10^{39}$ erg, for the cold ones it is much smaller, $\approx 10^{37}$ erg. The nuclear energy released is similar for the eccentric orbits and the non-eccentric ones for a fixed temperature of the AGB core, despite the difference in the peak temperatures achieved during the interaction.

Finally, we note that eccentric orbits ($q_{\rm disk} = 0.12$) result in mergers with durations of a few hours, much longer than those of mergers with $q_{\rm disk} = 0.10$, for which the durations are smaller than ~ 1 hour. However, we remind that for the case of

eccentric orbits the coalescence occurs in just a couple of initial orbital periods, while for circular ones the merger lasts for several initial orbital periods.

2.4.2 The remnants of the interaction

The general appearance of the remnants resulting from the interaction is similar for all the cases studied in this chapter, and moreover is similar to that found in previous simulations of the double-degenerate scenario for similar masses — see, for instance, Lorén-Aguilar et al. (2009), and references therein. The remnants of the interactions when simulations were stopped consist of a central degenerate object which contains all the mass of the core of the AGB star and some accreted mass. This central object spins as a rigid body and its angular momentum arises from the conversion of the orbital angular momentum of the binary system to rotational one. This core is surrounded by a corona, which contains a sizable fraction, $\sim 18\%$ for eccentric mergers and $\approx 27\%$ for circular ones, of the mass of the disrupted secondary (the white dwarf). The material of the corona is hot — a consequence of the material of the disrupted secondary being compressed on top of the almost rigid surface of the core of the AGB star — and rotates differentially — a consequence of the several mass transfer episodes occurring in the dynamical interaction. Finally, the rest of the material of the secondary ($\sim 82\%$ and $\approx 73\%$, respectively, for eccentric and circular mergers) that is not accreted on the central object goes to form a thick accretion disk, with a Keplerian velocity profile, and an extended shroud made of particles that have orbits with large inclinations with respect to the orbital plane, while some SPH particles have highly eccentric orbits and will ultimately fall back onto the primary, and very little mass is ejected from the system.

Table 2.1 lists also some of the characteristics of the merged remnant. In column 6 we list the mass of the central merged object ($M_{\rm mr}$) — that is, the sum of the mass of the undisturbed AGB core and of the hot corona — while in column 7 the mass of the Keplerian disk ($M_{\rm disk}$) is listed. The precise location of the inner edge of the hot corona is defined as the (spherical) mass coordinate for which the angular velocity is no longer constant, while the outer boundary of this region is defined as the point where the profile of angular velocities of the remnants is the Keplerian. In this table we also show the mass of the extended shroud ($M_{\rm shroud}$), that of the fallback material ($M_{\rm fb}$), as well as the mass ejected from the system ($M_{\rm ej}$) — columns 8, 9 and 10, respectively. As mentioned, the shroud is composed of material coming from the disrupted secondary that has approximately a spherical distribution. The fallback material is composed of particles belonging to the debris region that have very eccentric orbits as a result of the extreme conditions found during the very first stages of the dynamical interaction, but are still gravitationally bound to the merged remnant. Thus, it is expected that this material will ultimately fall back onto the central remnant at some later time (Rosswog, 2007). To compute the amount of mass in the debris region that will eventually fall back on the central object we

followed the same procedure described in Aznar-Siguán et al. (2014). Note that there is as well some material that is not gravitationally bound to the remnant and might escape, but the merger episodes are essentially conservative. We would like to remark that we do not look for a possible formation of jets and disk winds which, in the double-degenerate scenario, influece the appearance of an explosion if it occurs shortly after the merger (Levanon et al., 2015). Finally, for the sake of completeness we also list the maximum temperature ($T_{\rm max}$) and the maximum angular velocities ($\omega_{\rm max}$) of the hot corona, columns 11 and 12, respectively.

The central compact object

As can be seen in Table 2.1, the angular velocities of the remnants do not depend appreciably on the adopted temperature of the core of the AGB star, although there are significant differences depending on the value of $q_{\rm disk}$. The reason for this is that in the coalescence studied here the rigid rotation of the core of the AGB star arises from the conservation of angular momentum. That is, the orbital angular momentum of the pair is basically invested in spinning up the primary and the previously described corona, and to form the Keplerian disk. Nevertheless, the angular velocity of the remnants of the mergers in which a cold AGB core is involved are somewhat larger in both cases. This is due to the slightly smaller radii of these configurations (see Fig. 2.8 below), which in turn is a consequence of their larger degeneracies.

We now compare the angular velocities obtained for different values of $q_{\rm disk}$. As shown in Table 2.1, when $q_{\rm disk} = 0.10$ is adopted the angular velocities are larger. In particular, we find that for this case the inner regions of the merged remnant rotate uniformly at a speed $\omega \simeq 0.22$ s^{-1}, whereas in the corona a maximum angular velocity of $\omega_{\rm max} \simeq 0.31$ s^{-1} is reached. For the case in which $q_{\rm disk} = 0.12$ these angular velocities are, respectively, $\omega \simeq 0.18$ s^{-1}, and $\omega_{\rm max} \simeq 0.24$ s^{-1}, somewhat smaller than those of the case in which $q_{\rm disk} = 0.10$ is employed. The orbital angular momentum of the binary systems studied here is $J = 5.96 \times 10^{50}$ erg s for $q_{\rm disk} = 0.12$, and $J = 4.63 \times 10^{50}$ erg s when $q_{\rm disk} = 0.10$. Since the merger is almost conservative (very few particles acquire energies large enough to escape from the merged remnant) this angular momentum is distributed essentially in spinning up the core of the AGB star, in the differential rotation of the hot corona and in the Keplerian disk.

For a hot merger their respective angular momenta are $J_{\rm core} \simeq 1.4 \times 10^{49}$ erg s, $J_{\rm corona} \simeq 4.4 \times 10^{49}$ erg s and $J_{\rm disk} \simeq 2.8 \times 10^{50}$ erg s for $q_{\rm disk} = 0.12$, and $J_{\rm core} \simeq 1.5 \times 10^{49}$ erg s, $J_{\rm corona} \simeq 6.7 \times 10^{49}$ erg s and $J_{\rm disk} \simeq 3.2 \times 10^{50}$ erg s for $q_{\rm disk} = 0.10$, respectively. For the case of a cold merger these values do not differ much. Hence, the orbital angular momentum of the eccentric merger is larger than that of the circular one, and moreover the angular momenta are distributed in a different way in both cases. Specifically, the angular momentum of the corona for $q_{\rm disk} = 0.12$ is noticeably smaller than that of the merger in which $q_{\rm disk} = 0.10$ is adopted, but the mass of

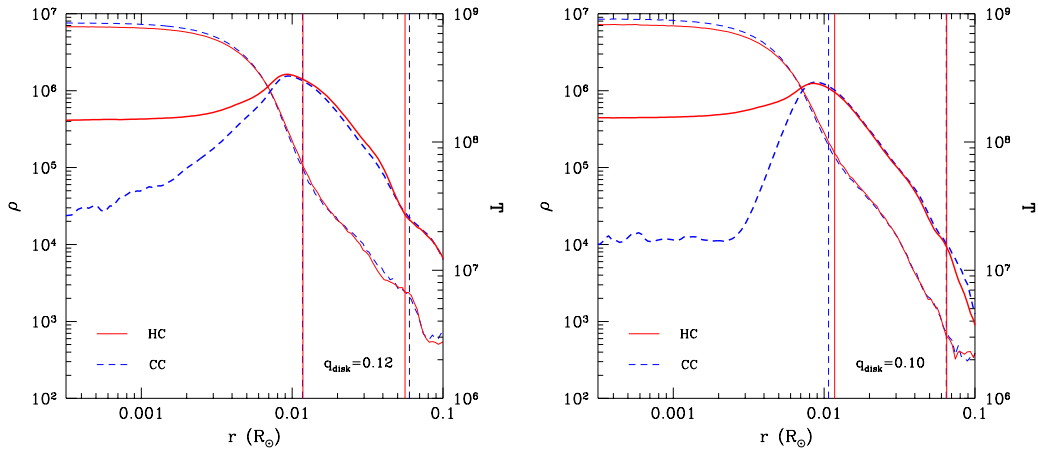

Figure 2.8: Density (thin lines) and temperature (thick lines) profiles of the central part of the remnants, at times $t/T_0 = 1.8115$ and 2.4476 for the hot (solid red lines) and cold (dashed blue lines) AGB cores of the simulation in which $q_{\rm disk} = 0.12$, and $t/T_0 = 40.2378$ and 41.9690 for the case in which $q_{\rm disk} = 0.10$ is adopted, respectively. These times correspond to our last computed models. As before, in the left panel we represent the profiles for $q_{\rm disk} = 0.12$, while the right one corresponds to $q_{\rm disk} = 0.10$. The abscissa is the spherical radius in solar units. Note that for large distances the spherical radius is not a valid representation of the merged configuration, as the assumption of spherical symmetry is only fulfilled to a good approximation in the innermost regions of the merged remnant. The leftmost solid vertical lines show the outer boundaries of the respective coronae. The rightmost vertical lines mark the outer edges of the respective Keplerian disks.

their respective coronae do not differ that much. Also the angular momentum of the newly formed disk of the eccentric merger is significantly smaller than that of the circular one. Consequently, more angular momentum is stored in these (outer) regions for the case in which $q_{\rm disk} = 0.10$ is adopted when compared to the case in which $q_{\rm disk} = 0.12$. Finally, for the the simulations in which $q_{\rm disk} = 0.12$ is employed the ejected mass is considerably larger than that of the case in which $q_{\rm disk} = 0.10$ is used. This mass carries some angular momentum. All this explains why the merged remnant spins at a slower rate for $q_{\rm disk} = 0.12$. All this is a consequence of the dynamical evolution during the merger. We remind that for $q_{\rm disk} = 0.12$ the evolution proceeds in abrupt steps, while for $q_{\rm disk} = 0.10$ mass is accreted in a more gentle way.

Figure 2.8 shows the density (dashed lines) and temperature (solid lines) profiles, for the case in which $q_{\rm disk} = 0.12$ (left panel) and the for the case in which $q_{\rm disk} = 0.10$ (right panel). The maximum temperature ($T_{\rm max}$) in all the remnants is very similar, close to $3{\times}10^8$ K, being slightly higher for the remnants of the eccentric mergers. This

can be easily understood in terms of the evolution during the last merger episode. In particular, it has been already mentioned that for eccentric mergers the mass transfer episodes are more dramatic than for the case of nearly circular orbits. Hence, the matter of the disrupted secondary white dwarf acquires larger accelerations and, consequently, is compressed more violently on the surface of the primary star. Thus, the temperatures of the external layers of the merged configuration are larger, and a hotter corona is obtained.

The stronger interaction of the accreted matter with the primary during the successive mass transfer episodes leaves also clear imprints on the structure of the internal regions of the merged remnant. Specifically, for the case of eccentric mergers in which a cold core of the AGB star is considered, the temperature of the outermost regions of the initially isothermal core begins to increase at earlier times during the coalescence, when compared to those in which a circular orbit is involved. Consequently, by the end of the merger process the core of this remnant is no longer isothermal. On the contrary, the core in the case of a circular orbit remains nearly isothermal — see Fig. 2.8. Finally, owing to the substantial degeneracy of the material of the core of the AGB star, the density profiles obtained in all the four simulations presented here are very similar.

The debris region

It has been already discussed that the temperature of the AGB core barely plays a role in the dynamical evolution of the merger process, and in determining the structure of the merged remnant. Instead, the most important parameter is the eccentricity of the initial orbits of both components of the binary system. This is true as well for the debris region formed around the merged remnants. The masses of the fallback and of the ejected material are, respectively, $M_{\rm fb} \simeq 2.1 \times 10^{-2}\, M_{\odot}$ and $M_{\rm ej} \simeq 1.8 \times 10^{-2}\, M_{\odot}$ for eccentric mergers, while for circular orbits the masses are much smaller, $M_{\rm fb} \simeq 2.5 \times 10^{-3}\, M_{\odot}$ and $M_{\rm ej} \simeq 8.1 \times 10^{-4}\, M_{\odot}$. The larger fallback and ejected masses in the case of eccentric mergers are a consequence of the longer durations (or, equivalently, larger orbital separations) of the mass transfer episodes — see Figs. 2.5 and 2.6.

As well, the masses of the respective shrouds are relatively different, $M_{\rm shroud} \simeq 9.2 \times 10^{-2}\, M_{\odot}$ for $q_{\rm disk} = 0.12$ and $M_{\rm shroud} \simeq 4.7 \times 10^{-2}\, M_{\odot}$ for $q_{\rm disk} = 0.10$. This is again a consequence of the very different number of mass transfer episodes occurring in both simulations. Actually, for $q_{\rm disk} = 0.12$ we find that some mass of the disrupted white dwarf flows around the region located in the opposite direction of the line connecting both stars of the system, and acquires high velocities when colliding with the primary star, forming this extended shroud. The size of this extended region does not depend much on the temperature adopted for the core of the AGB star. This can be seen in Fig. 2.9, where the density (left panel) and temperature (right panel) contours of the merged remnant in the meridional plane

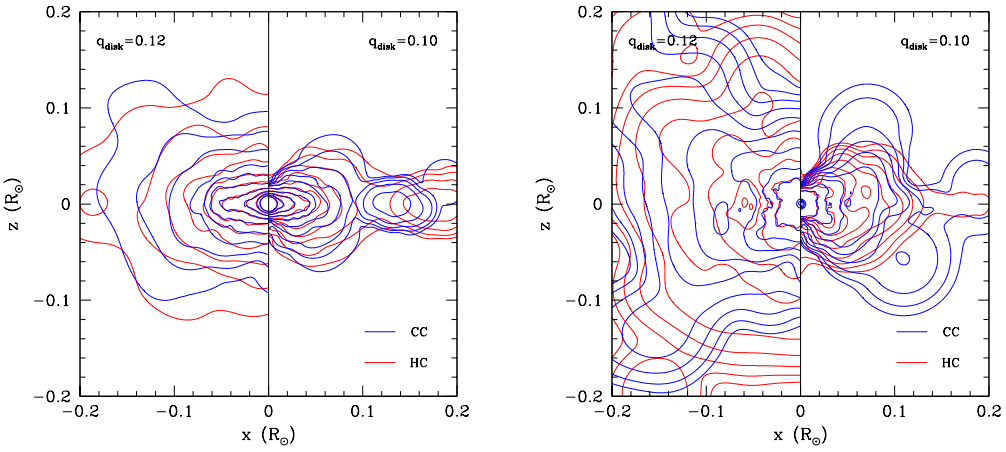

Figure 2.9: Left panel: density contour lines of the remnants across the meridional plane. Right panel: temperature contour lines across the same section. These density and temperature maps correspond to our last computed models, and the evolutionary times are the same of Fig. 2.8. The remnants represented with negative x coordinates correspond to the case in which $q_{\rm disk} = 0.12$, while for positive values of x the case in which $q_{\rm disk} = 0.10$ is represented. For both cases the outermost contour of the density profile corresponds to a density of 1 g cm^{-3} and the successive contours increase logarithmically inwards in constant steps of $\log \rho = 0.62$. The contour of maximum density corresponds to $\sim 3.8 \times 10^5$ g cm^{-3}. For the temperature the outermost contour corresponds to $\sim 3 \times 10^5$ K and the successive contours increase inwards logarithmically in steps of $\log T = 0.33$. The maximum temperature contour corresponds to $\sim 1.4 \times 10^8$ K. This temperature is reached in the hot corona, while the innermost regions of the merged remnant in the case of a core with small temperature merger are colder — see Fig. 2.7.

are displayed. In this figure the sub-panel with negative values of the x-coordinate corresponds to the case $q_{\rm disk} = 0.12$, whereas that with positive values shows the same contours for the case in which $q_{\rm disk} = 0.10$ is adopted.

As can be seen in Fig. 2.9, both the density and the temperature decrease as the distance to the central compact object increases, independently if we consider the remnants of eccentric or circular mergers. However the decline rate of both the density and the temperature for eccentric mergers is smaller than for circular orbits, resulting in a more extended debris region, which moreover is hotter. Additionally, the density and temperature profiles also have a different behavior near the polar regions of the central remnant. For mergers arising from circular orbits there is a region near the z-axis (the vertical axis in this figure) where the density and the temperature contour lines converge towards the poles, in contrast with what happens for the case of eccentric mergers, for which this region is absent, and the contour

lines are perpendicular to this axis. These differences between both profiles are a consequence of how the material of the disrupted secondary white dwarf is distributed on top of the primary (the core of the AGB star) during the dynamical interaction.

The final infall of the disrupted secondary onto the unaltered primary for $q_{\rm disk} = 0.10$ seen in Figs. 2.3 and 2.4, does not allow matter to be redistributed on the primary, but instead concentrates it in the orbital plane. Besides, the circular density contours that appear at the right of the remnant correspond to a spiral arm of matter infalling to the primary. Since SPH codes are not able to follow properly angular momentum transport, we stopped the simulations at a reasonable time after the complete disruption of the secondary. In particular, for $q_{\rm disk} = 0.12$ we stopped the simulations at $t/T_0 = 1.8115$ and $t/T_0 = 2.4476$ for the hot and cold merger, respectively. For $q_{\rm disk} = 0.10$ these times are, respectively, $t/T_0 = 40.2378$ and $t/T_0 = 41.9690$. In this case, the secondary had no time to be totally distributed over the primary and the spiral arm formed during the infalling phase is still present. The more flat structure for $q_{\rm disk} = 0.10$, which is more similar to that usually found in the simulations of the double-degenerate scenario, might lead to jets and disk winds that might alter the observations if explosion occurs shortly after merger (Levanon et al., 2015). Finally, the outer edges of the Keplerian disks formed during the merger process are located where the density distribution in the equatorial plane has no longer axial symmetry. In all cases this occurs at $\sim 0.06\,R_\odot$.

2.5 Summary and conclusions

In this chapter we have simulated the coalescence of a white dwarf with the core of a massive AGB star, in the context of the so-called core-degenerate scenario for Type Ia supernovae. Specifically, we have computed the merger of an otherwise typical white dwarf of mass $0.6\,M_\odot$ with the core of an AGB star of mass $0.77\,M_\odot$, which is a typical case (Kashi & Soker, 2011). This has been done for two temperatures of the AGB core, $T = 10^6$ K and 10^8 K, and for two assumptions about the mass of the disk formed during the common envelope phase. In particular, we have studied a first case in which the mass of the disk is $M_{\rm disk} = 0.12(M_{\rm core} + M_{\rm WD})$, which corresponds to the critical mass ratio for which a merger is guaranteed as a consequence of the interaction with the disk formed during the common envelope phase. The second case studied here corresponds to a binary system surviving the common envelope phase with a mass ratio 0.10, which is below the critical one, and for which the merger is driven by the emission of gravitational waves. The first of these cases results in a pair with a highly eccentric orbit, whereas for the second one the orbits of the members of the binary system are circular, and similar to those expected for the double-degenerate scenario for SNe Ia.

Our SPH simulations show that temperature of the core of the AGB star has little influence on the overall dynamical evolution of the merging process and on

the characteristics of the merger remnant, but the initial eccentricity of the binary system has a large impact on both the dynamical evolution of the merger and on the properties of the merged object. In particular, in both cases the white dwarf is totally disrupted in a series of mass transfer episodes, which occur at closest approach. However, the duration of the coalescence is notably different in both cases. Specifically, we found that for the case of an eccentric merger the disruption of the secondary white dwarf occurs in very few orbital periods, whereas for the case of the mergers in which circular orbits are adopted this process lasts for many orbital periods. Nevertheless, the initial orbital periods in both cases are very different — 10,126 s and 65 s, respectively — so the total time required to disrupt the secondary white dwarf turns out to be larger for the case of eccentric orbits.

In all the four cases studied in this chapter the coalescence process is almost conservative, and little mass is ejected from the system, $\sim 2 \times 10^{-2}\, M_{\odot}$ at most. Nevertheless, eccentric mergers eject ~ 25 times more mass than that ejected by binary systems with circular orbits. The peak temperatures achieved during the merging process are rather high, of the order of 8×10^{8} K, but not enough to power a prompt detonation upon merger. As for the final temperature of the merger remnant it is interesting to realize that for the cases studied here the temperature profile peaks off-center. The possibility that carbon is ignited in the remnant, thus producing a rapidly spinning oxygen-neon white dwarf, has been discussed by Saio & Nomoto (2004), Yoon & Langer (2004), and Yoon & Langer (2005). Our results do not support this possibility, since the peak temperature obtained at the end of our simulations is too low, and moreover the temperature peaks in a region where the densities are relatively small.

The structure of the merged remnant consists of a central compact object containing all the mass of the core of the AGB star and some mass from the disrupted secondary star, which is surrounded by a hot, differentially rotating corona. This corona is made of about 18% of the mass of the disrupted white dwarf, for the case of eccentric mergers, and somewhat larger ($\sim 27\%$) for circular ones. Finally, surrounding this central compact object there is a heavy, rapidly-rotating Keplerian disk, and an extended shroud of material which are formed by the rest of the mass of the disrupted white dwarf that has approximately ellipsoidal shape. This configuration is essentially the same found for double-degenerate mergers. However, the structure of the debris region is different depending on the initial eccentricity of the merger. For mergers with initially circular orbits the matter of the disrupted white dwarf concentrates in regions near the orbital plane, and little mass is found in the polar regions, whereas for eccentric mergers part of the mass of the disrupted white dwarf is distributed along the central compact object, and the merged configuration adopts an ellipsoidal shape. In the debris region there is also some fraction of SPH particles with highly eccentric orbits. This material will ultimately interact with matter in the Keplerian disk and will fall back onto the central compact remnant. The mass of this fallback material is typically or the order of $2 \times 10^{-2}\, M_{\odot}$ for the

case of the binary systems with eccentric orbit, and ten times smaller for those with circular ones. In all cases, this central object rotates as a rigid body, with typical angular velocities ~ 0.18 s^{-1} for the case of eccentric mergers and ~ 0.22 s^{-1} for circular ones. These rotation velocities arise from the conversion of orbital angular momentum to rotational one, as it happens for double-degenerate mergers.

We would like to emphasize that if the disk, fallback material, and the material of the extended shroud are finally accreted, as it is commonly thought, the mass of the remnant would be $\approx 1.35\,M_{\odot}$. If this is the case, after cooling and losing angular momentum this remnant might eventually explode. Of course, assessing such possibility requires modelling the viscous phase of the merger, which transports disk mass inwards and angular momentum outwards. This phase has typical timescales ranging from 10^3 s to 10^4 s, during which the disk might launch jets and winds (Levanon et al., 2015), and it cannot be followed using SPH techniques. If, nonetheless, all this mass is accreted and the remnant explodes the delay would be very long, up to millions of years (e.g. Piersanti et al. 2014), or even longer (Ilkov & Soker, 2012).

In summary, this first set of simulations of the core-degenerate scenario for SNe Ia demonstrates the need of exploring in more detail the effects of the eccentricity (and possibly of the temperature) on the overall dynamical evolution of the merger and on the properties of the merged configurations obtained in this scenario, especially when more massive stars are involved. The simulations presented here are a first important step in this direction. Future works will undoubtely allow us to characterize and place tight constraints on the most salient features of this scenario, and may possibly help in quantifying the fraction of these mergers that contributes to the total SNe Ia rate, thus filling a gap and complementing what we already learned from the existing simulations of the double degenerate scenario.

Chapter 3

Detonations in white dwarf dynamical interactions

In old, dense stellar systems collisions of white dwarfs are a rather frequent phenomenon. Here we present the results of a comprehensive set of Smoothed Particle Hydrodynamics simulations of close encounters of white dwarfs aimed to explore the outcome of the interaction and the nature of the final remnants for different initial conditions. Depending on the initial conditions and the white dwarf masses, three different outcomes are possible. Specifically, the outcome of the interaction can be either a direct or a lateral collision or the interaction can result in the formation of an eccentric binary system. In those cases in which a collision occurs, the infalling material is compressed and heated such that the physical conditions for a detonation may be reached during the most violent phases of the merger. While we find that detonations occur in a significant number of our simulations, in some of them the temperature increase in the shocked region rapidly lifts degeneracy, leading to the quenching of the burning. We thus characterize under which circumstances a detonation is likely to occur as a result of the impact of the disrupted star on the surface of the more massive white dwarf. Finally, we also study which interactions result in bound systems, and in which ones the more massive white dwarf is also disrupted as a consequence of the dynamical interaction. The sizable number of simulations performed in this work allows to find how the outcome of the interaction depends on the distance at closest approach, and on the masses of the colliding white dwarfs, and which is the chemical pattern of the nuclearly processed material. Finally, we also discuss the influence of the masses and core chemical compositions of the interacting white dwarfs and the different kinds of impact in the properties of the remnants.

3.1 Introduction

Globular clusters and galactic nuclei are dense and old stellar systems. In these environments the most probable collisions are those in which at least one of the colliding stars has a large cross-section — a red giant or an AGB star — and those in which at least one of the stars is common (Shara & Regev, 1986). Since white dwarfs are the most usual end-point of stellar evolution, and because both globular clusters and galactic nuclei are rather old, these stellar systems contain many degenerate stars. Therefore, collisions in which one of the colliding stars is a white dwarf should be rather common (Lorén-Aguilar et al., 2010). Additionally, it has been recently shown that close encounters of two white dwarfs could be more frequent than previously thought (Katz & Dong, 2012).

Recently, the study of the collisions of two white dwarfs has received considerable interest, since it has been shown that, under certain circumstances, the result of such interactions could be a Type Ia supernova outburst (Raskin et al., 2009, 2010; Rosswog et al., 2009). However, there are very few simulations of this phenomenon. In fact, the small number of simulations of white dwarf collisions is noticeable when compared to the number of simulations in which two white dwarfs belonging to a binary system merge. Specifically, the first simulations of colliding white dwarfs (Benz et al., 1989) were done using an SPH method, but employing a rather small number of particles in the calculations, a consequence of the severe computational limitations. Other recent calculations (Rosswog et al., 2009) also employed SPH techniques, but due to the large parameter space to be studied, the calculations were mostly restricted to head-on collisions, this time using a large number of particles. The reason for this choice was that these simulations were primarily aimed at obtaining a thermonuclear explosion, and it was foreseen that very high temperatures were most likely to be obtained in these kind of interactions. This was also the aim of subsequent calculations (Raskin et al., 2009, 2010), which indepently confirmed the results of Rosswog et al. (2009) using an independent SPH code. Finally, the collisions of two white dwarfs have also been studied recently using the Eulerian adaptive grid code FLASH (Hawley et al., 2012). However, these authors only computed zero impact parameter collisions for two equal-mass white dwarfs, a $0.64\,M_{\odot} + 0.64\,M_{\odot}$ pair and a $0.81\,M_{\odot} + 0.81\,M_{\odot}$ system. As in most of the previous studies of this kind, the primary goal of this work was again to study an independent channel for producing Type Ia supernovae.

In summary, most authors have studied the collision of two white dwarfs with fixed masses, and have varied the total energy and angular momentum of the colliding white dwarfs, while little attention has been paid up to now to study the effects of the masses of the interacting stars. This was also the approach adopted by Lorén-Aguilar et al. (2010), where the masses of the intervening white dwarfs ($0.6\,M_{\odot}$ and $0.8\,M_{\odot}$) were kept fixed, while their initial relative velocity and distance were varied. They found that the outcome of the interaction could be either a direct collision, a

lateral one, or could be the formation of an eccentric binary system. Nevertheless, the outcome of the dynamical interaction depends on the masses (and on the core chemical composition) of the interacting white dwarfs. Thus, a comprehensive study of the interactions of two white dwarfs covering a broad range of masses and initial conditions is still lacking. The present work aims precisely at filling this gap.

The SPH code used for these simulations is explained in appendix A. In section 3.2 of this chapter we present the initial conditions considered in our simulations. It follows section 3.3, where the outcomes of the collisions and close encounters are presented and analyzed. In section 3.4 we present the most significant features of the extensive set of simulations performed so far. Finally, in section 3.5 we summarize our main findings, we discuss their significance and we draw our conclusions.

3.2 Initial conditions

We have relaxed five different white dwarf models with masses $M_1 = 0.4\,M_\odot, 0.6\,M_\odot$, $0.8\,M_\odot, 1.0\,M_\odot$ and $1.2\,M_\odot$. The chemical composition of all white dwarfs is a mixture of 40% carbon and 60% oxygen (by mass), except for the lightest one — which is made of pure helium — and the heaviest one — which is made of a mixture of 80% of oxygen and 20% of neon, also by mass. The intervening stars were relaxed separately to obtain accurate equilibrium initial configurations, using $\sim 2 \times 10^5$ particles for each star. This resolution is high enough to provide accurate results and low enough to run a large number of simulations in a reasonable period of time. The initial temperature of our isothermal white dwarf configurations is $\sim 10^7$ K. As in Lorén-Aguilar et al. (2010), the white dwarfs were assumed to rotate counterclockwise as rigid bodies (Charpinet et al., 2009) with rotational velocities $\omega \simeq 7 \times 10^{-5}$ rad/s — a typical rotation velocity of field white dwarfs (Berger et al., 2005). This rotation rate is nevertheless irrelevant to the dynamics of the close encounters studied in this chapter. In fact, the spin rates of post-capture white dwarfs could be larger, as the capture is dominated by tidal dissipation, which would lead to spin-up of at least the lower mass white dwarf, and of both stars if the masses are comparable (Press & Teukolsky, 1977).

We fixed the initial distance between the stars along the x-axis, $\Delta x = 0.2\,R_\odot$, and allowed the initial distance along the y-axis to vary between $\Delta y = 0.3\,R_\odot$ and $0.4\,R_\odot$. Under these conditions the tidal deformations of both white dwarfs are negligible at the beginning of the simulation and the approximation of spherical symmetry is valid. The initial velocity of each star was set to $\mathbf{v}_{\rm ini} = (\pm v_{\rm ini}, 0, 0)$, with $v_{\rm ini}$ ranging from 75 to 300 km/s, which are typical values for which the interaction ends up in a collision. With this setting the initial coordinates of the two intervening white dwarfs are $(\Delta x/2, -\Delta y/2, 0)$ and $(-\Delta x/2, \Delta y/2, 0)$ and the relative velocity is $2v_{\rm ini}$. Note that these initial conditions lead in all cases to negative energies, which result in initial elliptical trajectories, although some of them have high eccentricities — see

below. That is, the interactions studied here correspond to a post-capture scenario. For a detailed study of the gravitational capture mechanisms see, for example, Press & Teukolsky (1977) and Lee & Ostriker (1986). Additionally, we note that in order for a pair of stars to become bound after a close encounter, some kind of dissipation mechanism must be involved, like a third body tidal interaction (Shara & Hurley, 2002), or the excitation of stellar pulsations by means of tidal interaction (Fabian et al., 1975).

3.3 Outcomes of the interactions

3.3.1 Time evolution

In most simulations the time evolution of the interactions computed here is the same found in the previous paper (Lorén-Aguilar et al., 2010). In particular, after tidal interaction, the intervening white dwarfs either form an eccentric binary or collide. In particular, if the intervening stars get sufficiently close at periastron and mass transfer begins, a stellar merger occurs. In this case, two different behaviors can be clearly distinguished. If more than one mass-transfer episode occurs before the stellar merger, we name it a lateral collision (LC). Else, if just one mass transfer happens, then we call the interaction a direct collision (DC). Otherwise, if the binary system survives without transferring mass, an eccentric orbit will be the outcome (O) of the interaction.

Also, for most of the cases studied here in which a collision occurs, the resulting remnants left behind by the dynamical interaction are very similar to those found in our previous work (Lorén-Aguilar et al., 2010). However, there are a few cases in which the interaction is so strong that the material of the lightest white dwarf is ejected from the system. Finally, there are as well some interactions in which both stars are totally disrupted. This occurs as a consequence of the very high temperatures attained in the contact region during the most violent phase of the dynamical interaction. Specifically, in all the simulations in which one or both stars are disrupted and the material is ejected from the system the temperatures and densities reached during the interaction are high enough to drive a detonation. If the material of the disrupted less massive star is a mixture of carbon and oxygen this occurs when the temperature is larger than $\sim 2.5 \times 10^9$ K and the density is above 2.0×10^6 g cm^{-3} (Seitenzahl et al., 2009; Pakmor et al., 2011). When the less massive white dwarf is made of helium we consider that a detonation is likely to develop when the nuclear timescale is shorter than the dynamical one. Nevertheless, we emphasize that these are only necessary conditions, since whether a detonation develops or not depends as well on other factors, like the temperature and density gradients.

We find that in most of the simulations in which the material of the disrupted low-mass white dwarf reaches high temperatures and large densities the regions in which a

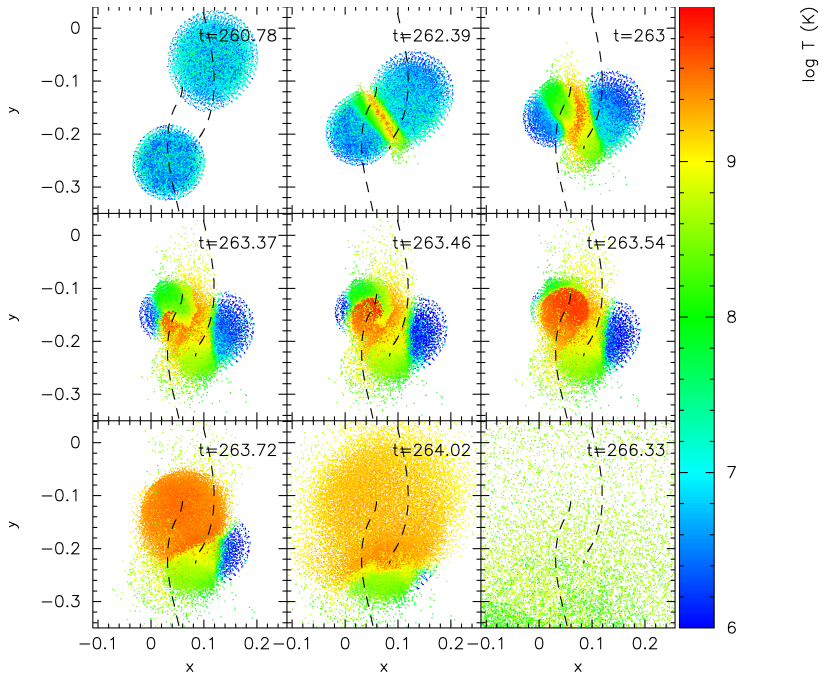

Figure 3.1: Time evolution of one of the simulations in which the dynamical interaction of two white dwarfs results in the disruption of both stars. In particular, this simulation corresponds to the case in which the interacting stars have masses $0.8\,M_{\odot}$ and $1.0\,M_{\odot}$, whereas the initial velocity is $v_{\rm ini} = 100$ km/s and the initial distance is $\Delta y = 0.3 R_{\odot}$ — that is, run number 7 in Table 3.1. The temperature of each SPH particle is also shown. The x and y axes are in units of $0.1\,R_{\odot}$. The dashed lines correspond to the trajectories of the center of mass of each intervening star. Only 1 out of 10 particles has been represented. Times (in seconds) since the beginning of the simulation are shown in the right upper corner of each panel. These figures have been done using the visualization tool SPLASH (Price, 2007).

detonation is likely to develop comprise a small number of particles and degeneracy is rapidly lifted. Consequently, in these cases the result of the dynamical interaction is not a powerful thermonuclear explosion, leading to a supernova. However, there are a few runs in which the number of particles that reach detonation conditions is large enough to ensure that a supernova occurs. This happens, for instance, in the case in which two heavy carbon-oxygen white dwarfs of masses $0.8\,M_{\odot}$ and $1.0\,M_{\odot}$ interact. The time evolution of this system is depicted in Fig. 3.1. There are other cases in which only the material of the less massive white dwarf is ejected after being tidally disrupted by the more massive one. This occurs, for instance, when the primary is a very compact oxygen-neon white dwarf. Due to the very small radius of the more massive white dwarf a sizable fraction of the less massive white dwarf is not accreted

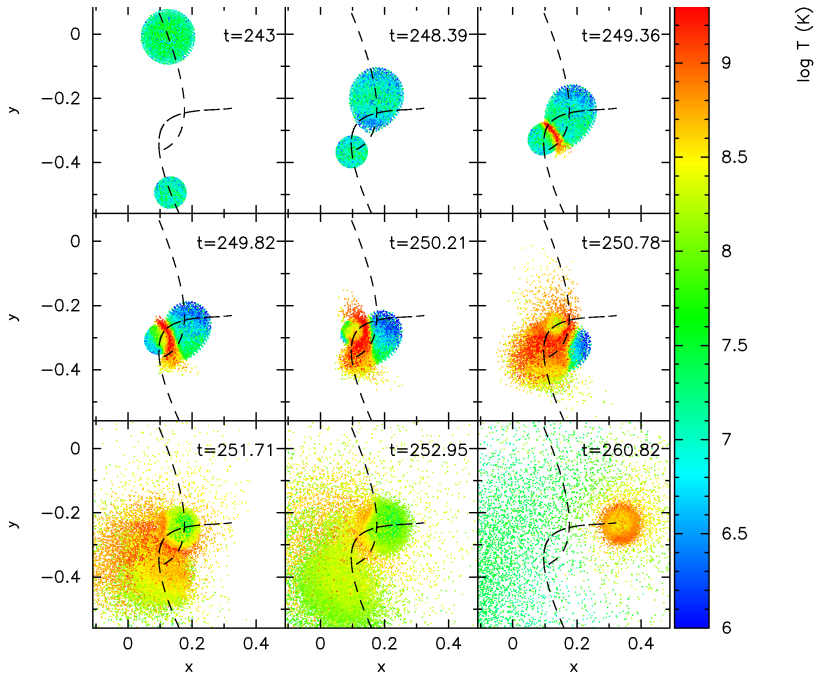

Figure 3.2: Same as Fig. 3.1 for one of the simulations in which the dynamical interaction results in the disruption of the less massive star, while the more massive white dwarf retains its identity. This specific simulation corresponds to the case in which the initial velocity is $v_{\rm ini} = 100$ km/s and the initial distance is $y_{\rm ini} = 0.3 R_\odot$, while the masses of the colliding white dwarfs are 0.8 and 1.2 $M_\odot$, respectively, corresponding to simulation number 8 in Table 3.1.

as it occurs when two white dwarfs with smaller mass contrast interact but, instead, in this case the oxygen-neon white dwarf is barely affected by the interaction, while the material of the disrupted less massive star bounces on the surface of the primary and is ejected at somewhat large velocities, of the order of 10^4 km/s. Fig. 3.2 shows an example of the temporal evolution in these cases. Specifically, this figure displays the time evolution in the case in which a 0.8 $M_\odot$ carbon-oxygen white dwarf and a 1.2 $M_\odot$ oxygen-neon white dwarf interact. Finally, there are other simulations in which both stars are disrupted as well although there is not a large mass contrast. This occurs mainly for the simulations involving two helium white dwarfs. Fig. 3.3 illustrates the case in which an extremely low mass white dwarf of mass 0.2 $M_\odot$ white dwarf is tidally disrupted by another helium white dwarf of mass 0.4 $M_\odot$, and its material is ejected from the system. Finally, it is interesting to note as well that in all these simulations the shocked region is well resolved by our simulations — see Figs. 3.1, 3.2, and 3.3.

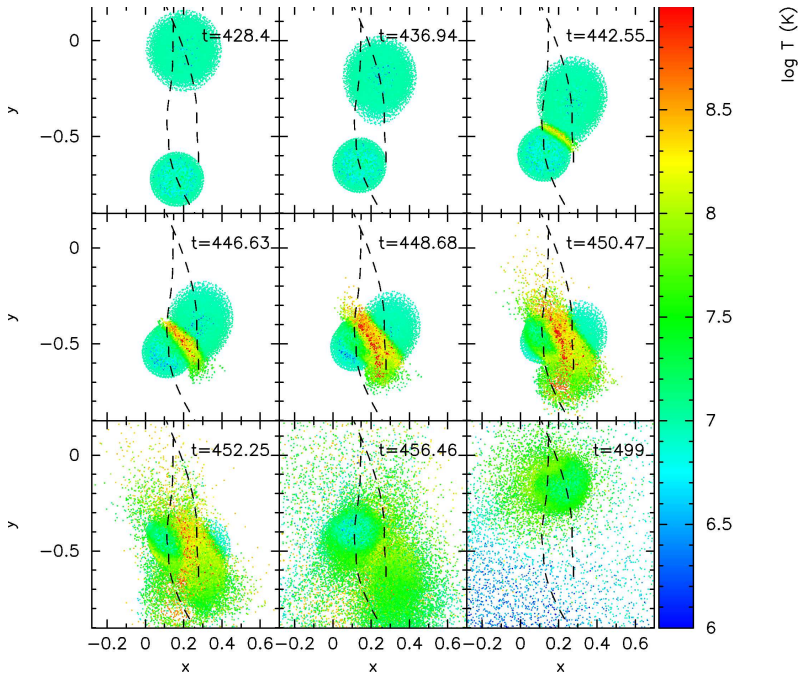

Figure 3.3: Same as Fig. 3.1 for the simulation in which two helium white dwarfs are involved. In this case the dynamical interaction results in the tidal disruption of an extremely low mass white dwarf of mass $0.2\,M_{\odot}$ in the gravitational field of a $0.4\,M_{\odot}$ helium white dwarf. The initial conditions of this specific simulation are $v_{\rm ini} = 75$ km/s and $y_{\rm ini} = 0.3R_{\odot}$, corresponding to run number 37 in Table 3.2.

3.3.2 Overview of the simulations

Tables 3.1 and 3.2 list all the simulations performed in this work, grouped as a function of the initial positions and velocities. In particular, Table 3.1 lists the kinematical properties of the simulations in which a $0.8\,M_{\odot}$ carbon-oxygen white dwarf is involved, whereas in Table 3.2 we display the same information for the simulations in which a light-weight ($0.4\,M_{\odot}$) helium white dwarf is considered. Note that these simulations complement those of Lorén-Aguilar et al. (2010), in which the interaction of two white dwarfs of masses 0.6 and $0.8\,M_{\odot}$ was studied. Thus, the present set of simulations, when complemented with those of Lorén-Aguilar et al. (2010), encompasses the most plausible range of white dwarf masses.

In both tables we list the masses of the interacting white dwarfs (second column) and the outcome of the dynamical interaction (third column). The fourth column shows if the physical conditions for a detonation are met during the dynamical interaction, and if as a consequence of the interaction the material of the less massive white dwarf is ejected (1), or if both stars are totally disrupted (2) — fifth column.

Table 3.1: Kinematical properties of the simulations reported here involving a $0.8\,M_\odot$ white dwarf.

Run	M_1+M_2 ($M_\odot$)	Outcome	Detonation	Ejection	E (10^{48} erg)	L (10^{50} erg s)	$r_{\max}$ ($R_\odot$)	$r_{\min}$ ($R_\odot$)	ε	β
$v_{\rm ini}=75$ km/s		$\Delta y=0.4\,R_\odot$								
1	0.8+0.6	DC	Yes	No	−4.12	2.80	4.48×10^{-1}	6.72×10^{-3}	0.970	2.83
2	0.8+0.8	DC	Yes	No	−5.49	3.28	4.49×10^{-1}	5.88×10^{-3}	0.974	3.06
3	1.0+0.8	DC	Yes	2	−6.88	3.64	4.49×10^{-1}	5.21×10^{-3}	0.977	3.07
4	1.2+0.8	DC	Yes	1	−8.26	3.93	4.48×10^{-1}	4.70×10^{-3}	0.980	2.98
$v_{\rm ini}=100$ km/s		$\Delta y=0.3\,R_\odot$								
5	0.8+0.6	DC	Yes	No	−5.05	2.81	3.64×10^{-1}	6.76×10^{-3}	0.964	2.81
6	0.8+0.8	DC	Yes	No	−6.76	3.28	3.63×10^{-1}	5.90×10^{-3}	0.968	3.05
7	1.0+0.8	DC	Yes	2	−8.47	3.64	3.63×10^{-1}	5.23×10^{-3}	0.972	3.06
8	1.2+0.8	DC	Yes	1	−10.1	3.93	3.63×10^{-1}	4.71×10^{-3}	0.974	2.97
$v_{\rm ini}=100$ km/s		$\Delta y=0.4\,R_\odot$								
9	0.8+0.6	LC	Yes	No	−4.06	3.74	4.49×10^{-1}	1.21×10^{-2}	0.948	1.57
10	0.8+0.8	LC	Yes	No	−5.42	4.37	4.50×10^{-1}	1.05×10^{-2}	0.954	1.71
11	1.0+0.8	LC	Yes	No	−6.80	4.85	4.50×10^{-1}	9.35×10^{-3}	0.959	1.71
12	1.2+0.8	LC	Yes	No	−8.18	5.24	4.49×10^{-1}	8.42×10^{-3}	0.963	1.66
$v_{\rm ini}=150$ km/s		$\Delta y=0.3\,R_\odot$								
13	0.8+0.6	LC	No	No	−4.88	4.21	3.68×10^{-1}	1.56×10^{-2}	0.919	1.22
14	0.8+0.8	LC	Yes	No	−6.56	4.91	3.67×10^{-1}	1.35×10^{-2}	0.929	1.33
15	1.0+0.8	LC	Yes	No	−8.25	5.46	3.66×10^{-1}	1.20×10^{-2}	0.937	1.33
16	1.2+0.8	LC	Yes	No	−9.95	5.90	3.66×10^{-1}	1.08×10^{-2}	0.943	1.30
$v_{\rm ini}=150$ km/s		$\Delta y=0.4\,R_\odot$								
17	0.8+0.6	LC	No	No	−3.89	5.60	4.53×10^{-1}	2.81×10^{-2}	0.883	0.68
18	0.8+0.8	LC	No	No	−5.22	6.55	4.54×10^{-1}	2.45×10^{-2}	0.898	0.73
19	1.0+0.8	LC	No	No	−6.57	7.28	4.53×10^{-1}	2.16×10^{-2}	0.909	0.74
20	1.2+0.8	LC	Yes	No	−7.93	7.86	4.52×10^{-1}	1.94×10^{-2}	0.918	0.72
$v_{\rm ini}=200$ km/s		$\Delta y=0.3\,R_\odot$								
21	0.8+0.6	LC	No	No	−4.64	5.62	3.75×10^{-1}	2.86×10^{-2}	0.858	0.66
22	0.8+0.8	LC	No	No	−6.28	6.55	3.73×10^{-1}	2.48×10^{-2}	0.875	0.73
23	1.0+0.8	LC	No	No	−7.94	7.28	3.72×10^{-1}	2.18×10^{-2}	0.889	0.73
24	1.2+0.8	LC	Yes	No	−9.61	7.86	3.70×10^{-1}	1.96×10^{-2}	0.900	0.71
$v_{\rm ini}=200$ km/s		$\Delta y=0.4\,R_\odot$								
25	0.8+0.6	O	No	No	−3.65	7.47	4.61×10^{-1}	5.23×10^{-2}	0.796	0.36
26	0.8+0.8	O	No	No	−4.94	8.74	4.60×10^{-1}	4.54×10^{-2}	0.820	0.40
27	1.0+0.8	O	No	No	−6.26	9.70	4.58×10^{-1}	3.99×10^{-2}	0.840	0.40
28	1.2+0.8	O	No	No	−7.60	10.50	4.57×10^{-1}	3.56×10^{-2}	0.855	0.39
$v_{\rm ini}=300$ km/s		$\Delta y=0.3\,R_\odot$								
29	0.8+0.6	O	No	No	−3.97	8.39	4.02×10^{-1}	6.96×10^{-2}	0.705	0.27
30	0.8+0.8	O	No	No	−5.47	9.32	3.96×10^{-1}	6.02×10^{-2}	0.736	0.30
31	1.0+0.8	O	No	No	−7.04	10.90	3.90×10^{-1}	5.27×10^{-2}	0.762	0.30
32	1.2+0.8	O	No	No	−8.64	11.80	3.86×10^{-1}	4.69×10^{-2}	0.783	0.30
$v_{\rm ini}=300$ km/s		$\Delta y=0.4\,R_\odot$								
33	0.8+0.6	O	No	No	−2.94	11.20	5.01×10^{-1}	1.35×10^{-1}	0.576	0.14
34	0.8+0.8	O	No	No	−4.13	13.10	4.89×10^{-1}	1.15×10^{-1}	0.620	0.16
35	1.0+0.8	O	No	No	−5.37	14.62	4.82×10^{-1}	9.97×10^{-2}	0.657	0.16
36	1.2+0.8	O	No	No	−6.63	15.71	4.76×10^{-1}	8.81×10^{-2}	0.688	0.16

Table 3.2: Kinematical properties of the simulations reported here involving a $0.4\,M_\odot$ white dwarf.

Run	M_1+M_2 ($M_\odot$)	Outcome	Detonation	Ejection	E (10^{48} erg)	L (10^{50} erg s)	$r_{\max}$ ($R_\odot$)	$r_{\min}$ ($R_\odot$)	ε	β
$v_{\rm ini}=75$ km/s		$\Delta y=0.3\,R_\odot$								
37	0.2+0.4	DC	Yes	1	−0.84	0.82	3.65×10^{-1}	8.94×10^{-3}	0.952	3.97
38	0.4+0.4	DC	Yes	2	−1.69	1.23	3.64×10^{-1}	6.65×10^{-3}	0.964	4.21
$v_{\rm ini}=75$ km/s		$\Delta y=0.4\,R_\odot$								
39	0.2+0.4	LC	Yes	No	−0.67	1.09	4.51×10^{-1}	1.60×10^{-2}	0.931	2.21
40	0.4+0.4	DC	Yes	2	−1.35	1.64	4.50×10^{-1}	1.19×10^{-2}	0.948	2.35
41	0.8+0.4	DC	Yes	1	−2.73	2.18	4.49×10^{-1}	7.85×10^{-3}	0.966	2.93
42	1.2+0.4	DC	Yes	1	−4.12	2.45	4.48×10^{-1}	5.84×10^{-3}	0.974	3.26
$v_{\rm ini}=100$ km/s		$\Delta y=0.3\,R_\odot$								
43	0.2+0.4	LC	Yes	No	−0.81	1.09	3.68×10^{-1}	1.62×10^{-2}	0.916	2.19
44	0.4+0.4	DC	Yes	2	−1.65	1.64	3.66×10^{-1}	1.20×10^{-2}	0.937	2.34
45	0.8+0.4	DC	Yes	1	−3.35	2.18	3.64×10^{-1}	7.88×10^{-3}	0.958	2.92
46	1.2+0.4	DC	Yes	1	−5.07	2.45	3.63×10^{-1}	5.88×10^{-3}	0.968	3.23
$v_{\rm ini}=100$ km/s		$\Delta y=0.4\,R_\odot$								
47	0.2+0.4	LC	No	No	−0.64	1.46	4.55×10^{-1}	2.93×10^{-2}	0.879	1.21
48	0.4+0.4	LC	Yes	No	−1.31	2.18	4.53×10^{-1}	2.16×10^{-2}	0.909	1.29
49	0.8+0.4	DC	Yes	1	−2.68	2.91	4.51×10^{-1}	1.42×10^{-2}	0.939	1.62
50	1.2+0.4	DC	Yes	1	−4.07	3.27	4.50×10^{-1}	1.05×10^{-2}	0.954	1.80
$v_{\rm ini}=150$ km/s		$\Delta y=0.3\,R_\odot$								
51	0.2+0.4	LC	No	No	−0.74	1.64	3.81×10^{-1}	3.84×10^{-2}	0.818	0.92
52	0.4+0.4	LC	Yes	No	−1.55	2.46	3.75×10^{-1}	2.81×10^{-2}	0.861	1.00
53	0.8+0.4	DC	Yes	1	−3.22	3.27	3.69×10^{-1}	1.83×10^{-2}	0.906	1.26
54	1.2+0.4	DC	Yes	1	−4.92	3.68	3.67×10^{-1}	1.35×10^{-2}	0.929	1.41
$v_{\rm ini}=150$ km/s		$\Delta y=0.4\,R_\odot$								
55	0.2+0.4	O	No	No	−0.58	2.18	4.70×10^{-1}	7.14×10^{-2}	0.736	0.50
56	0.4+0.4	O	No	No	−1.21	3.28	4.62×10^{-1}	5.16×10^{-2}	0.799	0.54
57	0.8+0.4	LC	Yes	No	−2.55	4.37	4.56×10^{-1}	3.30×10^{-2}	0.864	0.70
58	1.2+0.4	LC	Yes	No	−3.91	4.91	4.54×10^{-1}	2.44×10^{-2}	0.898	0.78
$v_{\rm ini}=200$ km/s		$\Delta y=0.3\,R_\odot$								
59	0.2+0.4	O	No	No	−0.65	2.18	4.07×10^{-1}	7.31×10^{-2}	0.695	0.49
60	0.4+0.4	O	No	No	−1.41	3.28	3.90×10^{-1}	5.27×10^{-2}	0.762	0.53
61	0.8+0.4	LC	Yes	No	−3.03	4.36	3.78×10^{-1}	3.36×10^{-2}	0.837	0.68
62	1.2+0.4	LC	Yes	No	−4.71	4.91	3.73×10^{-1}	2.47×10^{-2}	0.876	0.77
$v_{\rm ini}=200$ km/s		$\Delta y=0.4\,R_\odot$								
63	0.2+0.4	O	No	No	−0.48	2.91	5.05×10^{-1}	1.41×10^{-1}	0.564	0.25
64	0.4+0.4	O	No	No	−1.07	4.37	4.82×10^{-1}	9.97×10^{-2}	0.657	0.28
65	0.8+0.4	O	No	No	−2.36	5.82	4.66×10^{-1}	6.23×10^{-2}	0.764	0.37
66	1.2+0.4	LC	Yes	No	−3.70	6.55	4.60×10^{-1}	4.53×10^{-2}	0.821	0.42
$v_{\rm ini}=300$ km/s		$\Delta y=0.3\,R_\odot$								
67	0.4+0.4	O	No	No	−1.01	4.91	4.87×10^{-1}	1.33×10^{-1}	0.571	0.14
68	0.8+0.4	O	No	No	−2.50	6.55	4.17×10^{-1}	8.35×10^{-2}	0.666	0.28
69	1.2+0.4	O	No	No	−4.11	7.36	3.96×10^{-1}	6.01×10^{-2}	0.737	0.32
$v_{\rm ini}=300$ km/s		$\Delta y=0.4\,R_\odot$								
70	0.8+0.4	O	No	No	−1.82	8.74	5.22×10^{-1}	1.63×10^{-1}	0.525	0.14
71	1.2+0.4	O	No	No	−3.10	9.82	4.90×10^{-1}	1.14×10^{-1}	0.621	0.17

The total energy, E, and the total angular momentum, L, of the system are listed in the sixth and seventh columns, respectively. These two quantities have been computed using the corresponding SPH prescriptions. Note as well that all the energies of the systems considered here are negative and, thus, the initial trajectories are in all cases elliptical. Therefore, the apoastron ($r_{\rm max}$), the periastron ($r_{\rm min}$) and the eccentricity (ϵ) of the orbits are also specified in this table — columns 7, 8 and 9, respectively. All these quantities have been computed using the solution of the two-body problem, assuming that the two white dwarfs are point masses. However, it is important to realize that tidal interactions subsequently modify the initial orbits, leading to different outcomes. Finally, in the last column of tables 3.1 and 3.2 we also list the so-called impact parameter, which is defined as

$$\beta = \frac{R_1 + R_2}{r_{\rm min}}, \tag{3.1}$$

This parameter is a good indicator of the strength of the interaction. In this expression R_1 is the radius of the more massive white dwarf and R_2 that of the less massive one.

3.3.3 The outcomes of the interactions

As previously said, our simulations result in three different outcomes, depending on the adopted initial conditions. Not surprisingly, we find that the most relevant physical parameter for discriminating between the three different outcomes is the periastron distance, $r_{\rm min}$. In particular, we find that as the periastron distance decreases, the outcome of the interaction changes from the formation of an eccentric binary to a lateral collision and then to a direct one. This can be seen in Fig. 3.4, where we show the different outcomes of our simulations as a function of the periastron distance and the reduced mass of the system — $\mu = M_1 M_2/(M_1 + M_2)$ — for the case in which the mass of one of the interacting white dwarfs is kept fixed to $0.8\,M_\odot$ — top panel — or to $0.4\,M_\odot$ — bottom panel. In these panels the dark grey shaded areas represent the region in which the outcome of the interaction is a direct collision, the medium grey shaded areas show the regions in which lateral collisions occur, while the light grey shaded areas display the regions in which eccentric binaries are formed. We have also labelled, for the sake of clarity, each set of simulations with the mass of the second interacting white dwarf — from $1.2\,M_\odot$ to $0.2\,M_\odot$. In this way it is better illustrated how the masses of the white dwarfs involved in the interaction affect the resulting outcome.

To gain insight in the physics of the interaction process we have proceeded as follows. It could be naively expected that a direct collision occurs when at closest approach the two intervening white dwarfs are in contact. This happens when the minimum distance between their respective centers of mass, $r_{\rm min}$, is smaller than the sum of the unperturbed radii of the white dwarfs. That is, when $r_{\rm min} \leq R_1 + R_2$,

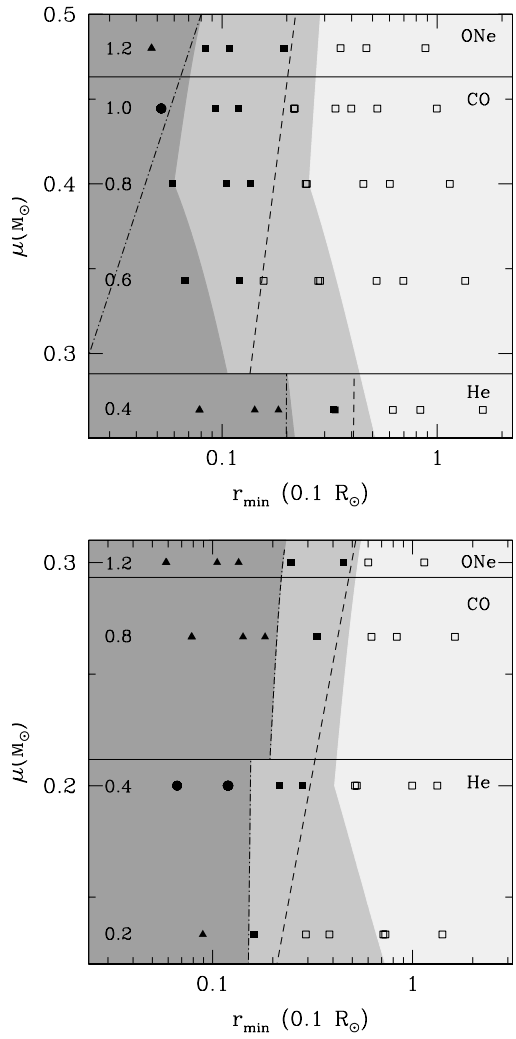

Figure 3.4: Outcomes of the simulations performed here presented in the plane defined by the reduced mass of the system and the periastron distance. The top panel displays the outcomes of the simulations in which a $0.8\,M_{\odot}$ carbon-oxygen white dwarf is involved, whilst the bottom panel shows the outcomes of the simulations in which a $0.4\,M_{\odot}$ helium white dwarf is used. The shaded areas indicate the regions for which the three different outcomes occur, as explained in the main text. Each row of simulations is also labelled with the mass of the second interacting white dwarf corresponding to the indicated reduced mass. The horizontal solid lines separate the regions of helium, carbon-oxygen and oxygen-neon white dwarfs, respectively. Hollow squares indicate those simulations in which no detonation occurs, filled squares represent those simulations in which the conditions for a detonation are met, filled triangles correspond to those simulations in which the material of the lightest white dwarf is ejected, while filled circles show the simulations in which both white dwarfs are completely destroyed. The dashed line separates the region in which no detonations occur and that in which during the dynamical interaction the physical conditions for a detonation to occur are met, while the dotted-dashed line indicates the region for which the dynamically interacting system is totally or partially disrupted. Those interactions occuring to the left of this line result in the ejection of the material of at least one component of the system.

where R_1 and R_2 are the radii of both white dwarfs at sufficiently large distances. Instead, our results show that in a direct collision the overlap between both white dwarfs at minimum distance is substantial in all cases, otherwise the less massive star survives the first mass transfer episode and a lateral collision is the outcome of the interaction, and thus this criterion is not valid. There are several reasons for this. The first one is that in direct collisions the relative velocities of the SPH particles are relatively large, or equivalently β is sufficiently large. Thus, in direct collisions the SPH particles of both stars are thoroughly mixed. The second reason is that in this approximation $r_{\rm min}$ is computed using the expression for point masses, whereas in our simulations we deal with extended bodies. Thus, in our calculations the distance at closest approach is larger than that obtained using point masses. Finally, tidal forces also decrease the periastron of the system. The interplay between all these factors is complex and, accordingly, the simplistic criterion previously explained has to be modified. To take into account that in all direct collisions substantial overlap at minimum distance occurs we adopt $r_{\rm min} \leq \lambda R_1 + R_2$, where the parameter λ indicates the degree of overlaping between both stars. The division between the regions of direct collisions and lateral collisions in Fig. 3.4 is best fitted using $\lambda \approx -0.35$, meaning that indeed the overlap has to be relatively large. We note at this point that the value of λ is the same for those simulations in which either carbon-oxygen and oxygen-neon white dwarfs are involved, but not for the case in which helium white dwarfs interact, for which the conditions for a detonation to occur are rather different. Nevertheless, this, in turn, means that this reasoning is relatively robust enough, as it does not depend much on the mass of the white dwarf.

We now go one step forward and we try to explain which is the physical mechanism that makes the difference between those simulations in which a lateral collision occurs and those simulations which end up in the formation of an eccentric binary. It would also be naively expected that a lateral collision occurs when the periastron distance is such that the less massive white dwarf fills its Roche lobe at closest approach, and consequently mass transfer from the lightest intervening white dwarf to the most massive one is enabled. To test this possibility we have used the usual analytical expression of Eggleton (1983):

$$R_{\rm L}/a = \frac{0.49 q^{2/3}}{0.6 q^{2/3} + \ln(1 + q^{1/3})} \tag{3.2}$$

where $q = M_2/M_1$ is the mass ratio of the interacting stars, and a is the binary separation, which in our case is $a = r_{\rm min}$. Nevertheless, we emphasize that Eq. (3.2) is only valid for circular orbits, while we are dealing with highly eccentric orbits. Most importantly, this expression was derived assuming that the interacting stars are spherical, which in our case is not true, as tidal deformations are important at closest approach. Thus, instead of directly using the value of $R_{\rm L}$ obtained from the expression above, we multiply it by a factor η, which takes into account all the non-

modelled effects. Hence, we expect that the limiting case separating both dynamical regimes is $R_2 = \eta R_{\rm L}$, with $R_{\rm L}$ given by Eq. (3.2).

As can be seen in Fig. 3.4, the simple argument previously explained works well when $\eta \sim 0.95$ is adopted, as all the interactions in which an eccentric binary system is formed lay in the lightest shaded area, whilst the region of lateral collisions is also nicely reproduced. It is worth noting as well that this value is the same for the simulations in which a $0.8\,M_{\odot}$ white dwarf is involved (left panel of Fig. 3.4) and those in which a $0.4\,M_{\odot}$ star is adopted (right panel in the same figure). Hence, the value of η is robust, since it does not depend on the composition of the intervening white dwarf (the $0.4\,M_{\odot}$ white dwarf is made of helium, while the $0.8\,M_{\odot}$ star is a regular carbon-oxygen white dwarf), or on the specific details of the interaction. Note also that the change in the slope of the boundary between both regions occurs at $\mu = 0.4\,M_{\odot}$ for the left panel and at $\mu = 0.2\,M_{\odot}$ for the right panel of Fig. 3.4. These values correspond to systems in which both intervening white dwarfs have equal masses. In particular, if we consider the left panel of Fig. 3.4, stars less massive than $0.8\,M_{\odot}$ have larger radii than the $0.8\,M_{\odot}$ white dwarf due to the mass-radius relation. Thus, the distances at closest approach for which a Roche-lobe overflow episode occurs are larger, and the reverse is also true. However, for white dwarfs more massive than $0.8\,M_{\odot}$ the gravitational well is deeper, and consequently lateral collisions occur for larger periastron distances. The interplay between these two effects determines the turn-off in this plane.

In Fig. 3.4 we also show the regions in the plane defined by the reduced mass and periastron distance for which the physical conditions for a detonation are met during the interaction. As shown in Figs. 3.1 and 3.2 these conditions always occur in the shocked region resulting from the very rapid accretion phase of the disrupted less massive star onto the almost rigid surface of the more massive white dwarf. The regions in which a detonation forms in the contact region between the surface of the more massive star and the material accreted from the disrupted less massive star are located to the left of the dashed line. The dotted-dashed line indicates the edge of the region for which either the less massive star or both are totally disrupted. We note, however, that if the more massive white dwarf is an oxygen-neon white dwarf the material of the less massive white dwarf is not accreted onto this star, but it bounces back. On the contrary if both stars are massive carbon-oxygen white dwarfs, the system is totally disrupted and the result of the interaction is indeed a super-Chandrasekhar Type Ia supernova.

3.4 Physical properties of the interactions

Quite generally speaking, and except for the few cases discussed previously in which the material of the less massive star is ejected, or in those cases in which both white dwarfs are entirely disrupted, in all those simulations in which a merger occurs, the

less massive white dwarf is accreted by the massive companion, and the resulting configuration consists of a central compact object surrounded by a hot corona, and a region where the debris of the interaction can be found. The properties of the debris region depend very much on the masses of the interacting white dwarfs. In particular, if a direct collision occurs, the final configuration is almost spherically symmetric, whereas in lateral collisions a thick, heavy, rotationally-supported disk is formed in all cases, but in those in which the two interacting white dwarfs have equal masses. All these findings are in agreement with those previously obtained by Lorén-Aguilar et al. (2010). We found that in these simulations little mass is ejected from the system, except in some direct collisions, namely those with rather large values of the impact parameter β — see Tables 3.1 and 3.3. The hot corona corresponds to material that has been compressed and heated during the collision, and therefore is substantially enriched in heavy elements. The resulting nucleosynthetic pattern follows closely that found in Lorén-Aguilar et al. (2010).

Table 3.3 shows some important physical quantities of the simulations in which a merger occurs but the material of the less massive white dwarf is not ejected from the remnant. That is, those simulations in which the remnant of the interaction is a single bound object, with the configuration previously described. In particular, in this table we specify the masses of the central remnant ($M_{\rm WD}$), of the corona ($M_{\rm corona}$), and of the debris region ($M_{\rm debris}$). Also listed are the ejected mass ($M_{\rm ej}$), as well as the radii of the corona and of the debris region — $R_{\rm corona}$ and $R_{\rm debris}$. We considered that the newly formed white dwarf is made of all the material which rotates as a rigid solid plus the hot corona, which rotates faster. This includes both the unperturbed more massive star and the accreted material resulting from the disrupted less massive white dwarf. Finally, we also list the maximum temperature of the central remnant at the end of our simulations — $T_{\rm max}$ — the maximum temperature achieved during the most violent phase of the merger — $T_{\rm peak}$ — and the energy released by nuclear reactions, $E_{\rm nuc}$.

As can be seen in Table 3.3, when the masses of the intervening white dwarfs are rather different — namely, when the mass difference between both stars is $\gtrsim 0.2\,M_{\odot}$ — the interaction is more violent. This is the case, for instance, of simulation number 5, in which two carbon-oxygen white dwarfs of masses $0.8\,M_{\odot}$ and $0.6\,M_{\odot}$, respectively, are involved. This occurs because in these cases the less massive white dwarf is destroyed very rapidly in the deep potential well of the more massive one. Moreover, in these simulations the more massive white dwarf has a small radius, which leads to significant accelerations of the material of the disrupted less massive white dwarf, and consequently to stronger interactions. Furthermore, when the masses of the white dwarfs are very different the resulting white dwarf accretes only a small percentage of the less massive star. If the dynamical interaction results in a lateral collision, a large amount of mass of the disrupted less massive white dwarf is incorporated to the debris region, whilst if the interaction results in a direct collision the mass ejected from the system is larger. All these physical considerations are also

Table 3.3: Hydrodynamical results for the simulations in which a collision occurs and the resulting system remains bound.

Run	Detonation ($M_\odot$)	$M_{\rm WD}$	$M_{\rm corona}$ ($M_\odot$)	$M_{\rm debris}$ ($M_\odot$)	$M_{\rm ej}$ ($M_\odot$)	$T_{\rm max}$ (K)	$T_{\rm peak}$ (K)	$R_{\rm corona}$ ($R_\odot$)	$R_{\rm debris}$ ($R_\odot$)	$E_{\rm nuc}$ (erg)
1	Yes	0.90	0.79	0.46	3.74×10^{-2}	5.35×10^{8}	4.37×10^{9}	9.64×10^{-3}	0.43	1.09×10^{49}
2	Yes	1.12	—	0.34	1.41×10^{-1}	4.69×10^{8}	5.44×10^{9}	—	0.28	4.57×10^{49}
5	Yes	0.87	0.79	0.50	3.22×10^{-2}	4.90×10^{8}	4.50×10^{9}	8.86×10^{-3}	0.22	9.81×10^{48}
6	Yes	1.13	—	0.33	1.37×10^{-1}	4.65×10^{8}	5.37×10^{9}	—	0.19	4.25×10^{49}
9	Yes	0.91	0.72	0.48	1.39×10^{-2}	4.79×10^{8}	3.03×10^{9}	8.00×10^{-3}	0.21	9.93×10^{47}
10	Yes	1.29	—	0.28	2.63×10^{-2}	4.50×10^{8}	4.20×10^{9}	—	0.21	2.27×10^{48}
11	Yes	1.12	0.89	0.64	4.64×10^{-2}	7.77×10^{8}	4.51×10^{9}	6.93×10^{-3}	0.24	1.66×10^{49}
12	Yes	1.26	0.54	0.64	1.01×10^{-1}	1.08×10^{9}	4.66×10^{9}	4.98×10^{-3}	0.21	3.67×10^{49}
13	No	0.91	0.71	0.48	7.96×10^{-3}	4.49×10^{8}	2.18×10^{9}	8.05×10^{-3}	0.22	1.49×10^{46}
14	Yes	1.30	—	0.29	8.44×10^{-3}	4.44×10^{8}	3.50×10^{9}	—	0.23	5.24×10^{47}
15	Yes	1.15	0.83	0.63	1.85×10^{-2}	7.54×10^{8}	3.89×10^{9}	6.62×10^{-3}	0.20	2.63×10^{48}
16	Yes	1.26	0.54	0.67	6.81×10^{-2}	1.07×10^{9}	4.30×10^{9}	5.02×10^{-3}	0.19	2.36×10^{49}
17	No	0.91	0.41	0.47	1.41×10^{-2}	4.36×10^{8}	1.16×10^{9}	5.44×10^{-3}	0.38	1.88×10^{41}
18	No	1.38	—	0.21	5.76×10^{-3}	3.49×10^{8}	2.54×10^{9}	—	0.25	7.95×10^{46}
19	No	1.16	0.63	0.62	1.71×10^{-2}	7.02×10^{8}	2.08×10^{9}	4.85×10^{-3}	0.37	8.17×10^{45}
20	Yes	1.31	0.44	0.66	2.70×10^{-2}	1.25×10^{9}	2.80×10^{9}	3.65×10^{-3}	0.36	1.43×10^{48}
21	No	0.92	0.42	0.46	1.39×10^{-2}	4.21×10^{8}	9.22×10^{8}	5.43×10^{-3}	0.49	1.90×10^{39}
22	No	1.33	—	0.27	4.80×10^{-3}	2.48×10^{8}	1.32×10^{9}	—	0.43	8.67×10^{43}
23	No	1.17	0.50	0.62	1.73×10^{-2}	7.56×10^{8}	1.79×10^{9}	4.81×10^{-3}	0.34	9.95×10^{45}
24	Yes	1.30	0.44	0.67	2.62×10^{-2}	1.17×10^{9}	2.74×10^{9}	3.72×10^{-3}	0.28	9.38×10^{47}
39	Yes	0.42	0.23	0.16	2.43×10^{-2}	1.21×10^{8}	2.29×10^{9}	1.41×10^{-2}	0.75	2.04×10^{48}
43	Yes	0.41	0.22	0.16	2.26×10^{-2}	1.13×10^{8}	2.42×10^{9}	1.18×10^{-2}	0.49	2.17×10^{48}
47	No	0.45	0.24	0.15	2.54×10^{-3}	1.09×10^{8}	6.83×10^{8}	1.63×10^{-2}	0.57	1.24×10^{45}
48	Yes	0.54	—	0.21	4.81×10^{-2}	8.81×10^{7}	2.68×10^{9}	—	0.55	8.49×10^{48}
51	No	0.44	0.17	0.16	5.63×10^{-3}	1.12×10^{8}	3.96×10^{8}	1.09×10^{-2}	0.65	2.75×10^{43}
52	Yes	0.67	—	0.13	4.96×10^{-3}	8.48×10^{7}	2.29×10^{9}	—	0.64	8.12×10^{47}
57	Yes	0.85	0.29	0.32	3.13×10^{-2}	4.25×10^{8}	2.50×10^{9}	9.27×10^{-3}	0.38	6.09×10^{48}
58	Yes	1.20	0.27	0.32	7.80×10^{-2}	7.74×10^{8}	2.75×10^{9}	5.34×10^{-3}	0.41	2.03×10^{49}
61	Yes	0.85	0.28	0.32	2.52×10^{-2}	4.13×10^{8}	1.98×10^{9}	9.50×10^{-3}	0.33	4.70×10^{48}
62	Yes	1.21	0.15	0.30	9.15×10^{-2}	7.96×10^{8}	2.74×10^{9}	5.77×10^{-3}	0.45	2.53×10^{49}
66	Yes	1.20	0.15	0.35	5.15×10^{-2}	7.77×10^{8}	2.46×10^{9}	3.35×10^{-3}	0.74	1.86×10^{49}

valid for the simulations in which a very massive oxygen-neon white dwarf of mass $1.2\,M_\odot$ and a $0.8\,M_\odot$ carbon-oxygen white dwarf are involved but a lateral collision occurs — namely, simulations 12, 16, 20, and 24. In these simulations we find that a larger fraction of the less massive white dwarf is ejected from the system, while the mass of the debris region is also significantly larger. On the contrary, when the mass difference between the interacting white dwarfs is smaller our calculations show the interaction is more gentle and a sizable amount of mass is accreted on the undisrupted more massive white dwarf. Finally, it is important to realize as well that in all simulations with small impact parameters, which produce lateral collisions, the number of mass transfer episodes is larger for decreasing values in the difference of masses of the interacting white dwarfs.

There is one simulation in which the remnant white dwarf is very close to the

Chandraskhar mass, namely simulation 18. In this simulation two $0.8\,M_{\odot}$ white dwarfs interact. Nevertheless, the remnant is rotating rapidly (a consequence of the conversion of orbital angular momentum in rotational velocity of the remnant), and thus the central density is not extraordinarily large. This prevents the onset of electron captures on ^{16}O in the densest regions of the remnant. Additionally, in some simulations the temperatures and densities attained during the interaction are high enough to drive a detonation. However, in these simulations the regions in which a detonation is likely to develop comprise a small number of particles and degeneracy is rapidly lifted. Consequently, in these cases the result of the dynamical interaction is not a powerful thermonuclear explosion, leading to a supernova.

There are a few simulations in which a corona is not formed. These are simulations 2, 6, 10, 14, 18, 22, 48 and 52. All these simulations correspond to interactions in which two equal-mass white dwarfs are involved (with either carbon-oxygen or helium internal chemical compositions). In these cases both white dwarfs are disrupted and merge forming a new, more massive, white dwarf. In particular, the final remnant is always $\sim 35\%$ more massive than the original white dwarf. Moreover, in these simulations mixing of the disrupted white dwarfs is extensive, and the final temperature profile of the remnant is completely different from that obtained in the rest of the simulations. In fact, the final remnant is isothermal and very hot. Since the nuclear energy release in these simulations is modest, these very high temperatures are the result of compression of the disrupted stars.

Table 3.4 displays the results obtained in those simulations in which either the material of the less massive star is not accreted by the more massive white dwarf, and thus goes to the debris region or is ejected, or those calculations in which both stars are totally disrupted. Specifically, for each run we first list if a remnant white dwarf exists, the corresponding mass of the remnant white dwarf, the mass of the debris region, the ejected mass, the velocity of the ejecta, the maximum and peak temperatures — as previously defined — attained during the dynamical interaction, and the nuclear energy released.

As can be seen, in most of these simulations a $0.4\,M_{\odot}$ helium white dwarf is involved, although there are a few runs in which the intervening star is an otherwise regular, not extremely massive, $0.8\,M_{\odot}$ carbon-oxygen white dwarf. This is the case of simulations 3, 4, 7 and 8. This can be easily understood as the combination of two factors. On one hand, the material of the disrupted less massive helium white dwarf has a reduced Coulomb barrier and, hence, nuclear reactions are more easily driven by the dynamical interaction. On the other, a light-weight helium white dwarf has a reduced gravity and, consequently, a larger radius. Thus, it is disrupted at larger distances from the more massive white dwarf, and consequently the material flowing to the primary can be significantly compressed and heated during the interaction. All this results in an explosive behavior. However, in none of these simulations the total mass of the system is larger than Chandrasekhar's mass, and thus although a powerful nuclear outburst is powered by the conversion of gravitational energy in

Table 3.4: Hydrodynamical results for the simulations in which at least the material of one of the colliding stars does not remain bound to the remnant.

Run	Remnant	$M_{\rm WD}$ ($M_\odot$)	$M_{\rm debris}$ ($M_\odot$)	$M_{\rm ej}$ ($M_\odot$)	$v_{\rm ej}$ (km/s)	$T_{\rm max}$ (K)	$T_{\rm peak}$ (K)	$E_{\rm nuc}$ (erg)
3	No	—	—	1.80	—	—	1.70×10^{10}	1.42×10^{51}
4	Yes	1.20	0.37	0.43	6.06×10^{3}	7.89×10^{8}	9.00×10^{9}	1.35×10^{50}
7	No	—	—	1.80	—	—	1.70×10^{10}	1.72×10^{51}
8	Yes	1.20	0.39	0.41	5.95×10^{3}	7.66×10^{8}	8.51×10^{9}	1.42×10^{50}
37	Yes	0.37	0.06	0.16	3.19×10^{3}	9.16×10^{7}	2.75×10^{9}	1.61×10^{49}
38	No	—	—	0.80	—	—	4.02×10^{9}	7.45×10^{50}
40	No	—	—	0.80	—	—	4.03×10^{9}	7.24×10^{50}
41	Yes	0.78	0.02	0.41	1.22×10^{4}	2.76×10^{8}	3.57×10^{9}	3.67×10^{50}
42	Yes	1.20	0.01	0.39	1.30×10^{4}	7.08×10^{8}	3.97×10^{9}	3.76×10^{50}
44	No	—	—	0.80	—	—	4.06×10^{9}	7.38×10^{50}
45	Yes	0.77	0.02	0.41	1.22×10^{4}	3.05×10^{8}	3.66×10^{9}	3.66×10^{50}
46	Yes	1.20	0.01	0.39	1.32×10^{4}	7.14×10^{8}	4.18×10^{9}	3.93×10^{50}
49	Yes	0.79	0.01	0.40	1.21×10^{4}	2.63×10^{8}	3.57×10^{9}	3.46×10^{50}
50	Yes	1.20	0.01	0.39	1.29×10^{4}	6.89×10^{8}	3.58×10^{9}	3.67×10^{50}
53	Yes	0.80	0.01	0.40	1.15×10^{4}	2.03×10^{8}	3.54×10^{9}	3.16×10^{50}
54	Yes	1.20	0.01	0.40	1.27×10^{4}	6.99×10^{8}	3.62×10^{9}	3.58×10^{50}

thermal energy, and a significant amount of nuclear energy is released (of the order of a few times 10^{50} erg) in most cases this energy is invested in ejecting the shocked material (approximately $0.4\,M_\odot$) at significant velocities (typically 10^4 km/s). Of these calculations there are two (namely, runs 3 and 7) in which the outcome is likely a super-Chandrasekhar Type Ia supernova, since in this case both stars are regular carbon-oxygen white dwarfs, although rather massive ($1.0\,M_\odot$ and $0.8\,M_\odot$, respectively), the peak temperatures are very large — in excess of 10^{10} K, and no remnant is left after the interaction. In these two simulations the released nuclear energies are very high ($\sim 1.4\times10^{51}$ erg and $\sim 1.7\times10^{51}$ erg, respectively), but these values should be considered as rough estimates, as nuclear statistical equilibrium is not implemented in our code. In runs 4 and 8 a heavy-weight oxygen-neon white dwarf tidally disrupts a carbon-oxygen white dwarf, but the more massive star remains bound, and approximately half of the material of the disrupted star remains orbiting in the debris region, whereas the rest of the material is ejected at considerably large velocities ($\sim 6\times10^3$ km/s). In these two cases the nuclear energy released is somewhat smaller, of the order of 1.4×10^{50} erg.

All this is illustrated in a different way in Fig. 3.5, where we show, for the case in which a $0.8\,M_\odot$ carbon-oxygen white dwarf is involved, the fraction of mass of the

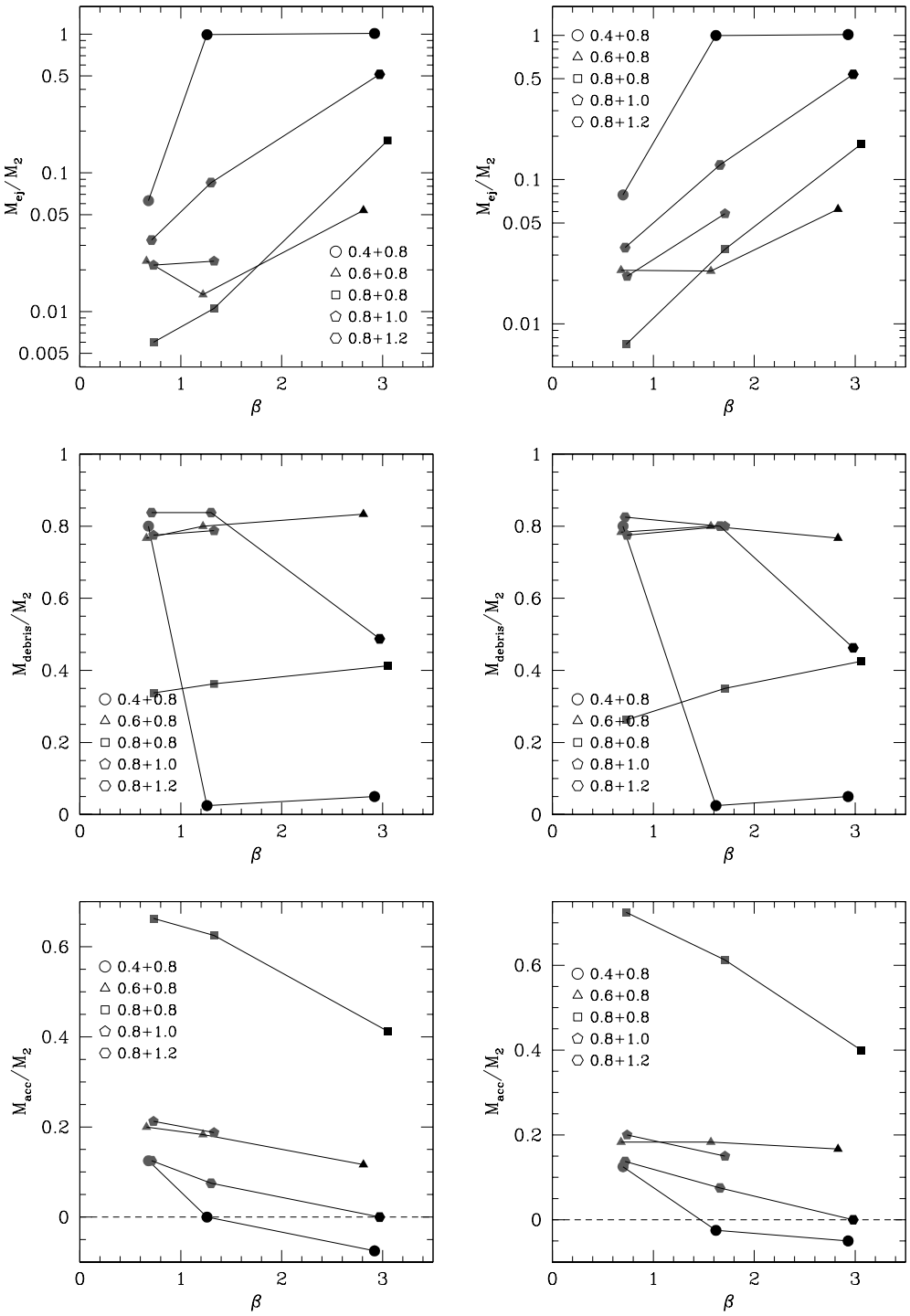

Figure 3.5: Fraction of mass of the less massive white dwarf ejected (top panels), fraction of the disrupted star that forms the debris region (middle panels) and fraction of mass which is accreted onto the more massive white dwarf (bottom panels) as a function of the impact parameter β, for the simulations in which a $0.8\,M_{\odot}$ white dwarf is involved and a merger occurs. The left panels correspond to the simulations in which $\Delta y = 0.3\,R_{\odot}$ was adopted, whereas in the right panels the simulations in which $\Delta y = 0.4\,R_{\odot}$ was used are displayed. The masses of the intervening white dwarfs and the meaning of the symbols can be found in the respective insets. The grey symbols indicate a lateral collision, while the black ones indicate a direct collision. See text for additional details.

less massive white dwarf ejected during the interaction — top panels — the fraction of the disrupted star that forms the debris region — middle panels — and the mass fraction accreted by the undisrupted massive white dwarf — bottom panels — as a function of the impact parameter, β. The black, solid symbols are used to depict a direct collision, while the grey ones indicate a lateral one. Note that direct collisions always occur for large values of β. The left panels show the results obtained when $\Delta y = 0.3\,R_{\odot}$, while the right panels display the results when $\Delta y = 0.4\,R_{\odot}$.

We start discussing the top panels of Fig. 3.5. As can be seen in these panels, the fraction of mass ejected during the interaction is small when a lateral collision occurs, of the order of 10% at most. Moreover, for a given set of masses, the mass ejected during the interaction increases for increasing values of β. The only exception is the case in which two white dwarfs of masses $0.8\,M_{\odot}$ and $0.6\,M_{\odot}$ interact. For these runs the ejected mass first decreases slightly as β increases, and then increases, as in the rest of the simulations. It is important to realize that the mass ejected from the system depends noticeably not only on the masses of the interacting white dwarfs, but also on the peak temperatures achieved during the first and most violent moments of the interaction — which are larger when both stars are rather massive and have similar masses — as well as on other details of each simulation, like the chemical composition of the interacting white dwarfs. This explains why we obtain in this case a different behavior. Note as well that the mass ejected in direct collisions is considerably larger, and in some extreme cases — for instance, in the case in which a $0.8\,M_{\odot}$ and a $0.4\,M_{\odot}$ white dwarf interact — all the mass of the less massive star is ejected from the system. Additionally, comparing the top left and right panels it turns out that all this is nearly independent of the adopted initial distance along the y-axis, Δy. This can be easily understood. If β is fixed, then all that Δy controls is the eccentricity of the encounter, and the eccentricity varies very little for the Δy values chosen.

Now we turn our attention to the mass of the debris region — middle panels of Fig. 3.5. As can be seen, when the mass contrast is large (say $\gtrsim 0.3\,M_{\odot}$) the mass of the debris region decreases for increasing values of β, whereas in all other cases the fraction of the less massive white dwarf which goes to form the debris region slightly increases as for larger values of β. Note as well that, as it occurs with the mass ejected from the system, the general trend is nearly independent of the adopted value of Δy. Finally, we discuss the mass accreted by the more massive white dwarf — bottom panels of Fig. 3.5. As previously mentioned, the final mass of the remnant white dwarf is the mass of the undisrupted massive component of the system and the mass of the hot corona that is formed during the interaction. Our simulations demonstrate that for strong impacts — or, equivalently, large values of β — the accreted mass decreases substantially as β increases. Actually, the accreted mass can be negative for relatively large values of β. This means that actually some material of the more massive white dwarf is removed during interaction and is ejected or incorporated into the debris region. This occurs for the case in which a $0.4\,M_{\odot}$

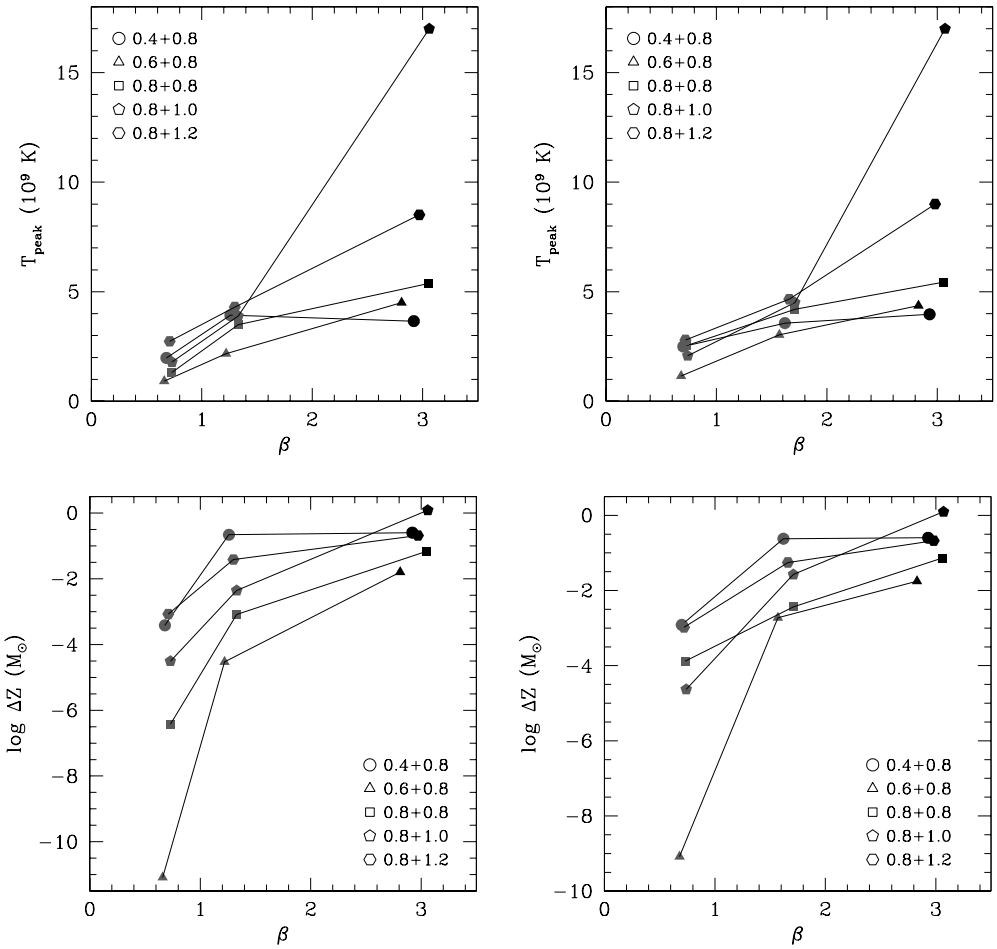

Figure 3.6: Peak temperature achieved during the interaction (top panels) and metallicity enhancement (bottom panels) as a function of the impact parameter β, for the simulations in which a $0.8\,M_\odot$ white dwarf is involved and a merger occurs. The left panels correspond to the simulations in which $\Delta y = 0.3\,R_\odot$ was adopted, whereas in the right panels the simulations in which $\Delta y = 0.4\,R_\odot$ was used are displayed. The masses of the merging white dwarfs and the meaning of the symbols can be found in the respective insets. As in Fig. 3.5 the black symbols indicate a direct collision, while the grey ones are used to display lateral ones.

helium white dwarf interacts with a $0.8\,M_{\odot}$ carbon-oxygen one. In the rest of the cases — except in that in which two equal-mass $0.8\,M_{\odot}$ interact — the accreted mass is $\sim 20\%$ in lateral collisions and much smaller in direct ones. As mentioned, the exception to this general rule is the previously mentioned case in which two $0.8\,M_{\odot}$ white dwarfs collide. In this case the fraction of mass incorporated to the remnant is considerably larger, typically $\sim 50\%$. Finally, we emphasize that, again, all these considerations are independent of Δy, for the same reason previously discussed.

Finally, to close this section we discuss Fig. 3.6, where we show the peak temperatures reached during the interactions in which a $0.8\,M_{\odot}$ white dwarf is involved, as a function of the impact parameter β — top panels — and the corresponding metallicity enhancements due to nuclear reactions — bottom panels. As in Fig. 3.5 the left panels show the cases in which $\Delta y = 0.3\,R_{\odot}$ was adopted, whereas the right panels show the cases in which $\Delta y = 0.4\,R_{\odot}$ was used. We also use the same convention adopted in Fig. 3.5, and the grey symbols indicate a lateral collision, while the black ones denote a direct one. As in Fig. 3.5 the masses of the colliding white dwarf are indicated in the insets of each figure. As can be seen in this figure, the peak temperatures reached during the interaction — top panels — increase for increasing values of β in almost all cases. It is worth noticing that, except for the case in which a $0.8\,M_{\odot}$ and a $1.0\,M_{\odot}$ white dwarfs interact, the relationship between $T_{\rm peak}$ and β is almost linear. Note that in the case in which two rather massive carbon-oxygen white dwarfs of masses $1.0\,M_{\odot}$ and $0.8\,M_{\odot}$ directly collide the resulting peak temperature is rather large, $T_{\rm peak} \simeq 1.7 \times 10^{10}$. As previously found for the masses ejected from the system, accreted to the central remnant, and incorporated to the debris region, the behavior of the peak temperature as a function of β is almost independent of the adopted value of Δy. Another important characteristic is that, in general, the larger the total mass of the system, the higher the peak temperature reached during the interaction. Additionally, we find that the more violent the interaction — and, consequently, the larger the mass transfer rate — the higher the peak temperatures are. This is a natural consequence of the matter of the disrupted less massive star being more rapidly compressed in these interactions. We now turn our attention to the bottom panels of this figure, were we show the metallicity enhancement, ΔZ, resulting from our simulations. Here we define ΔZ as the sum of the mass abundances of all elements that were not present in the original white dwarfs plus helium. For example, if the two intervening white dwarfs are made of carbon-oxygen ΔZ stands for the sum of the abundances of all elements heavier than oxygen. As can be seen in these panels, the metallicity enhancement increases abruptly until a critical value of β, while for values of β larger than the critical one the metallicity enhancement also increases but with a shallower slope. Examining the left and right panels of Fig. 3.6 it turns out that this critical value lies between $\beta \sim 1.2$ and ~ 1.6. All this is, obviously, the result of the high temperatures reached during the dynamical interactions, and hence the metallicity enhancement shows the same overall behavior observed for the peak temperatures. However, due to the strong dependence of the thermonuclear

Table 3.5: Mass abundances of selected chemical elements (Mg, Si, and Fe), for the simulations in which a $0.8\,M_\odot$ and a $0.6\,M_\odot$ white dwarfs collide and form a bound remnant.

Run	1	5	9	13	17	21
β	2.83	2.81	1.57	1.22	0.68	0.66
$T_{\rm peak}$	4.37×10^9	4.50×10^9	3.03×10^9	2.18×10^9	1.16×10^9	9.22×10^8
Maximum abundances						
Mg	2.36×10^{-1}	2.33×10^{-1}	2.33×10^{-1}	2.12×10^{-1}	8.00×10^{-11}	1.95×10^{-14}
Si	5.86×10^{-1}	5.76×10^{-1}	2.39×10^{-1}	1.43×10^{-1}	1.31×10^{-16}	0
Fe	3.54×10^{-3}	1.06×10^{-3}	0	0	0	0
Hot corona						
$\langle$Mg$\rangle$	1.98×10^{-7}	4.14×10^{-7}	9.87×10^{-8}	1.53×10^{-12}	0	0
$\langle$Si$\rangle$	1.50×10^{-9}	6.04×10^{-9}	5.51×10^{-10}	6.64×10^{-17}	0	0
$\langle$Fe$\rangle$	0	0	0	0	0	0
Debris region						
$\langle$Mg$\rangle$	2.97×10^{-3}	2.74×10^{-3}	1.16×10^{-3}	2.48×10^{-5}	1.04×10^{-14}	2.28×10^{-18}
$\langle$Si$\rangle$	7.17×10^{-3}	5.71×10^{-3}	5.84×10^{-4}	1.16×10^{-5}	0	0
$\langle$Fe$\rangle$	5.14×10^{-7}	2.60×10^{-7}	0	0	0	0
Ejecta						
$\langle$Mg$\rangle$	5.92×10^{-2}	5.81×10^{-2}	1.58×10^{-2}	5.72×10^{-10}	6.38×10^{-18}	3.24×10^{-17}
$\langle$Si$\rangle$	1.27×10^{-1}	1.29×10^{-1}	9.27×10^{-3}	3.84×10^{-14}	0	0
$\langle$Fe$\rangle$	2.16×10^{-6}	3.15×10^{-6}	0	0	0	0

reaction rates on temperature the slopes of the relationship between ΔZ and β are much steeper (note that the bottom panels of Fig. 3.6 have a logarithmic scale).

It is as well interesting to note that the nucleosynthetic endpoint depends sensitively on β, as it should be expected. This is illustrated in Table 3.5 where we list the abundances of some selected chemical species for the simulations in which a $0.8\,M_\odot$ and a $0.6\,M_\odot$ white dwarfs collide and form a bound remnant, which is a representative case of the calculations reported here. Specifically, for these runs we list the respective impact parameter, the peak temperature reached during the interaction and the abundances (by mass) of magnesium, silicon and iron in the hot corona, in the debris region and in the ejecta. We also list the maximum abundances of these elements found in the entire remnant. We note that these abundances are in line with those found by Lorén-Aguilar et al. (2010). The first thing to be noted in this table is that the larger the value of β — and, consequently, of $T_{\rm peak}$ — the more extensive nuclear processing is and the larger the maximum abundances of these elements. Secondly, it is important to realize that the average abundances of these elements are largest in the ejecta, while they are rather small in the hot corona and have sizeable values in the debris region. This, in turn, is a consequence of the very intensive nuclear processing of the shocked material hitting the rigid surface of the

Table 3.6: ^{56}Ni production in the collisions that have undergone a detonation.

Run	Ejection	$M_{\rm Ni}$ ($M_\odot$)	L erg/s
1	No	8.65×10^{-8}	1.79×10^{36}
2	No	4.47×10^{-3}	9.23×10^{40}
3	2	7.25×10^{-1}	1.50×10^{43}
4	1	6.60×10^{-2}	1.36×10^{42}
5	No	2.74×10^{-8}	5.66×10^{35}
6	No	3.67×10^{-3}	7.58×10^{40}
7	2	7.15×10^{-1}	1.48×10^{43}
8	1	6.32×10^{-2}	1.31×10^{42}
9	No	0	1.63×10^{10}
10	No	4.52×10^{-10}	9.33×10^{33}
11	No	7.94×10^{-7}	1.64×10^{37}
12	No	1.09×10^{-5}	2.25×10^{38}
14	No	7.44×10^{-16}	1.54×10^{28}
15	No	1.56×10^{-13}	3.22×10^{30}
16	No	9.70×10^{-10}	2.00×10^{34}
20	No	0	2.31×10^{10}
24	No	0	2.31×10^{10}
37	1	1.31×10^{-9}	2.71×10^{34}
38	2	8.84×10^{-4}	1.83×10^{40}
39	No	5.57×10^{-16}	1.15×10^{28}
40	2	1.64×10^{-3}	3.39×10^{40}
41	1	8.04×10^{-4}	1.66×10^{40}
42	1	1.18×10^{-3}	2.44×10^{40}
43	No	4.97×10^{-14}	1.03×10^{30}
44	2	4.68×10^{-3}	9.67×10^{40}
45	1	7.60×10^{-4}	1.57×10^{40}
46	1	2.21×10^{-3}	4.56×10^{40}
48	No	2.76×10^{-11}	5.70×10^{32}
49	1	5.00×10^{-4}	1.03×10^{40}
50	No	9.36×10^{-4}	1.93×10^{40}
52	No	1.62×10^{-17}	3.35×10^{26}
53	1	2.00×10^{-4}	4.13×10^{39}
54	1	8.44×10^{-4}	1.74×10^{40}
57	No	6.98×10^{-14}	1.44×10^{30}
58	No	5.61×10^{-10}	1.16×10^{34}
61	No	2.37×10^{-16}	4.89×10^{27}
62	No	3.27×10^{-9}	6.75×10^{34}
66	No	7.30×10^{-12}	1.51×10^{32}

more massive white dwarf and acquiring very large velocities during the interaction, which results in the subsequent ejection of these particles. This is particularly true for runs 1 and 5. Note that for these simulations the iron and silicon abundances are very large, and that the silicon abundance is larger than that of magnesium and iron, indicating that nuclear processing has been very extensive, but has not been complete. Magnesium is the most abundant isotope in the ejecta of run 9, and its abundance decreases abruptly for succesive runs, while silicon is the most abundant element maximum in the ejecta of runs 1 and 5. For these simulations the iron abundance is also maximum, but for $\beta \lesssim 1.6$ becomes negligible. The same behavior is found for the debris region. Finally, we emphasize that the iron abundance is negligible in the hot corona, independently of the value of β, whilst the magnesium and silicon abundances are modest there.

Finally, Table 3.6 lists the mass of ^{56}Ni synthesized in those simulations in which a detonation occurs, and the corresponding energy release according to the simple scaling law of Arnett (1982):

$$L = \alpha R(t_{\rm R}) M_{\rm Ni} \ {\rm erg\,s^{-1}}, \tag{3.3}$$

where

$$R = 7.74 \times 10^{43} e^{-t_{\rm R}/8.8} + 1.43 \times 10^{43} e^{-t_{\rm R}/111} \ {\rm erg\,s^{-1}M_{\odot}^{-1}} \tag{3.4}$$

is the radioactivity luminosity per unit nickel mass at time $t_{\rm R} \sim 19.3$ days, which is the time of maximum light, and $\alpha \sim 1$ is a parameter — see, for instance, Branch (1992). As can be seen in this table the amount of ^{56}Ni synthesized in these simulations, and thus the corresponding luminosities, is small in almost all the cases, with a few exceptions, namely those simulations in which either the material of the lightest intervening white dwarf or of both stars is ejected as a consequence of the dynamical interaction. In particular, in those simulations in which both white dwarfs are disrupted as a consequence of a direct collision of two carbon-oxygen white dwarfs (runs 3 and 7, respectively) the masses of ^{56}Ni produced during the extensive nuclear burning resulting from the interaction are of the order of $M_{\rm Ni} \simeq 0.7\,M_{\odot}$. Accordingly, these simulations result in Type Ia supernovae with typical luminosities ($L \simeq 1.6 \times 10^{43}$ erg s^{-1}). In those runs in which the lightest white dwarf is made of helium and the direct collision results in the disruption of both stars (simulations 38, 40, and 44) the amount of synthesized nickel is much smaller, typically of the order of $10^{-3}\,M_{\odot}$, as are the corresponding luminosities ($L \sim 10^{40}$ erg s^{-1}), and would not be classified as Type Ia supernovae. When only one carbon-oxygen white dwarf is disrupted and ejected (runs 4, and 8) the masses of nickel synthesized are also considerably smaller ($M_{\rm Ni} \simeq 0.06\,M_{\odot}$) and the luminosities of these events are, hence, smaller as well ($L \sim 1.3 \times 10^{42}$ erg s^{-1}). Consequently, they would be classified as sub-luminous supernovae. As it occurs in those cases in which the lightest white dwarf is made of helium and both stars are disrupted, in the simulations in which only the helium white dwarf is destroyed and ejected (runs 37, 41, 42, 49, 53,

and 54) the masses of nickel are very small as well. Finally, as mentioned, in the rest of the cases, namely those simulations in which the interaction does not result in the disruption of at least one star, the masses of ^{56}Ni synthesized are negligible.

3.4.1 Comparison with previous works

Raskin et al. (2010) performed simulations of head-on and off-center collisions with initial parameters apparently similar to the simulations presented in this work, and found that $0.53\,M_{\odot}$ of nickel is produced in a $0.64\,M_{\odot} + 0.81\,M_{\odot}$ collision with impact parameter $b \simeq 1.0\,R_{\rm WD}$, whereas a negligible amount of nickel is produced in a simulation with $b \simeq 2.0\,R_{\rm WD}$, which results in a bound remnant. Our equivalent simulations are runs 1, 5 and 9, all of them involving two white dwarfs of masses $0.6\,M_{\odot}$ and $0.8\,M_{\odot}$, respectively. All these simulations result in bound remnants and minuscle amounts of nickel are produced. The simulations that most closely resemble each other are our run 5, for which the distance between the centers of mass of the two stars just before the less massive white dwarf starts transferring mass to the more massive one is $\simeq 1.9\,R_{\rm WD}$, and simulation 2 of Raskin et al. (2010) with $b \simeq 2.0\,R_{\rm WD}$. In both simulations the outcome of the interaction is a bound remnant and the amount of nickel produced during the interaction is negligible. Nevertheless, to better compare with the simulations of Raskin et al. (2010) we ran a set of additional simulations. For this set of runs we adopt as a fiducial model a head-on collision of two white dwarfs of masses $0.6\,M_{\odot}$. We emphasize that except for the masses of the colliding white dwarfs, which in our case are $0.60\,M_{\odot}$ instead of $0.64\,M_{\odot}$, this fiducial simulation is identical to their run 1 with $b = 0$. For this simulation we obtain a mass of nickel of $0.22\,M_{\odot}$, while they obtain $0.51\,M_{\odot}$. However, we note that the amount of ^{56}Ni synthesized depends very sensitively on several factors. Amongst them we mention the masses of the interacting white dwarfs, how the evolution of temperature is computed, the resolution employed in the calculations, and the adopted prescription for the artificial viscosity. We discuss them one by one.

To start with, we note that the masses of the colliding white dwarfs are slightly different in both cases and, as mentioned previously, the peak temperature reached during the interaction depends sensitively on the masses of the interacting white dwarfs, as does the mass of synthesized nickel. The second important factor to be taken into account is that the peak temperature reached during the interaction obviously depends on how the evolution of the temperature is computed. We note that for a degenerate electron gas the temperature obtained from the energy equation — see Appendix A — may be incorrect by a sizable percentage. This is the reason why for those regions we adopt a different formulation and we follow the evolution of the temperature using Eq. (A.11), which we judge is more appropriate under these conditions. Moreover, Dan et al. (2012) have shown that the peak temperature and the averaged temperature may differ by up to a factor of ~ 2 — see, for instance,

their Fig. 4. Given the extreme sensitivity of the nuclear reaction rates to the temperature this, quite naturally, translates in large variations of the mass of nickel synthesized. For instance, in our fiducial simulation we obtain a peak temperature $T_{\rm peak} \simeq 8.21 \times 10^9$ K, while Rosswog et al. (2009) obtain $T_{\rm peak} \simeq 8.90 \times 10^9$, which is similar to ours. However, the masses of ^{56}Ni synthesized in both simulations differ considerably. In particular, we obtain $0.22\,M_\odot$, whereas Rosswog et al. (2009) obtain $0.32\,M_\odot$. Also the number of SPH particles plays a significant role. To quantify this we ran an additional simulation in which we decreased the number of particles to 4×10^4, that is by a factor of 5, and we obtained that the mass of nickel synthesized in this case was $0.094\,M_\odot$. Interestingly, Rosswog et al. (2009) find that when 2×10^6 particles are employed the mass of nickel synthesized in the explosion is $0.32\,M_\odot$, which is quite similar to that found in our fiducial simulation, and Raskin et al. (2010) estimate that when 5×10^4 particles are used the nickel mass should be $\sim 0.3\,M_\odot$ which agrees relatively well with the value found in our fiducial simulation. Moreover, Rosswog et al. (2009) find that when the Eulerian hydrodynamical code FLASH is employed in the calculations the mass of nickel is considerably smaller, $0.16\,M_\odot$. Thus, our mass of nickel is bracketed by the values found by Rosswog et al. (2009). The adopted treatment of the artificial viscosity also plays a non-negligible role. To illustrate this point we also ran a series of low-resolution simulations with 4×10^4 particles, in which the parameter α in Eq. (A.6) was varied from 0.5 to 1.0 and 1.5. The resulting nickel masses are 0.017, 0.094, and $0.076\,M_\odot$, respectively. Moreover, when the Balsara switch is not employed in the calculations the mass of ^{56}Ni synthesized in the simulation with $\alpha = 0.5$ is $M_{\rm Ni} \sim 0.012 M_\odot$. Thus, depending on the adopted prescription of the artificial viscosity the mass of nickel can vary by up to a factor of ~ 5. In summary, we conclude that the mass of nickel synthesized depends sensitively on the details of the numerical codes, and that discrepancies of the order of a factor of up to ~ 3 can quite naturally arise as a consequence of the different practical implementations of the SPH formalism.

The natural question is now why we obtain such small amounts of nickel in some of our simulations when compared with the simulations of Raskin et al. (2010)? The answer to this question lays on the choice of the initial conditions. We recall that in our simulations the initial orbits correspond to a post-capture scenario and have negative energies, whereas in the simulations of Raskin et al. (2010) the energies are positive in most cases. Hence, our orbits are always elliptical, while theirs are in most cases either parabolic or hyperbolic. This is indeed at the origin of the discrepancies in the masses of nickel found in both sets of simulations. To illustrate this point we compare our direct collision of two $0.8\,M_\odot$ white dwarfs (our run 6) with simulation 4 with $b = 0$ of Raskin et al. (2010), in which two $0.81\,M_\odot$ white dwarfs collide head-on. We first note that the impact parameter quoted by Raskin et al. (2010) cannot be directly compared with that given by Eq. (3.1) because their initial orbits are open, while ours are elliptical. In our simulation we obtain a bound remnant, while Raskin et al. (2010) obtain a powerful detonation resulting in the

total disruption of the system. The respective masses of ^{56}Ni synthesized are in this case 3.67×10^{-3} and $0.84\,M_{\odot}$. However, for these specific simulations the relative velocities between both stars at contact are very different. In particular, the relative velocities are $v_{\rm rel} \simeq 4.5 \times 10^3$ km/s and 5.9×10^3 km/s, respectively. However, while in the simulation of Raskin et al. (2010) this velocity is along the line connecting the two centers of mass of the white dwarfs, in our case the velocities of each star form angles of $\sim \pm 33.6^{\circ}$ with the line connecting the two centers of mass, thus resulting in a considerably less violent collision, thus in a weaker shock, and consequently in a much smaller peak temperature and in a very small mass of synthesized nickel.

3.5 Discussion

In this chapter we have studied how the interactions of white dwarfs in dense stellar systems depend on the initial conditions and on the masses of the intervening stars. Our simulations extend those of Lorén-Aguilar et al. (2010), in which the interactions of two white dwarfs of masses 0.6 and $0.8\,M_{\odot}$ with different initial conditions were studied, and encompass the most plausible range of white dwarf masses and internal chemical compositions. In total we have simulated 71 dynamical interactions, of which 36 correspond to runs in which a regular $0.8\,M_{\odot}$ interacts with another carbon-oxygen white dwarf (of masses $0.6\,M_{\odot}$ and $1.0\,M_{\odot}$, respectively), and a $1.2\,M_{\odot}$ oxygen-neon white dwarf. In the rest of the simulations the dynamical interactions of a $0.4\,M_{\odot}$ helium white dwarf with either another helium white dwarf of mass $0.2\,M_{\odot}$, or a $0.8\,M_{\odot}$ carbon-oxygen white dwarf, or a $1.2\,M_{\odot}$ oxygen-neon white dwarf were explored. Our initial conditions have been chosen to ensure that a close encounter leading to the formation of an eccentric binary or a collision always happens.

We have found that the outcome of the interactions can be a direct collision, a lateral collision or the formation of an eccentric binary system. In direct collisions there is only one violent and dramatic mass transfer episode in which the less massive white dwarf is tidally disrupted by the more massive one on a dynamical timescale, while in a lateral collision although the less massive star is disrupted as well, it takes several orbits around the more massive white dwarf to be totally destroyed. Thus, in this case the entire disruption process occurs in a more gentle way. Moreover, we have demonstrated that the outcome of the interaction can be predicted using very basic physical principles. In particular, we have found that for a given simulation tidal forces modify the initial trajectories of the interacting stars in such a way that the distance at closest approach determines the final outcome of the dynamical interaction. Specifically, we have found that if the distance at closest approach is small enough to allow a deep contact between both white dwarfs, a direct collision is the natural outcome of the interaction. For this to occur the overlap between both stars at minimum distance must be of the order of 35% if two typical carbon-oxygen white dwarfs are considered. Else, we have demonstrated as well that lateral

collisions occur when at minimum distance the radius of the less massive white dwarf is within ~ 0.95 of the Roche lobe radius of the interacting system.

We have also characterized for which initial conditions of the dynamically interacting system the material flowing from the disrupted less massive white dwarf and accreted onto the more massive star is compressed to such an extent that reaches the conditions for a detonation to develop. Moreover, we have also studied for which initial conditions the explosion is powerful enough to result in the disruption of one or both of the interacting white dwarfs, and for which ones degeneracy is lifted and the result of the interaction is a central, more massive and very hot object surrounded by a debris region orbiting around it. Our results indicate that if the intervening stars are regular carbon-oxygen white dwarfs (or even oxygen-neon ones) detonations occur when the two components of the system are separated by less than $\sim 0.015\,R_{\odot}$ at minimum distance, and that one or both components of the system are totally disrupted and ejected to the surrounding medium if the total mass of the system is rather large, preferentially $\gtrsim 1.4\,M_{\odot}$ and the initial periastron distance is smaller than $\sim 0.005\,R_{\odot}$ — see Fig. 3.4. However, if the less massive star is a helium white dwarf the resulting detonations always result in a catastrophic output for separations at minimum distance $\lesssim 0.02\,R_{\odot}$. Two of our simulations result in a super-Chandrasekhar Type Ia supernova outburst, corresponding to direct collisions of two rather massive carbon-oxygen white dwarfs of masses $1.0\,M_{\odot}$ and $0.8\,M_{\odot}$. There are as well a few simulations in which only one carbon-oxygen white dwarf is disrupted and ejected. These simulations also result in powerful explosions, but their luminosities are considerably smaller and, thus, would probably be classified as sub-luminous supernovae. Finally, other simulations result in powerful outbursts, and lead as well to the disruption of the entire system, but involve white dwarfs with helium cores. In these cases the mass of ^{56}Ni is very small, as are the corresponding luminosities. Nevertheless, some of our simulations produce bound remnants which are close to the Chandrasekhar limit, and the subsequent evolution of these systems may eventually produce Type Ia supernovae, as the viscous evolution unbinds only a very small fraction of the material of the debris region (Schwab et al., 2012).

For those interactions resulting in a central, massive and very hot remnant we have also studied the influence of the masses of the interacting white dwarfs and of the initial conditions on the properties of the final remnants. In particular, we have studied the morphology of the resulting remnant, the peak temperatures reached during the most violent phase of the interaction, and the associated nucleosynthesis. In all these simulations a central hot white dwarf surrounded by a debris region is formed, whereas a variable amount of mass is ejected from the system. The morphology of the debris region depends mostly on the kind of collision the system undergoes. In particular, for lateral collisions the debris region is a heavy, rotationally-supported keplerian disk, whilst for direct ones the debris regions consists of a spheroid. The peak temperatures attained during the most violent phase of the accreting episode are rather high in all cases, typically of the order of 10^9 K, and can be even larger

for direct collisons, for which temperatures larger than 10^{10} K are easily reached, than for lateral interactions. This, in turn, drives extensive nucleosynthetic activity in the shocked regions. Hence, the debris region and the material ejected during the dynamical interaction are substantially enriched in heavy elements.

In summary, we have computed a comprehensive set of simulations aimed to provide a consistent framework to analyze the dynamical interactions of white dwarfs in dense stellar systems. These interactions are of interest because the collision is likely to detonate the white dwarfs, and result in a type Ia supernova outburst. Actually, in our simulations the detonation conditions are reached in a significant number of interactions, and the masses of the exploding systems show some dispersion. As a matter of fact, we find that for some simulations the detonation occurs in interacting systems for which the involved mass is larger than Chandrasekhar's mass, whereas in some other the resulting explosion is sub-Chandrasekhar. An important fact that needs to be taken into account is that it has been recently shown that such interactions might be more common than previously thought (Katz & Dong, 2012), and could even dominate the event rate. Thus, there is a renewed interest in studying these interactions, for which there was a lack of extensive calculations. Precisely, our results fill this gap, and pave the road to more extensive calculations in which the enhancement in the event rate proposed by these authors could be analyzed in more detail. Particularly, it is worth mentioning that this increase in the event rate depends on the fraction of white dwarf collisions that are expected to lead to Type Ia-like events. Given that our calculations provide the maximum separation at pericenter for various pairs of white dwarfs to produce detonations, future calculations could approach this problem on a solid basis. Finally, another open question remains to be answered yet, namely how exactly the optical signature of the explosions resulting from these dynamical interactions would look like, even if they do not result in Type Ia supernovae. Given the wide range of nickel masses produced during the interactions studied here, they may explain both some underluminous transients and relatively bright outbursts. This is, nevertheless, out of the scope of this chapter, and will be studied in the following one.

Chapter 4

On the possible observational signatures of white dwarf dynamical interactions

Here we compute the possible observational signatures of white dwarf dynamical interactions in dense stellar environments. Specifically, we compute the emission of gravitational waves, and we compare it with the sensitivity curves of planned space-borne gravitational wave detectors. We also compute the light curves for those interactions in which a detonation occurs, and one of the stars is destroyed, as well as the corresponding neutrino luminosities. We find that for the three possible outcomes of these interactions — which are the formation of an eccentric binary system, a lateral collision in which several mass transfer episodes occur, and a direct one in which just a single mass transfer episode takes place — only those in which an eccentric binary are formed are likely to be detected by the planned gravitational wave mission eLISA, while more sensitive detectors would be able to detect the signals emitted in lateral collisions. On the other hand, the light curves (and the thermal neutrino emission) of these interactions are considerably different, producing both very powerful outbursts and low luminosity events. Finally, we also calculate the X-ray signature produced in the aftermath of those interactions for which a merger occurs. We find that the temporal evolution follows a power law with the same exponent found in the case of the mergers of two neutron stars, although the total energy released is smaller.

4.1 Introduction

Close encounters of two white dwarfs in dense stellar environments, as the central regions of galaxies or the cores of globular clusters, are interesting phenomena that have several potential applications, and hence deserve close scrutiny. Among the

possible applications of these interactions we mention that it has been shown (Rosswog et al., 2009) that head-on collisions of two white dwarfs is a viable mechanism to produce Type Ia Supernovae, one of the most energetic events in the Universe. However, as seen in the previous chapter, there are situations in which the two white dwarfs interact but the interaction does not result in a powerful thermonuclear outburst leading to the complete disruption of the two stars, whereas in some other the release of nuclear energy is very modest, and finally there are other cases in which no nuclear energy is released at all. We have shown that white dwarf close encounters can have three different outcomes, depending on the initial conditions of the interaction — namely, the initial energy and angular momentum of the pair of white dwarfs, or equivalently the impact parameter and initial velocity of the pair of stars. In particular, these interactions can lead to the formation of an eccentric binary system, to a lateral collision in which several mass transfer episodes between the disrupted less massive star and the more massive one occur, and finally to a direct collision, in which only one catastrophic mass transfer event occurs. Additionally, it turns out that for these two last outcomes there is a sizable region of the parameter space for which the conditions for a detonation to occur are met, leading in some cases to the total disruption of both white dwarfs, and to a large dispersion of the nuclear energy released during the interaction.

In chapter 3 we have demonstrated that the masses of ^{56}Ni synthesized in the strongest dynamical interactions can vary by orders of magnitude, and so do the typical luminosities. Actually, the mass of ^{56}Ni obtained in the several sets of simulations performed so far, and thus the corresponding luminosities, range from those typical of macro-nova events, to sub-luminous and super-luminous supernova events. Nonetheless, it is important to realize that the spread in the mass of ^{56}Ni produced during the most violent phases of the most energetic interactions does not only depend on the adopted initial conditions but also, as previously shown and first noticed by Kushnir et al. (2013), on the adopted prescription of the artificial viscosity, and on the resolution employed in the simulations, among other (less important) factors. Additionally, one has to note that the parameter space of such dynamical interactions is huge and the complexity of the physical mechanism of the interactions is extremely high. We have chosen to account for the first point by producing a vast set of numerical simulations, but this comes of the expense of the second issue. Consequently, most likely the tidal interaction is reasonably captured in moderately-resolved SPH simulations, but combustion processes are possibly not completely well resolved. Nevertheless, although a thorough resolution study is still lacking, the masses of ^{56}Ni synthesized in the several independent sets of simulations agree within a factor of ~ 5, and the qualitative picture of the hydrodynamical evolution is quite similar in all the cases, as discussed in section 3.4.1.

In this chapter we study different observational signatures of the calculations described in chapter 3. We first discuss, in section 4.2, the methods employed to characterize the different observational characteristics. Section 4.3 is devoted to

analyze the results of our theoretical calculations. Specifically, in section 4.3.1 we study the emission of gravitational waves. It follows section 4.3.2 where we discuss the late-time light curves for those interactions which result in powerful detonations, while in section 4.3.3 we present the thermal neutrino fluxes and we assess their detectability. In section 4.3.4, we compute the fallback luminosities produced in the aftermath of those interactions which result in a central remnant surrounded by a disk. Finally, in section 4.4 we summarize our most relevant results, we discuss their significance, and we draw our conclusions.

4.2 Numerical setup

In this section we describe how we compute the emission of gravitational waves, the light curves for those events which have an explosive outcome, the neutrino fluxes, and the fallback X-ray luminosity of the remnants, for those cases in which the dynamical interaction is not strong enough to disrupt both stars. All the calculations presented in section 4.3 are the result of post-processing the SPH calculations of interacting white dwarfs of chapter 3. Since the results of these calculations is a set of trajectories of a collection of individual particles some of the usual expressions must be discretized. Here we explain how we do this.

4.2.1 Gravitational waves

We compute the gravitational wave emission in the slow-motion, weak-field quadrupole approximation (Misner et al., 1973). Specifically, we follow closely the procedure outlined in Lorén-Aguilar et al. (2005). Within this approximation the strain amplitudes can be expressed in the following way:

$$h_{jk}^{\mathrm{TT}}(t,\mathbf{x}) = \frac{G}{c^4 d}\big(A_+(t,\mathbf{x})\mathbf{e}_{+\,jk} + A_\times(t,\mathbf{x})\mathbf{e}_{\times\,jk}\big) \tag{4.1}$$

where d is the distance to the source, and the polarization tensor coordinate matrices are defined as:

$$\begin{aligned} \mathbf{e}_{+\,jk} &= \frac{1}{\sqrt{2}}[(\mathbf{e}_x)_j(\mathbf{e}_x)_k - (\mathbf{e}_y)_j(\mathbf{e}_y)_k] \\ \mathbf{e}_{\times\,jk} &= \frac{1}{\sqrt{2}}[(\mathbf{e}_x)_j(\mathbf{e}_y)_k + (\mathbf{e}_y)_j(\mathbf{e}_x)_k], \end{aligned} \tag{4.2}$$

and

$$A_+(t,\mathbf{x}) = \ddot{Q}_{xx} - \ddot{Q}_{yy}, \quad A_\times(t,\mathbf{x}) = +2\ddot{Q}_{xy} \tag{4.3}$$

for $i = 0$, and

$$A_+(t,\mathbf{x}) = \ddot{Q}_{zz} - \ddot{Q}_{yy}, \quad A_\times(t,\mathbf{x}) = -2\ddot{Q}_{yz} \tag{4.4}$$

for $i = \pi/2$, being i the angle with respect to the line of sight. In these expressions Q is the quadrupole moment of the mass distribution.

Since, as already mentioned, we are post-processing a set of SPH calculations and, hence, we deal with an ensemble of n individual SPH particles, the double time derivative of the quadrupole moment is discretized in the following way:

$$\ddot{Q}^{\rm TT}_{jk} \approx P_{ijkl}(\mathbf{N}) \sum_{p=1}^{n} m(p)[2\mathbf{v}^k(p)\mathbf{v}^l(p) + \mathbf{x}^k(p)\mathbf{a}^l(p) + \mathbf{x}^l(p)\mathbf{a}^k(p)] \quad (4.5)$$

where $m(p)$ is the mass of each SPH particle, $\mathbf{x}(p)$, $\mathbf{v}(p)$ and $\mathbf{a}(p)$ are, respectively, its position, velocity and acceleration, and

$$P_{ijkl}(\mathbf{N}) \equiv (\delta_{ij} - N_i N_k)(\delta_{jl} - N_j N_l) - \frac{1}{2}(\delta_{ij} - N_i N_j)(\delta_{kl} - N_k N_l) \quad (4.6)$$

is the transverse-traceless projection operator onto the plane ortogonal to the outgoing wave direction, $\mathbf{N}$.

To assess the detectability of the gravitational waveforms we proceed as follows. For the well defined elliptical orbits, we first accumulate the power of the signal during one year. We then compute the characteristic frequencies and amplitudes, and the signal-to-noise-ratios (SNR) according to Zanotti et al. (2003). These characteristic quantities are given by:

$$h_{\rm c} = \left[3 \int_0^\infty \frac{S_{\rm n}(f_{\rm c})}{S_n(f)} \left\langle \left|\tilde{h}(f)\right|^2 \right\rangle f\, df \right]^{1/2} \quad (4.7)$$

$$f_{\rm c} = \left[\int_0^\infty \frac{\left\langle \left|\tilde{h}(f)\right|^2 \right\rangle}{S_n(f)} f\, df \right] \left[\int_0^\infty \frac{\left\langle \left|\tilde{h}(f)\right|^2 \right\rangle}{S_{\rm n}(f)} df \right]^{-1} \quad (4.8)$$

where

$$\tilde{h}(f) = \int_{-\infty}^{\infty} e^{2\pi i f t}\, h(t)\, dt \quad (4.9)$$

is the waveform in the frequency domain, and $S_{\rm n}$ is the power spectral density of the detector. After this the root-mean-square strain noise:

$$h_{\rm rms} = \sqrt{f S_{\rm n}(f)} \quad (4.10)$$

is computed to obtain the SNR:

$$\mathrm{SNR} = \frac{h_{\rm c}}{h_{\rm rms}(f_{\rm c})}. \quad (4.11)$$

For the short-lived signals obtained in lateral collisions, we compute the SNR as in Giacomazzo et al. (2011):

$$(\mathrm{SNR})^2 = 4 \int_0^\infty \frac{\left|\tilde{h}\left(f\right)\right|^2}{S_\mathrm{n}\left(f\right)} df, \tag{4.12}$$

and we compare the product of the Fourier transform of the dimensionless strains and the square root of the frequency, $\tilde{h}(f)f^{1/2}$, with the gravitational-wave detector noise curve. Finally, for direct collisions we only compute the total energy radiated in the form of gravitational waves, since it is unlikely that these events could be eventually detected.

4.2.2 Light curves

The observable emission of those events in which some ^{56}Ni is synthesized during the interaction is powered completely by its radioactive decay and that of its daughter nucleus, ^{56}Co (Colgate & McKee, 1969). Specifically, the ^{56}Ni synthesized in the explosion decays by electron capture with a half-life of 6.1 days to ^{56}Co, which in turn decays through electron capture (81%) and β^+ decay (19%) to stable ^{56}Fe with a half-life of 77 days. The early phase is dominated by the down-scattering and the release of photons generated as γ-rays in the decays, while at late phases the optical radiation escapes freely. The peak radiated luminosity of Tpe Ia supernovae can be approximated with enough accuracy using the scaling law of Arnett (1979), as it has been done in chapter 3. It is expected to be comparable to the instantaneous rate of energy release by radioactivity at the rise time (Branch, 1992).

To model the light curves in those interactions where sizable amounts of ^{56}Ni are produced, we adopt the treatment of Kushnir et al. (2013), which provides a relation between the synthesized ^{56}Ni mass and the late-time (≈60 days after peak) bolometric light curve. Within this approach, the late-time bolometric light curve is computed numerically using a Monte Carlo algorithm, which solves the transport of photons, and the injection of energy by the γ-rays produced by the ^{56}Ni and ^{56}Co decays. To this end we first map, using kernel interpolation, our SPH data to a three-dimensional cartesian velocity grid, and then we employ the Monte Carlo code of Kushnir et al. (2013).

4.2.3 Thermal neutrinos

Since the densities reached in all the simulations are smaller than 10^{10} g cm^{-3}, the material is expected to be completely transparent to neutrinos. Moreover, as in a sizable number of close encounters the maximum temperatures are in excess of 10^9 K, copious amounts of thermal neutrinos should be emitted. We thus computed this emission taking into account the five traditional neutrino processes

— that is, electron-positron annihilation, plasmon decay, photoemission, neutrino bremsstrahlung, as well as neutrino recombination — using the prescriptions of Itoh et al. (1996).

To assess the possibility of detecting some of the emitted neutrinos we follow closely the prescriptions of Odrzywolek & Plewa (2011) and Kunugise & Iwamoto (2007). Specifically, we compute the number of events that could be eventullay observed in the Super-Kamiokande detector when the source is at a distance $d = 1$ kpc. We compute first the neutrino spectral flux:

$$\Phi(E_\nu, t) = \frac{L}{A\langle E_\nu\rangle^4} \frac{aE_\nu^2}{1+\exp^{bE_\nu/\langle E_\nu\rangle}} \tag{4.13}$$

where L is the neutrino luminosity at time t, $A = 4\pi d^2$ is the irradiated area, $\langle E_\nu\rangle = 3.15137\,T_\nu$ is the average neutrino energy at time t, $a \simeq 17.3574$ and $b \simeq 3.15137$. The values of $L(t)$ and $T_\nu(t)$ are obtained from our SPH simulations. Assuming equipartition of energy between all the emitted neutrino flavors, the number of events detected in a water Cherenkov detector can be approximated by estimating the rate of electron-neutrino neutrino scatterings. The cross section of this scattering depends on the threshold energy of recoil electrons in the experiment, $T_{\rm e}^{\rm th}$:

$$\begin{aligned}\sigma(E_\nu, T_{\rm e}^{\rm th}) &= \frac{\sigma_0}{m_{\rm e}}\left[\left(g_1^2+g_2^2\right)\left(T_{\rm e}^{\rm max}-T_{\rm e}^{\rm th}\right)-\left(g_2^2+g_1g_2\frac{m_{\rm e}}{2E_\nu}\right)\left(\frac{T_{\rm e}^{\rm max^2}-T_{\rm e}^{\rm th^2}}{E_\nu}\right)\right.\\ &+ \left.\frac{1}{3}g_2^2\left(\frac{T_{\rm e}^{\rm max^3}-T_{\rm e}^{\rm th^3}}{E_\nu^3}\right)\right],\end{aligned} \tag{4.14}$$

where $\sigma_0 \simeq 88.06\times10^{-46}\,{\rm cm}^2$,

$$T_{\rm e}^{\rm max} = \frac{2E_\nu^2}{m_{\rm e}+2E_\nu}$$

is the maximum kinetic energy of the recoil electron at a neutrino energy E_ν, $g_1 \simeq 0.73$ and $g_2 \simeq 0.23$. The time-integrated spectra is then

$$F_\nu(E_\nu) = \int \Phi(E_\nu, t)dt,$$

and the total number of events is:

$$N = nV\int F_\nu(E_\nu)\sigma(E_\nu, T_{\rm e}^{\rm th})dE_\nu,$$

where n is the number density of electrons in the water tank and V is its volume. We consider the Super-Kamiokande detector, with a fiducial volume of 22,500 tons.

4.2.4 Fallback luminosities

Another possible observational signature of these types of collisions and close encounters is the emission of high-energy photons from the fallback material in the aftermath of the interaction. As mentioned, in some cases only one of the stars intervening in the dynamical interaction is disrupted, and its material goes to form a disk orbiting the more massive white dwarf. Most of the material of these disks has circularized orbits. However, it turns out that a general feature of these interactions is that some of the SPH particles of the disk have highly eccentric orbits. After some time this material interacts with the rest of the disk. As shown by Rosswog (2007), the relevant timescale for these particles is not the viscous one, but instead their evolution is set by the distribution of eccentricities. To compute how these particles interact with the newly formed disk, and which are the corresponding fallback accretion luminosities, we follow closely the approach described in Rosswog (2007). For the particles that have been launched into eccentric orbits, but are still bound to the remnant, we compute the following quantities. These particles are treated as test masses in the gravitational field of the enclosed mass, M. That is, the trajectory of each particle is approximated as that of a point-mass two-body problem. For each of these particles of mass $m_i \ll M$, the angular momentum, J_i, and their energy, E_i, can be determined. We compute first the time τ_i elapsed from its present radius, r_i, until its energy is dissipated at the disk radius $R_{\rm dis}$,

$$\tau_i = \begin{cases} I_{r_i, r_{{\rm max},i}} + I_{r_{{\rm max},i}, R_{\rm dis}} & \text{for } \mathbf{v}_i \cdot \mathbf{r}_i > 0 \\ I_{r_i, R_{\rm dis}} & \text{for } \mathbf{v}_i \cdot \mathbf{r}_i < 0 \end{cases} \tag{4.15}$$

where $\mathbf{r}_i$ and $\mathbf{v}_i$ are the position and velocity of particle i, $r_{{\rm max},i}$ is the semi-major axis of the eccentric orbit that describes particle i and

$$I_{r_1, r_2} = \left[\frac{\sqrt{Ar^2 + Br + C}}{A} + \frac{B}{2A\sqrt{-A}} \arcsin\left(\frac{2Ar + B}{\sqrt{-D}} \right) \right]_{r_1}^{r_2}, \tag{4.16}$$

where $A = 2E_i/m_i$, $B = 2GM$ and $C = -J_i^2/m_i^2$. Then, it is assumed that the kinetic energy of these particles is dissipated within the radius of the disk. Thus, the released fallback energy, $E_{\rm fb}$, is the difference between the potential plus kinetic energy at the initial radius, r_i, and the potential energy at the dissipation radius, $R_{\rm dis}$. The accretion luminosities is therefore $L = dE_{\rm fb}/dt$.

4.3 Results

In this section we present the possible observational consequences of the interactions. The section is organized as follows. We first describe the resulting gravitational waveforms in section 4.3.1. We do so for the three possible outcomes of the interactions. It

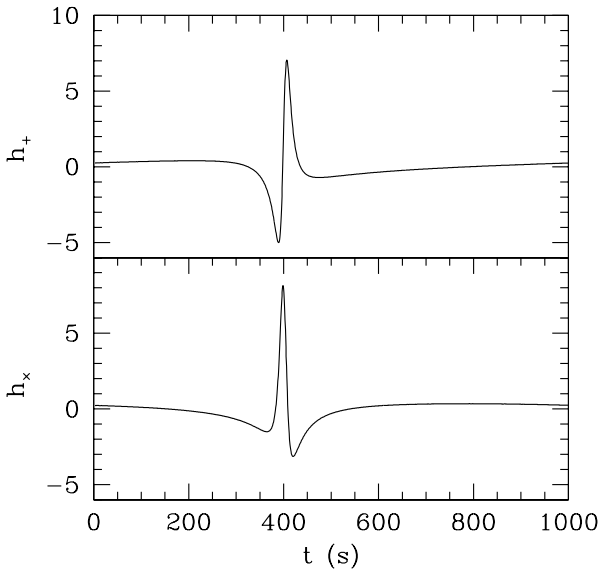

Figure 4.1: Gravitational waveforms for a close encounter in which an eccentric binary is formed. For this particular case both white dwarfs have equal masses, $M = 0.8\,M_{\odot}$, whilst the adopted initial conditions are $v_{\rm ini} = 200$ km s^{-1} and $\Delta y = 0.4\,R_{\odot}$. We only show the waveforms h_{+} (top panel) and $h_{\times}$ (bottom panel) for an inclination $i = 0^{\circ}$ and a distance of 10 kpc, in units of 10^{-22}. See text for details.

follows section 4.3.2 where we present the light curves for those interactions in which a detonation, with the subsequent disruption of one of the stars, occurs, whereas in section 4.3.3 we discuss the neutrino emission of all the direct collisions. Finally, in section 4.3.4 we describe the fallback X-ray luminosities for those interactions in which a debris region around a central white dwarf is formed.

4.3.1 Gravitational wave radiation

Eccentric orbits

In chapter 3 we have characterized the initial conditions of the encounters in terms of the initial relative velocity ($v_{\rm ini}$) and the initial distance perpendicular to the relative velocity (Δy) at a sufficiently large distance so that the two interacting white dwarfs are not affected by tidal forces. Here we will compute the gravitational waveforms of the interactions computed using this notation as well.

As previously explained, some of the close encounters computed result in the formation of a binary system that survives the interaction and no mass transfer between the two stars occurs. In these cases the eccentricity of the orbit is always large, $e > 0.5$. Figure 4.1 shows the resulting gravitational dimensionless strains

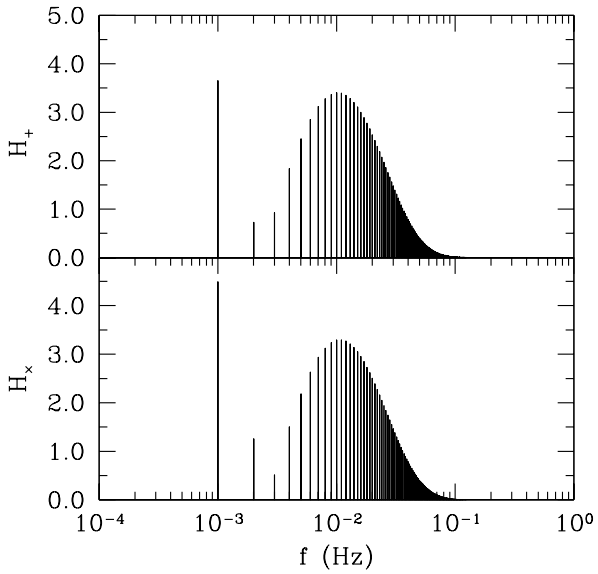

Figure 4.2: Fourier transforms of the gravitational waveforms of Fig. 4.1, in units of 10^{-23}.

of a typical case, in units of 10^{-22}, for an edge-on orbit. The two polarizations of the gravitational radiation, h_+ and $h_\times$, are shown, respectively, in the top and bottom panels, for a full period of the orbit. The corresponding dimensionless Fourier transforms, $H(f) = \tilde{h}/T$ where $T = 1$ yr, of these gravitational wave patterns are displayed in Fig. 4.2. As can be seen, the gravitational wave emission presents a single, narrow, large pulse, which occurs at the periastron, whereas the corresponding Fourier transforms, H_+ and $H_\times$, present a peak at the orbital frequency, and several Fourier components at larger frequencies. This was expected, as a binary system in a circular orbit produces a monochromatic gravitational waveform at twice the orbital frequency, while for eccentric orbits it is found — see, for instance, Wahlquist (1987) — that the binary system radiates power at the fundamental mode and at several harmonics of the orbital frequency. The reason for this is clear, since it is at closest approach when the accelerations are larger, thus resulting in an enhanced emission of gravitational radiation. Moreover, it turns out that for a fixed energy, the larger the eccentricity, the smaller the distance at closest approach, and therefore the larger the radiated power.

Table 4.1 lists for each of the runs of chapter 3 which result in the formation of an eccentric binary system the masses of the interacting white dwarfs, the eccentricity of the orbit, the frequency of the fundamental mode, and the signal-to-noise ratios for h_+ for the eLISA mission, adopting $i = 0°$ and a distance of 10 kpc. Also listed, for the sake of completeness, is the run number (first column). As can be seen, eLISA will be able to detect almost all these systems with sufficiently large SNRs.

Table 4.1: Signal-to-noise ratios of the gravitational waves of the interactions resulting in eccentric orbits, for the case of eLISA, adopting $i = 0°$ and a distance of 10 kpc.

Run	$M_1 + M_2$ ($M_\odot$)	e	f (Hz)	SNR
$v_{\rm ini} = 150$ km/s		$\Delta y = 0.4\ R_\odot$		
55	0.2+0.4	0.736	5.54×10^{-4}	1.90
56	0.4+0.4	0.799	6.91×10^{-4}	5.25
$v_{\rm ini} = 200$ km/s		$\Delta y = 0.3\ R_\odot$		
59	0.2+0.4	0.695	6.64×10^{-4}	2.00
60	0.4+0.4	0.762	8.64×10^{-4}	5.87
$v_{\rm ini} = 200$ km/s		$\Delta y = 0.4\ R_\odot$		
25	0.8+0.6	0.796	9.11×10^{-4}	16.41
26	0.8+0.8	0.820	1.00×10^{-3}	23.42
27	1.0+0.8	0.840	1.09×10^{-3}	30.48
28	1.2+0.8	0.855	1.16×10^{-3}	37.38
63	0.2+0.4	0.564	4.25×10^{-4}	0.48
64	0.4+0.4	0.657	5.74×10^{-4}	2.49
65	0.8+0.4	0.764	8.12×10^{-4}	9.70
$v_{\rm ini} = 300$ km/s		$\Delta y = 0.3\ R_\odot$		
29	0.8+0.6	0.705	1.03×10^{-3}	15.11
30	0.8+0.8	0.736	1.17×10^{-3}	22.90
31	1.0+0.8	0.762	1.30×10^{-3}	31.08
32	1.2+0.8	0.783	1.41×10^{-3}	39.33
67	0.4+0.4	0.571	5.21×10^{-4}	1.38
68	0.8+0.4	0.666	8.82×10^{-4}	8.11
69	1.2+0.4	0.737	1.17×10^{-3}	17.22
$v_{\rm ini} = 300$ km/s		$\Delta y = 0.4\ R_\odot$		
33	0.8+0.6	0.576	6.64×10^{-4}	6.04
34	0.8+0.8	0.620	7.67×10^{-4}	10.71
35	1.0+0.8	0.657	8.62×10^{-4}	16.90
36	1.2+0.8	0.688	9.49×10^{-4}	23.77
70	0.8+0.4	0.525	5.51×10^{-4}	2.99
71	1.2+0.4	0.621	7.67×10^{-4}	8.05

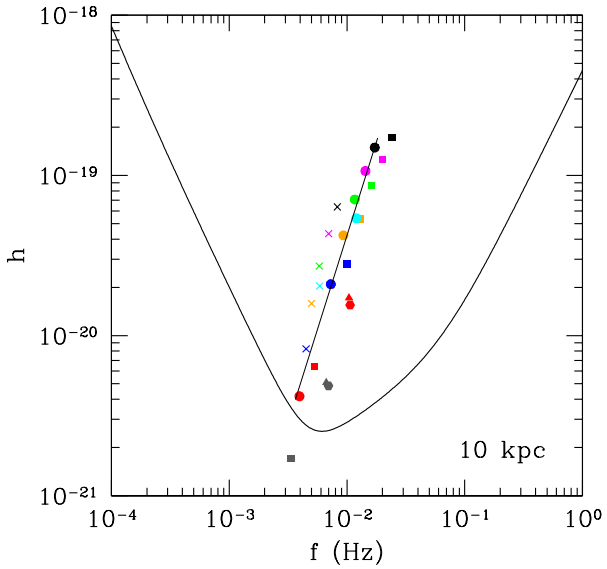

Figure 4.3: A comparison of the signal produced by the close white dwarf binary systems studied here, when a distance of 10 kpc is adopted, with the spectral distribution of noise of eLISA for a one year integration period, and for a null inclination. We assess the detectability of the h_+ dimensionless strain. The different colors denote different masses of the interacting white dwarfs, whereas the different symbols are used to distinguish between different initial conditions. Specifically, black symbols correspond to a $1.2\,M_\odot + 0.8\,M_\odot$ binary system, magenta ones to a $1.0\,M_\odot + 0.8\,M_\odot$, green symbols to a $0.8\,M_\odot + 0.8\,M_\odot$, cyan ones to a $1.2\,M_\odot + 0.4\,M_\odot$, orange symbols to a $0.8\,M_\odot + 0.6\,M_\odot$, blue ones to a $0.8\,M_\odot + 0.4\,M_\odot$, red symbols to a $0.4\,M_\odot + 0.4\,M_\odot$, and grey ones are used for a $0.4\,M_\odot + 0.2\,M_\odot$ binary system. On the other hand, hexagons are used for the case in which $v_{\rm ini} = 150$ km/s and $\Delta y = 0.4\,R_\odot$, triangles for $v_{\rm ini} = 200$ km/s and $\Delta y = 0.3\,R_\odot$, squares for $v_{\rm ini} = 200$ km/s and $\Delta y = 0.4\,R_\odot$, circles for $v_{\rm ini} = 300$ km/s and $\Delta y = 0.3\,R_\odot$, crosses for $v_{\rm ini} = 300$ km/s and $\Delta y = 0.4\,R_\odot$.

Only run number 63, which corresponds to the binary system with an orbit with the smallest eccentricity ($e = 0.564$) and for which the two interacting white dwarfs have the smallest masses — namely, $M_1 = 0.4\,M_\odot$ and $M_2 = 0.2\,M_\odot$ — will not be detectable. The rest of the interactions have, in general, large SNRs.

In Fig. 4.3 we display the characteristic amplitudes and frequencies of the h_+ dimensionless strain for $i = 0^\circ$ and we compare them with the sensitivity curve of eLISA, computed using the analytical approximation of Amaro-Seoane et al. (2013). As previously noted, only run number 63 lies below the eLISA sensitivity limit. Moreover, in this figure it can be clearly seen that for a fixed initial condition — that is for a fixed pair of values of $v_{\rm ini}$ and Δy — the characteristic amplitude as well as the frequency decreases with the total mass. The mass ratio of the interacting

white dwarfs, $q = M_2/M_1$, also plays a role. This can be seen when simulations 30 and 69, or 34 and 71, are compared. Both pairs of simulations have the same initial conditions and total mass, but different values of q. As can be seen, the value of the characteristic amplitude in runs 69 and 71 — which have $q = 1/3$ — is smaller, while the characteristic frequencies are larger than those of runs 30 and 34, respectively — which have $q = 1$. Finally, it is interesting to realize that for a given set of initial conditions the runs of different masses lie approximately on straight lines, which are not all shown for the sake of clarity. In particular, we only show, using a thin solid line, the case in which the initial conditions are $v_{\rm ini} = 300$ km/s and $\Delta y = 0.3\,R_\odot$.

Lateral collisions

In lateral collisions the less massive white dwarf is tidally deformed by the more massive star at closest approach to such an extent that in the end some of its material is accreted by the massive companion. This occurs in several mass tranfer episodes, and the resulting final configuration consists of a central compact object surrounded by a hot, rapidly rotating corona, and an external region where some of the debris produced during the dynamical interaction can be found. A typical example of the gravitational wave pattern resulting in these cases is shown in Fig. 4.4, which corresponds to run number 21. This specific simulation corresponds to the dynamical interaction of two white dwarfs with masses $0.8\,M_\odot$ and $0.6\,M_\odot$, whereas the adopted initial conditions were $v_{\rm ini} = 200$ km s^{-1} and $\Delta y = 0.3\,R_\odot$. Again, in this figure we only show the waveforms h_+ (top panel) and $h_\times$ (bottom panel) for an inclination $i = 0^\circ$ and a distance of 10 kpc, in units of 10^{-22}. As can be seen, the time evolution of the dimensionless strains presents a series of peaks. For this specific case each one of these peaks corresponds to a mass transfer episode, which occurs short after the passage through the periastron. Nevertheless, it is to be noted that, depending on the masses of the stars and on the initial conditions of the close encounter, the eccentricity of the orbit and the distance at closest approach may be quite different for the several lateral collisions studied here. Hence, the number of periastron passages shows a wide range of variation. However, a general feature in all cases is that the emission of gravitational waves is largest for the first passages through the periastron and the amplitude of the narrow peaks of gravitational wave radiation decreases in subsequent passages. Note as well that the time difference between successive peaks of the gravitational wave pattern also decreases as time passes by. All this is a consequence of the fact that after every passage through the periastron the orbit is slightly modified, either because the less massive white dwarf is substantially deformed by tidal forces in those cases in which during the first passages through the periastron there is no mass transfer from the less massive white dwarf to the more massive one, or because mass transfer has happened, and the orbit becomes less eccentric. In the former case, after a few passages through the periastron mass transfer occurs, and the subsequent evolution is similar to that of lateral collisions in

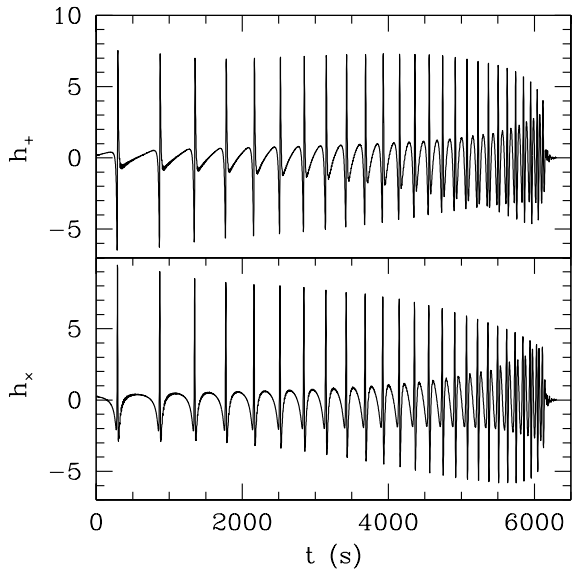

Figure 4.4: Gravitational waveforms for a close encounter in which the outcome of the interaction is a lateral collision. For this particular case two white dwarfs of masses $0.8\,M_{\odot}$ and $0.6\,M_{\odot}$, respectily, collide. The adopted initial conditions of this interaction are $v_{\rm ini} = 200$ km s^{-1} and $\Delta y = 0.3\,R_{\odot}$. As in Fig. 4.1 we only show the waveforms h_{+} (top panel) and $h_{\times}$ (bottom panel) for an inclination $i = 0^{\circ}$ and a distance of 10 kpc. Again, the units of of the dimensionless stresses are 10^{-22}.

which there is a mass transfer episode during the first closest approach. Finally, after several mass transfers, the binding energy of the less massive star becomes positive and it is totally destroyed, leading to a merger. This causes the sudden decrease of the gravitational wave emission, although some oscillations of the remnant still radiate gravitational waves — in a way very much similar to that of the ring-down phase found in mergers of two compact objects — but with a significantly smaller amplitude than the previous ones.

The dimensionless Fourier transform of the gravitational wave pattern shown in Fig. 4.4 is displayed in Fig. 4.5. The only difference with those Fourier transforms shown in Fig. 4.2 is that in this case to compute the dimensionless Fourier transform we adopt the duration of the merger. In contrast with the Fourier transform of the gravitational wave emission presented in Fig. 4.2, which is discrete because the signal is periodic, now the emission of gravitational waves is characterized by a continuous spectrum, and presents two peaks. The first one is a broad, smooth peak at around $f = 3$ mHz, while the second one, which is of larger amplitude but more noisy, occurs at larger frequencies, ~ 20 mHz. Since in our numerical configuration all the lateral collisions have orbits which can be well approximated

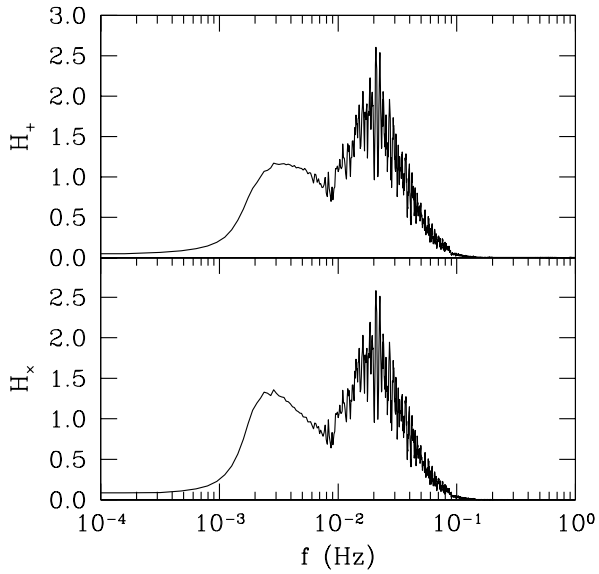

Figure 4.5: Fourier transforms of the gravitational waveforms of Fig. 4.4, in units of 10^{-23}.

until the passage through the periastron by elliptical ones, the first of these peaks corresponds to the fundamental mode of the eccentric orbit, while the second one is due to the presence of higher order harmonics, as it occurs for the pure elliptical orbits previously analyzed, being the most significant difference the continuous shift in frequency due to orbit circularization, which noticeably broadens the fundamental mode.

In Fig. 4.6 we compare the amplitude of the simulated waveform of run number 20 (a typical lateral collision) as a function of the frequency to the strain sensitivity of two detectors, eLISA and ALIA. As can be seen, eLISA will not be able to detect this dynamical interaction at a distance of 10 kpc. However, ALIA (Crowder & Cornish, 2005) — a proposed space-borne gravitational-wave detector — would eventually be able to detect most of these gravitational signals. This is quantified in Table 4.2, where we list for each simulation, the masses of the interacting white dwarfs, the number of mass transfer episodes (N), the mass of nickel synthesized (if the mass of ^{56}Ni is zero means that the interaction failed to produce a detonation, or that the detonation conditions were reached in very small region of the shocked material, for very short periods of time), the energy radiated in the form of gravitational waves, and the energy carried away by thermal neutrinos. Finally, in the last two columns we list the SNR of h_+ for the same conditions used previously. In general, for a fixed white dwarf pair, the less eccentric orbits with larger periastron distances the larger the number of mass transfer episodes, and the smaller the maximum amplitude of the gravitational wave signal. This is an expected result, as a less violent merger

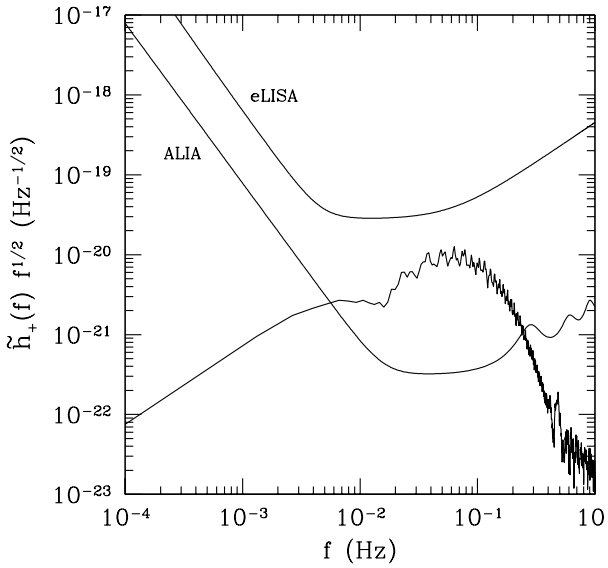

Figure 4.6: Fourier spectra of the gravitational waveform of a typical lateral collision — run number 20, which involves two white dwarfs of masses $0.8\,M_\odot$ and $1.2\,M_\odot$, respectively — in units that facilitate the comparison with gravitational-wave detector noise curves. The noise spectra of eLISA and ALIA are also shown for comparison.

episode lasting for longer times results in smaller accelerations. Nevertheless, none of the lateral collisions studied here has chances to be detected by eLISA, given that the respective SNRs are always relatively small, a quite unfortunate situation. More sophisticated and sensitive detectors — like ALIA, for instance — would, however, be able to detect such events.

Table 4.2 deserves further comments. In particular, it is worth mentioning that the total energy released in the form of gravitational waves increases as the total mass of the white dwarf pair increases, as it should be expected. More interestingly, the mass ratio of the colliding white dwarfs, $q = M_2/M_1$ also plays a role. Specifically, we find that for a fixed total mass, the smaller the value of q, the smaller the strength of the gravitational signals. Additionally, since the total energy radiated as gravitational waves not only depends on the masses of the colliding white dwarfs, but also on the duration of the dynamical interaction, we find that, for fixed initial conditions, lateral collisions in which the total mass of the system is large can release small amounts of energy in the form of gravitational waves, depending on the number of mass transfer episodes. Actually, two of the cases for which the SNR is largest — simulations number 21 and 22, which involve a $M_1 = 0.6\,M_\odot$ and a $M_2 = 0.8 M_\odot$ and two $0.8, M_\odot$ white dwarfs — clearly correspond to those interactions which have longest durations, and more mass transfer episodes, and nevertheless the masses of

Table 4.2: Properties of lateral collisions.

Run	$M_1 + M_2$ ($M_\odot$)	N	$M_{\rm Ni}$ ($M_\odot$)	$E_{\rm GW}$ (erg)	E_ν	SNR eLISA	SNR ALIA
$v_{\rm ini} = 75$ km/s		$\Delta y = 0.4\ R_\odot$					
39	0.4+0.2	2	0	2.78×10^{38}	3.03×10^{42}	0.02	1.60
$v_{\rm ini} = 100$ km/s		$\Delta y = 0.3\ R_\odot$					
43	0.4+0.2	2	4.97×10^{-14}	2.69×10^{38}	3.23×10^{42}	0.02	1.61
$v_{\rm ini} = 100$ km/s		$\Delta y = 0.4\ R_\odot$					
9	0.6+0.8	2	0	1.32×10^{41}	3.64×10^{43}	0.11	12.24
10	0.8+0.8	2	4.52×10^{-10}	6.37×10^{41}	2.25×10^{44}	0.15	18.03
11	1.0+0.8	2	7.94×10^{-7}	1.16×10^{42}	1.28×10^{45}	0.16	18.74
12	1.2+0.8	2	1.09×10^{-5}	2.10×10^{42}	2.43×10^{45}	0.16	18.73
47	0.4+0.2	2	0	1.87×10^{38}	3.58×10^{35}	0.02	1.58
48	0.4+0.4	2	2.76×10^{-11}	4.36×10^{39}	3.24×10^{43}	0.07	5.66
$v_{\rm ini} = 150$ km/s		$\Delta y = 0.3\ R_\odot$					
13	0.6+0.8	2	0	1.18×10^{41}	1.82×10^{41}	0.13	13.47
14	0.8+0.8	2	0	4.45×10^{41}	4.36×10^{43}	0.17	19.38
15	1.0+0.8	2	1.56×10^{-13}	8.58×10^{41}	8.82×10^{43}	0.17	20.16
16	1.2+0.8	2	9.70×10^{-10}	1.32×10^{42}	6.12×10^{44}	0.14	15.75
51	0.4+0.2	2	0	1.15×10^{38}	1.70×10^{35}	0.03	1.38
52	0.4+0.4	2	0	4.04×10^{39}	1.16×10^{43}	0.07	6.33
$v_{\rm ini} = 150$ km/s		$\Delta y = 0.4\ R_\odot$					
17	0.6+0.8	6	0	8.77×10^{40}	2.97×10^{39}	0.28	24.25
18	0.8+0.8	4	0	4.57×10^{41}	3.74×10^{42}	0.29	31.33
19	1.0+0.8	5	0	5.61×10^{41}	1.56×10^{41}	0.36	36.83
20	1.2+0.8	3	0	6.26×10^{41}	2.44×10^{43}	0.31	32.34
57	0.8+0.4	3	6.98×10^{-14}	7.01×10^{39}	1.83×10^{42}	0.12	8.56
58	1.2+0.4	2	5.61×10^{-10}	2.55×10^{40}	1.63×10^{43}	0.11	9.70
$v_{\rm ini} = 200$ km/s		$\Delta y = 0.3\ R_\odot$					
21	0.6+0.8	27	0	2.17×10^{41}	9.45×10^{39}	0.57	45.83
22	0.8+0.8	20	0	1.07×10^{42}	6.60×10^{39}	0.64	63.28
23	1.0+0.8	5	0	5.69×10^{41}	2.46×10^{41}	0.37	37.69
24	1.2+0.8	3	0	5.82×10^{41}	3.84×10^{44}	0.31	32.10
61	0.8+0.4	3	0	7.03×10^{39}	3.85×10^{41}	0.12	8.70
62	1.2+0.4	2	3.27×10^{-9}	2.03×10^{40}	2.36×10^{43}	0.11	9.67
$v_{\rm ini} = 200$ km/s		$\Delta y = 0.4\ R_\odot$					
66	1.2+0.4	8	7.30×10^{-12}	2.46×10^{40}	5.89×10^{42}	0.25	15.50

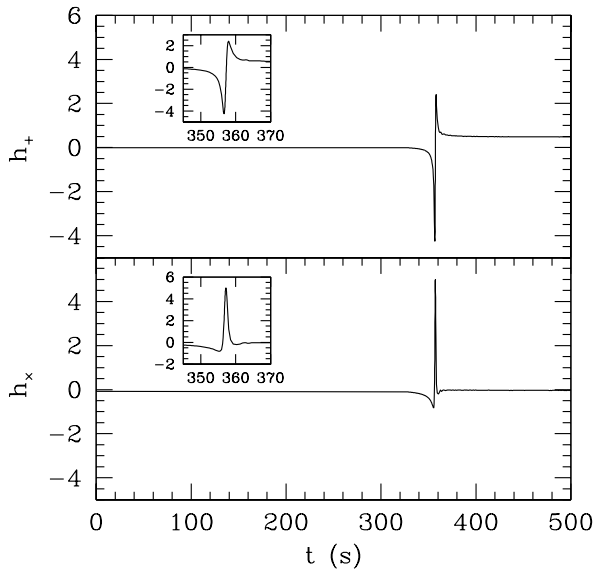

Figure 4.7: Gravitational waveform for a typical direct collision, in units of 10^{-21}. The inset shows in greater detail the region of the burst of gravitational waves.

the interacting white dwarfs are not excesively large. Note, however, that in run number 20 the gravitational energy released is larger than in simulation 21, but the SNR is smaller. This occurs because run 21 peaks at frequencies where eLISA and ALIA will be most sensitive.

Direct collisions

As explained before, the last outcome of the dynamical interactions studied here consists in a direct collision, in which a single mass transfer episode, of very short duration, occurs. The physical conditions achieved in all these interactions are such that the densities and temperatures necessary to produce a powerful detonation are met, leading in nearly all the cases to the disruption of either the lightest white dwarf or of both stars — see column 3 of Table 4.3, where we list whether none (0), one (1), or both (2) colliding white dwarfs are disrupted — and a sizable amount of mass is ejected as a consequence of the interaction. Although it will not be possible to detect the gravitational signal produced in these interactions, owing to their extremely short duration, for the sake of completeness in Fig. 4.7 a typical example of the gravitational wave pattern is displayed. The signal is characterized by a single, very narrow pulse. Finally, the total energy radiated as gravitational waves can be found in Table 4.3. As can be seen, in general, the larger the total mass of the system, the larger the emission of gravitational waves. As it occurs with

Table 4.3: Properties of direct collisions.

Run	$M_1 + M_2$ ($M_\odot$)	Disruption	$M_{\rm Ni}$ ($M_\odot$)	$E_{\rm GW}$ (erg)	E_ν	$\frac{\Delta m}{\Delta t}$ (mag/day)
$v_{\rm ini} = 75$ km/s		$\Delta y = 0.3\ R_\odot$				
37	0.4+0.2	1	1.31×10^{-9}	9.51×10^{37}	3.21×10^{43}	0.019
38	0.4+0.4	2	8.84×10^{-4}	1.49×10^{41}	7.01×10^{45}	0.016
$v_{\rm ini} = 75$ km/s		$\Delta y = 0.4\ R_\odot$				
1	0.8+0.6	0	8.65×10^{-8}	1.72×10^{41}	1.20×10^{45}	—
2	0.8+0.8	0	4.47×10^{-3}	5.12×10^{41}	7.21×10^{45}	—
3	1.0+0.8	2	7.25×10^{-1}	8.46×10^{41}	8.42×10^{47}	0.020
4	1.2+0.8	1	6.60×10^{-2}	2.71×10^{42}	3.04×10^{46}	0.019
40	0.4+0.4	2	1.64×10^{-3}	6.38×10^{40}	6.43×10^{45}	0.010
41	0.8+0.4	1	8.04×10^{-4}	5.37×10^{39}	3.66×10^{45}	0.013
42	1.2+0.4	1	1.18×10^{-3}	3.47×10^{40}	4.49×10^{45}	0.022
$v_{\rm ini} = 100$ km/s		$\Delta y = 0.3\ R_\odot$				
5	0.8+0.6	0	2.74×10^{-8}	1.70×10^{41}	1.03×10^{45}	—
6	0.8+0.8	0	3.67×10^{-3}	5.35×10^{41}	6.64×10^{45}	—
7	1.0+0.8	2	7.15×10^{-1}	9.08×10^{41}	8.36×10^{47}	0.017
8	1.2+0.8	1	6.32×10^{-2}	2.62×10^{42}	3.18×10^{46}	0.013
44	0.4+0.4	2	4.68×10^{-3}	9.33×10^{40}	6.94×10^{45}	0.020
45	0.8+0.4	1	7.60×10^{-4}	5.73×10^{39}	3.66×10^{45}	0.015
46	1.2+0.4	1	2.21×10^{-3}	3.39×10^{40}	4.95×10^{45}	0.015
$v_{\rm ini} = 100$ km/s		$\Delta y = 0.4\ R_\odot$				
49	0.8+0.4	1	5.00×10^{-4}	9.54×10^{39}	3.02×10^{45}	0.017
50	1.2+0.4	1	9.36×10^{-4}	4.52×10^{40}	3.67×10^{45}	0.019
$v_{\rm ini} = 150$ km/s		$\Delta y = 0.3\ R_\odot$				
53	0.8+0.4	1	2.00×10^{-4}	1.51×10^{40}	2.47×10^{45}	0.015
54	1.2+0.4	1	8.44×10^{-4}	5.11×10^{40}	3.39×10^{45}	0.018

lateral collisions, the mass ratio of the colliding white dwarfs also plays a role, and white dwarf pairs with smaller values of q release smaller amounts of gravitational waves for the same value of $M_1 + M_2$.

4.3.2 Light curves

As some of the white dwarf dynamical interactions analyzed here result in powerful explosions, the light curves powered by the decay of radioactive ^{56}Ni synthesized in the most violent phases of the interaction — when the material is shocked and the temperatures and densities are such that a detonation is able to develop — might be eventually detectable. As extensively discussed before, explosions are more likely to

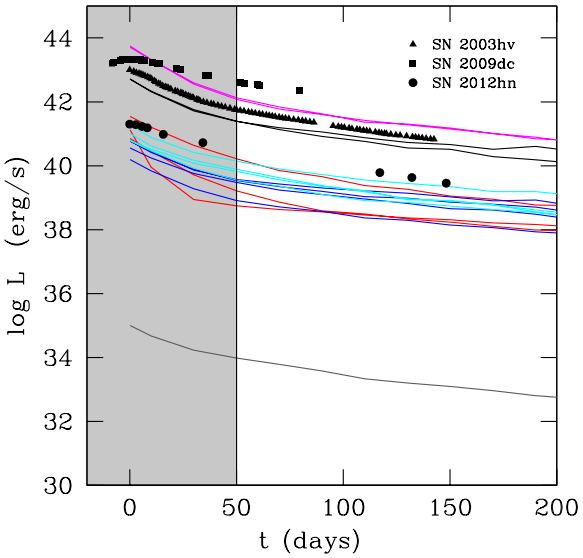

Figure 4.8: Bolometric late-time light curves of those dynamical interactions in which at least one of the colliding white dwarfs explodes. The colors indicate the different white dwarf pairs considered here, and is the same employed in Fig. 4.3: red curves stand for a $0.4\,M_{\odot}+0.4\,M_{\odot}$ system, black ones for a $0.8\,M_{\odot}+1.2\,M_{\odot}$, magenta curves denote a $0.8\,M_{\odot}+1.0\,M_{\odot}$ pair, blue ones correspond to $0.4\,M_{\odot}+0.8\,M_{\odot}$ systems, cyan lines are used for a $0.4\,M_{\odot}+1.2\,M_{\odot}$ pair, while the grey curve corresponds to the $0.2\,M_{\odot}+0.4\,M_{\odot}$ case. The light curves of three observed Type Ia supernovae are also displayed for comparison. Square symbols show the light curve of SN 2009dc, triangles correspond to SN 2003hv, while circles correspond to SN 2012hn. The gray shaded area indicates that for these early times our light curve is not entirely reliable. The time origin is set at the time at which our simulations reach the maximum temperature (explosion time).

occur in direct collisions, although in some lateral collisions some nickel is also synthesized. However, the masses of synthesized nickel in lateral collisions are in general small, and consequently we expect that most of these events would be undetectable — see Tables 4.2 and 4.3. In particular the amount of ^{56}Ni produced in lateral collisions is almost negligible in most cases — ranging from about $\sim 5\times10^{-14}\,M_{\odot}$ to about $1\times10^{-5}\,M_{\odot}$. On the other hand, the resulting masses of nickel in direct collisions, although show a broad range of variation, are consistently larger than in lateral collisions. According to this, the late-time light curves are characterized by large variations. This is shown in Fig. 4.8, where the late-time light curves — computed according to the procedure outlined in section 4.2.2 — of those direct collisions in which at least one of the colliding white dwarfs is disrupted are displayed.

Figure 4.8 shows that the late-time light curves are sensitive not only to the total mass of the pair of colliding white dwarfs, but also to the choice of initial conditions.

Specifically, the bolometric late-time light curves can differ considerably for a fixed pair of masses, depending on the initial conditions of the considered interaction. The most extreme case is that of a $0.4\,M_{\odot} + 0.4\,M_{\odot}$ (red lines in Fig. 4.8). In particular, for this specific case the late-time bolometric luminosities differ by about 1 order of magnitude when runs number 38, 40 and 44 are considered. This stems from the very large difference in the nickel masses synthesized in the respective interactions, which are $8.84 \times 10^{-4}\,M_{\odot}$, $1.64 \times 10^{-3}\,M_{\odot}$, and $4.68 \times 10^{-3}\,M_{\odot}$, respectively. The different velocities of the ejecta also play a role. The most powerful outburst corresponds to the case in which a $0.8\,M_{\odot} + 1.0\,M_{\odot}$ pair of white dwarfs experience a direct collision — magenta lines in Fig. 4.8. This agrees well with the results obtained so far for white dwarf mergers, in which case the most powerful events are found when both white dwarfs have similar masses and are relatively massive (Pakmor et al., 2012). Also of interest is to realize that we obtain a mild explosion in the case in which a $0.2\,M_{\odot} + 0.4\,M_{\odot}$ white dwarf system in which both stars have helium cores collide (run number 37). In this specific case the nickel mass is small ($1.39 \times 10^{-9}\,M_{\odot}$), and only one of the stars — the lightest one — is disrupted. Most importantly, its late-time light curve falls well below the bulk of light curves computed here (the peak luminosity is nearly 9 orders of magnitude smaller).

In Fig. 4.8 we also display the bolometric light curves of three thermonuclear supernovae, for which late-time observations are available, to allow a meaningful comparison with the synthetic late-time light curves computed here. Squares correspond to the light curve of SN 2009dc, which was an overluminous peculiar supernova (Yamanaka et al., 2009), triangles correspond to the light curve of the otherwise normal thermonuclear supernova SN 2003hv (Leloudas et al., 2009), while circles correspond to the underluminous Type Ia supernova SN 2012hn (Valenti et al., 2014). As can be seen, only a few of our simulated late-time light curves — corresponding to the brightest events — have characteristics similar to those of thermonuclear supernovae, whereas most of the dynamical interactions studied in this work would appear as underluminous transients. In particular, only the runs in which rather massive white dwarfs interact have light curves which could be assimilated to those of Type Ia supernovae. In particular, this is the case of runs number 4 and 8, in which a pair of white dwarfs with masses $0.8\,M_{\odot}$ and $1.2\,M_{\odot}$ interact — in which case only the less massive carbon-oxygen white dwarf is disrupted, while the massive ONe one remains bound — for runs 3 and 7 — which involve a pair of massive carbon-oxygen white dwarfs of masses $0.8\,M_{\odot}$ and $1.0\,M_{\odot}$, and both components are distroyed as a consequence of the interaction — and, possibly, runs number 38 and 42, which involve two white dwarfs with masses $0.4\,M_{\odot}$ and $0.4\,M_{\odot}$, and $1.2\,M_{\odot}$ and $0.4\,M_{\odot}$, respectively. Note that in these last two cases a white dwarf with a helium core is involved. Hence, the total mass burned is small, as is the mass of synthesized ^{56}Ni — see table 4.3. In summary, only those light curves resulting from events in which the total mass of the system is large (larger than $\sim 1.8\,M_{\odot}$) and a carbon-oxygen white dwarf is involved in the interaction resemble those of thermonuclear supernovae, whereas the

rest of the interactions are transient bright events of different nature.

In Table 4.3 we also show the decline rate of the bolometric light curve at late times. As well known, after about 50 days the light curves of Type Ia supernovae steadily decline in an exponential way. It is observationally found that the decline rates are essentially the same for all thermonuclear supernovae between 50 and 120 days (Wells et al., 1994; Hamuy et al., 1996; Lira et al., 1998) — that is, for the time interval for which the results of our calculations are reliable — and hence, a comparison of our calculations and the observed decline rates is worthwhile. The typical values of the late-time decline rate are 0.014 mag/day in the B band, 0.028 mag/day in the V band, and 0.042 mag/day in the I band, although there are a few exceptions (SN 1986G and SN 1991bg), which decline faster — see Leibundgut (2000), and references therein. Given our numerical approach, to compare our simulated late-time light curves with the observed decline rates of supernovae Ia we only used data from day 60. As shown in Table 4.3 the computed decline rates are compatible with those observationally found in Type Ia supernovae.

4.3.3 Thermal neutrinos

As mentioned, due to the extreme physical conditions reached in some of the interactions studied in this work it is expected that copious amounts of thermal neutrinos should be produced in those regions where the material of the colliding white dwarfs is compressed and heated. Tables 4.2 and 4.3 show that this is indeed the case. In particular, in these tables we list the energy radiated in the form of thermal neutrinos in lateral collisions and in direct ones, respectively. As can be seen, the radiated energies are in all cases rather large, although a large spread is also found. Specifically, for the case of lateral collisions the neutrino energies range from $\sim 1.7 \times 10^{35}$ erg to $\sim 2.4 \times 10^{45}$ erg, roughly 10 orders of magnitude, whereas in the case of direct collisions the range of variation is somewhat smaller, since it spans about 5 orders of magnitude, being run 3 the simulation in which more neutrinos are produced ($\sim 8.4 \times 10^{47}$ erg). In general, we find that for the case of lateral collisions increasing the total mass of the system results in stronger interactions, and consequently larger peak temperatures and densities are achieved. This directly translates in a larger release of both nuclear energy and of thermal neutrinos — see Table 4.2. Equally, for a fixed total mass of the system, larger mass ratios lead to a smaller nuclear energy release, and in a reduced neutrino emission. Besides, systems with larger initial distances at closest approach between both colliding white dwarfs result in longer mergers — as can be seen in column 3 of table 4.2, which lists the number of mass transfer episodes occurring in each lateral collision — and, therefore, in more gentle interactions, thus leading to smaller neutrino luminosities. This is in contrast with what we found for the emission of gravitational waves, for which the reverse is true. For the case of direct collisions we also find that, in general, as the total mass of the system is increased, neutrino luminosities also increase, as it happens in lateral

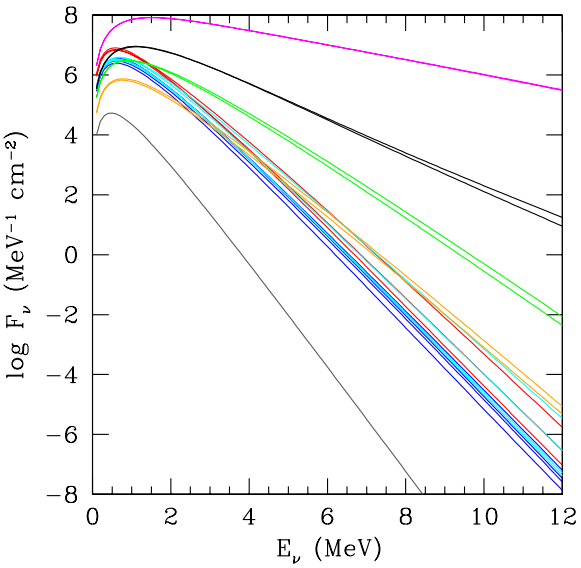

Figure 4.9: Spectral energy distribution of neutrinos for those interactions resulting in a direct collision. The color coding is the same employed in Fig. 4.3. We assumed that source of neutrinos is located at a distance of 1 kpc.

collisions — see Table 4.3. However, there are exceptions to this rule. Specifically, a good example of this is the case of the interactions in which two white dwarfs of masses $0.8\,M_\odot$ and $1.0\,M_\odot$ collide. In these interactions both stars are totally disrupted, and it turns out that, consequently, the nuclear energy released is larger, and that more neutrinos are produced than in the case in which a $0.8\,M_\odot + 1.2\,M_\odot$ is considered. This is a consequence of the fact that in this case the more massive oxygen-neon white dwarf of $1.2\,M_\odot$ is more tightly gravitationally bound, and is not disrupted during the interaction.

Figure 4.9 displays the spectral energy distribution of the neutrinos emitted when the temperature reaches its maximum value during the dynamical interaction, using the same color coding as it was done in previous figures. As expected, the general features of the neutrino spectral flux follow the same pattern previously found for the peak bolometric luminosities, and show a wide range of variation. Quite naturally, the simulations in which more ^{56}Ni is synthesized also produce more neutrinos. Nevertheless, this is not the most relevant information that can be obtained from this figure. Instead, it is important to note that in all cases the peak of emission corresponds to neutrinos with energies between 1 and 2 MeV. Thus, the best-suited detector for searching the neutrino signals produced in these dynamical events is the Super-Kamiokande detector (Nakahata et al., 1999), for which the peak sensitivity is 3 MeV, although other detectors, like the IceCube Observatory (Ahrens et al., 2002)

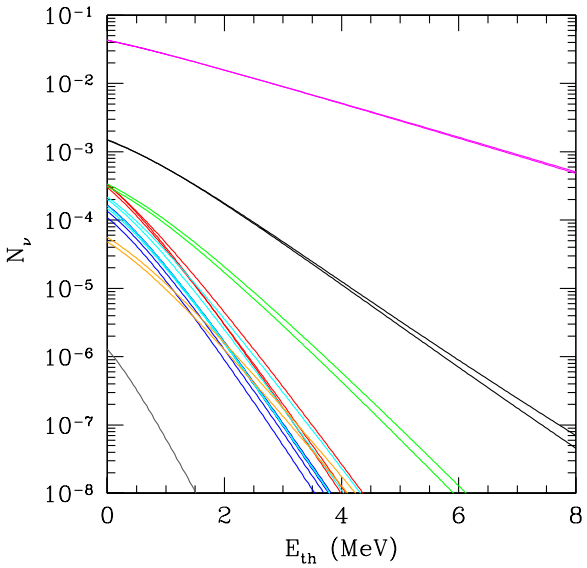

Figure 4.10: Expected number of neutrino events in the Super-Kamiokande detector, when the source is located at a distance of 1 kpc. Again, the color coding is the same employed in Fig. 4.8.

could also eventually detect the neutrinos produced in these interactions (Abbasi et al., 2011). Hence, we compute the number of expected neutrino events for this detector, using the prescription outlined in section 4.2.3. The results are shown in Fig. 4.10. Clearly, even for nearby sources (located at 1 kpc) only those dynamical interactions in which two very massive carbon-oxygen white dwarfs are involved will have (small) chances to be detected, since in the best of the cases only ~ 0.04 thermal neutrinos will interact with the tank.

4.3.4 Fallback luminosities

Another potential observational signature of the mergers studied here is the emission of high-energy photons from the fallback material in the aftermath of those dynamical interactions in which one of the stars is disrupted, and the final configuration consists of a central remnant surrounded by a debris region. As described in depth in chapter 3, in some dynamical interactions a fraction of the disrupted star goes to form a Keplerian disk. In this debris region the vast majority of material has circularized orbits. However, some material in this region has highly eccentric orbits. After some time, this material will most likely interact with the recently formed disk. Rosswog (2007) demonstrated that the relevant timescale in this case is not given by viscous dissipation but, instead, by the distribution of eccentrities. As discussed in

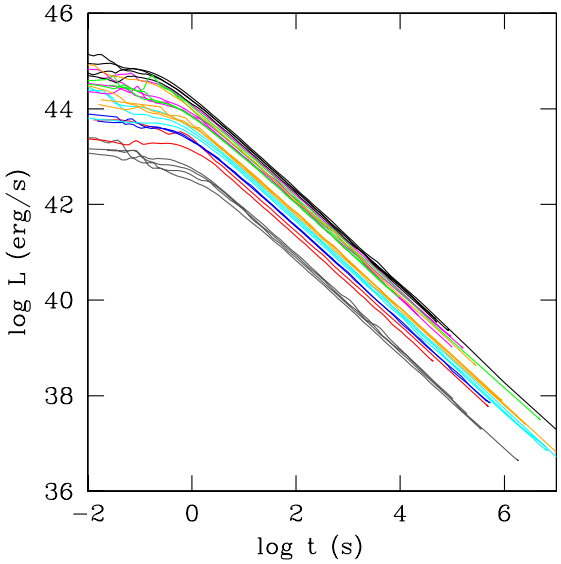

Figure 4.11: Fallback accretion luminosity for the dynamical interactions for which the outcome is a lateral collision, and hence result in the formation of a central remnant surrounded by a disk. The fallback accretion luminosities have been averaged over all the SPH particles with eccentric orbits for a given time. The color coding is the same of Fig. 4.8.

Sect. 4.2.4, we adopted the formulation of Rosswog (2007) and calculated the accretion luminosity resulting from the interaction of the material with high eccentricities with the newly formed disk by assuming that the kinetic energy of these particles is dissipated within the radius of the debris disk.

Figure 4.11 displays the results of this procedure for all the lateral collisions in which as a result of the dynamical interaction the less massive star is disrupted and a Keplerian disk is formed. We note that only a fraction of the fallback luminosity will be released in the form of high-energy photons. Thus, the results shown in this figure can be regarded as an upper limit for the actual luminosity of high-energy photons. It is important to note that the time dependence of the fallback luminosities is very similar for all the simulations, $\propto t^{-5/3}$. This time dependence is the same found for double white dwarf or double neutron star mergers. Another interesting point is that the fallback luminosities are rather high, of the order of 10^{45} erg s^{-1}, and thus these events could eventually be detected up to relatively large distances. Finally, as it should be expected, the most violent interactions result in larger fallback luminosities. In particular, the events with the largest fallback luminosities are those in which two white dwarfs with masses $0.8\,M_{\odot}$ and $1.2\,M_{\odot}$ interact (runs number 12, 16, 20 and 24, black lines), while the event in which less X-ray photons would be radiated is that in which a pair of helium white dwarfs of masses $0.2\,M_{\odot}$ and $0.4\,M_{\odot}$

collide (runs number 39, 43, 47, and 51, grey lines). Note, nevertheless, that the fallback luminosity in this case is only a factor of 10^2 smaller than that computed for the most violent event. This is in contrast with the large difference (almost 9 orders of magnitude) found for the light curves of direct collisions. This, again, is a consequence of the very small amount of ^{56}Ni synthesized during the interaction, whereas the masses of the debris region do not differ substantially (being of the same order of magnitude). A more detailed analysis shows that the key issue to explain this behavior is that the more massive mergers produce more material in the debris region with larger kinetic energies, thus resulting in enhanced fallback luminosities.

4.4 Discussion

We have computed the observational signatures of the dynamical interactions of two white dwarfs in a dense stellar environment. This includes the emission of gravitational waves for those systems which as a result of the interaction end up forming an eccentric binary system, or those pairs which experience a lateral collision, in which several mass transfer episodes occur, although we also computed the emission of gravitational waves for those events in which a direct collision, in which only one violent mass transfer episode occurs. For those cases in which as a consequence of the dynamical mass transfer process an explosion occurs, and either one or both stars are disrupted, we also computed the corresponding late-time bolometric light curves, and the associated emission of thermal neutrinos, while for all those simulations in which the less massive white dwarf is disrupted, and part of its mass goes to form a debris region, we also computed the fallback luminosities radiated in the aftermath of the interaction. This has been done employing the most complete and comprehensive set of simulations of this kind — namely that of chapter 3 — which covers a wide range of masses, chemical compositions of the cores of the white dwarfs, and initial conditions of the intervening stars. For all these signals we have assessed the feasibility of detecting them.

We have shown that in the case of interactions leading to the formation of an eccentric binary the most noticeable feature of the emitted gravitational wave pattern is a discrete spectrum, and that these signals are likely to be detected by future spaceborne detectors, like eLISA, up to relatively long distances (larger than 10 kpc). This, however, is not the case of the gravitational wave radiation resulting from lateral collisions, although more advanced experiments, like ALIA, would be able to detect them. Finally, since for the case of direct collisions the emitted signal consists of a single, well-defined peak, of very short duration, there are no hopes to detect them.

The late-time bolometric light curves of those events in which an explosion is able to develop, and at least one of the stars is disrupted, show a broad range of variation, of almost 10 orders of magnitude in luminosity. This is the logical con-

sequence of the large variety of masses of ^{56}Ni synthesized during the explosion. This, in turn, can be explained by the very different masses of the white dwarfs involved in the interaction. Even more, we have found that for a given pair of white dwarfs with fixed masses the initial conditions of the interaction — namely, the initial separations and velocities (or, alternatively, the energies and angular momenta) — also play a key role in shaping the late-time bolometric light curves, and that the corresponding peak luminosities can differ by almost 2 orders of magnitude. More interestingly, we have found that only the brightest events have light curves resembling those of thermonuclear supernovae, and that most of our simulations result in very underluminous events, which would most likely be classified as bright transient events. Only those events in which two rather massive white dwarfs (of masses larger than $\sim 0.8\,M_{\odot}$) collide would have light curves which could be assimilated to those of Type Ia supernovae. Even in this case, the resulting late-time bolometric light curves show a considerable range of variability depending on the adopted initial conditions, and light curves resembling those of underluminous, normal and peculiar bright supernovae Ia are possible.

The corresponding thermal neutrino luminosities also show a noticeable dispersion, which is a natural consequence of the very different maximum temperatures reached during the most violent phases of the interaction. Nonetheless, the chances of detecting the neutrinos emitted in these events are very low for the current detectors, even if the dynamical interaction occurs relatively close, at 1 kpc. Even in this case, the Super-Kamiokande detector would not be able to detect the neutrino signal, since the number counts are small, $\sim 10^{-2}$ in the best of the cases.

Finally, we have also computed the emission of high-energy photons in the aftermath of those interactions in which at least one of the white dwarfs is disrupted, and a debris region is formed. As it occurs for the case of the mergers of two white dwarfs, or of two neutron stars, the accretion luminosity follows a characteristic power law of index $-5/3$, but the fallback luminosities are considerably smaller than in the case of neutron star mergers. Nevertheless, the typical peak luminosities are of the order of 10^{44} erg s^{-1}, and hence should be easily detectable up to very long distances. Again, we also find that depending on the masses and the initial conditions of the interaction the spread in the peak fallback luminosities is large, although considerably smaller than that obtained for the late-time bolometric light curves.

All in all, our calculations provide a qualitative multimessenger picture of the dynamical interactions of two white dwarfs. A combined strategy in which data obtained from the planned spaceborne gravitational wave detectors, as well as optical and high-energy observations would result in valuable insight on the conditions under which this type of events take place.

Chapter 5

Double degenerate mergers as progenitors of high-field magnetic white dwarfs

High-field magnetic white dwarfs have been long suspected to be the result of stellar mergers. However, the nature of the coalescing stars and the precise mechanism that produces the magnetic field are still unknown. Here we show that the hot, convective, differentially rotating corona present in the outer layers of the remnant of the merger of two degenerate cores is able to produce magnetic fields of the required strength that do not decay for long timescales. We also show, using a state-of-the-art Monte Carlo simulator, that the expected number of high-field magnetic white dwarfs produced in this way is consistent with that found in the Solar neighborhood.

5.1 Introduction

The merger of two white dwarfs has received considerable interest during the last years because it is thought to be at the origin of several interesting astrophysical phenomena. Here we show that the merger of two degenerate cores can also explain the presence of very high magnetic fields in some white dwarfs — a result previously anticipated by Wickramasinghe & Ferrario (2000) but not yet quantitatively proved.

High-field magnetic white dwarfs have magnetic fields in excess of 10^6 G and up to 10^9 G (Schmidt et al., 2003). Surprisingly, very few belong to a non-interacting binary system (Kawka et al., 2007), and moreover they are more massive than average (Silvestri et al., 2007). One possibility is that these white dwarfs descend from single stars, so the magnetic field is a fossil of previous evolution (Angel et al., 1981). However, this scenario cannot explain why these stars are massive, and why they are not found in non-interacting binary systems. Recently, it has been suggested (Tout et al., 2008; Nordhaus et al., 2011) that strong magnetic fields are produced during a

common envelope episode in a close binary system in which one of the components is degenerate. During this phase, spiral-in of the secondary induces differential rotation in the extended convective envelope, resulting in a stellar dynamo which produces the magnetic field. However, the magnetic field produced in this way does not penetrate in the white dwarf, and decays rapidly when the common envelope is ejected (Potter & Tout, 2010).

In this chapter we show that the hot, differentially rotating, convective corona resulting from the merger of two degenerate cores produces strong magnetic fields, which are confined to the outer layers of the resulting remnant, and which do not decay for very long timescales. The chapter is organized as follows. In section 5.2 we explain the precise mechanism that produces the required magnetic fields, and we show that these fields are confined the outer layers of the remnant of the coalescence and do not decay for very long timescales. Section 5.3 is devoted to analyze if our model can account for the number of high-field magnetic white dwarfs in the Solar neighborhood, while in section 5.4 we summarize our findings and we present our conclusions.

5.2 The stellar dynamo

The merger of two degenerate cores is the final destiny of the evolution of a sizable fraction of binary systems. Three-dimensional simulations of the merger process (Guerrero et al., 2004; Yoon et al., 2007; Lorén-Aguilar et al., 2009) indicate that the remnant of the coalescence of two white dwarfs consists of a central white dwarf which contains all the mass of the primary. On top of it a hot corona, which is made of approximately half of the mass of the disrupted secondary, can be found. Finally, surrounding this compact remnant a rapidly rotating Keplerian disk is formed, containing nearly all the mass of the secondary which has not been incorporated to the hot corona. According to these calculations little mass ($\sim 10^{-3}\,M_{\odot}$) is ejected from the system during the merger. The structure of the remnant of the coalescence is illustrated in Fig. 5.1.

The existing simulations show that the temperature gradient in the hot corona is high, and consequently the corona is convective. We computed the boundaries of the convective region using the Schwarzschild criterion, $\nabla > \nabla_{\rm ad}$. We found that the inner and outer edges of the convective region are located at radii $R \approx 0.012\,R_{\odot}$, and $R \approx 0.026\,R_{\odot}$, respectively, and that the total mass inside this region is $\sim 0.24\,M_{\odot}$ (see Fig. 5.1). Moreover, this region rotates differentially, and is prone to magneto-rotational instability. Assuming energy equipartition, the resulting $\alpha\omega$ dynamo produces a magnetic field $B^2/8\pi \approx \rho(\omega R)^2/2$. For the typical values found in the simulations of Lorén-Aguilar et al. (2009), the magnetic field amounts to $B \sim 3.2 \times 10^{10}$ G. Thus, the energy available in the convective corona is sufficiently large to produce strong magnetic fields. We note that even in the case in which only

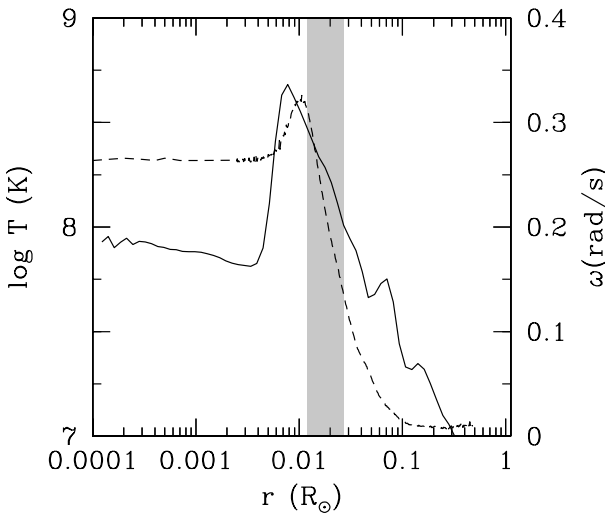

Figure 5.1: Dynamo configuration in a white dwarf merger. Temperature (solid line, left scale) and rotational velocity (dashed line, right scale) profiles of the final remnant of a white dwarf merger as a function of radius are shown for the case of a binary system composed of two stars of 0.6 and 0.8 $M_{\odot}$. In our simulations approximately half of the mass of the disrupted secondary ($\sim 0.3\,M_{\odot}$) is accreted onto the primary, while the rest of the mass goes to form the Keplerian disk, which extends up to $\sim 0.3\,R_{\odot}$. The temperature of the central white dwarf depends on the initial temperature of the coalescing white dwarfs (Yoon et al., 2007; Lorén-Aguilar et al., 2009). However, the temperature of the hot corona is remarkably similar in all the simulations, $T \approx 8.7 \times 10^8$ K. The central spinning white dwarf rotates as a rigid body with a rotational velocity $\omega \sim 0.26$ s^{-1}, and the corona rotates differentially, with a peak rotation rate $\omega \sim 0.33$ s^{-1}. These velocities arise from energy and angular momentum conservation, since little mass is ejected from the system, so the orbital angular momentum of the binary system is invested in spinning up the remnant, while the available energy is primarily invested in heating the corona. The location of the convective region is displayed by the shaded area.

0.1% of the total energy of the convective shell is invested in magnetic energy the fields produced in this way are of the order of 10^7 G, a value typical of high-field magnetic white dwarfs. We also note that there are very few white dwarfs with magnetic fields larger than 10^9 G, and that when these fields are observed, these are confined to spots on their surfaces.

For this mechanism to be efficient at producing the observed magnetic fields, the dynamo must work for several convective turnovers before the energy of the hot corona is radiated away. The temperature of the corona is so high that is preferentially cooled by neutrino emission. The neutrino luminosity of the corona is $L_{\nu} \sim 4.0 \times 10^2\,L_{\odot}$, while the total thermal energy of the non-degenerate material in the corona is $U \sim 8.8 \times 10^{48}$ erg. Hence, the convective shell lasts for $\tau_{\rm hot} \sim$

$U/L_\nu \sim 1.8 \times 10^5$ yr. The convective turnover timescale is $\tau_{\rm conv} \approx H_P/v_{\rm conv}$, where $H_P \approx 2.7 \times 10^8$ cm is the pressure scale height and $v_{\rm conv} \approx 8.0 \times 10^7$ cm/s is the convective velocity. Thus, $\tau_{\rm conv} \sim 3.3$ s, and during the lifetime of the hot corona the number of convective cycles is sufficiently large. Consequently, the $\alpha\omega$ mechanism is able to produce a strong magnetic field. We also note that if the duration of the convective shell is substantially smaller than that estimated here, large magnetic fields can still be produced. Specifically, even assuming durations 10^3 times smaller than that previously estimated, the number of convective cycles would still be enough to produce magnetic fields comparable to those observationally found in high-field magnetic white dwarfs. We thus conclude that the stellar dynamos produced in the aftermath of the merger of two degenerate cores can produce magnetic fields of the order of 10^7 G. From now on we adopt this value (typical of high-field magnetic white dwarfs) as a fiducial value for the rest of the calculations.

Once the magnetic field is established we need to know if it can diffuse outwards, to the surrounding disk, or inwards, to the degenerate primary. To this end we solved the diffusion equation (Jackson, 1998; Wendell et al., 1987):

$$\frac{\partial \vec{B}}{\partial t} = -\vec{\nabla} \times \left(\frac{c^2}{4\pi\sigma} \vec{\nabla} \times \vec{B} - \vec{v} \times \vec{B} \right) \tag{5.1}$$

being σ the magnetic conductivity, for which we used the most up-to-date prescription (Cassisi et al., 2007), while the rest of the symbols have their usual meaning. We first integrated the diffusion equation for the surrounding disk using cylindrical coordinates, adopting the velocity field and density and temperature profiles resulting from our SPH simulations (Lorén-Aguilar et al., 2009). The initial condition adopted here is $\vec{B}(0) = \vec{0}$, while we also imposed the boundary condition $\partial\vec{B}/\partial t = 0$ at the outer edge of the disk. We used a Crank-Nicolson integration scheme with variable coefficients (Dautray & L., 2000) which turns out to be stable. We found that the timescale for diffusion of the magnetic field across the disk is $\tau_{\rm disk} \sim 2.0 \times 10^{11}$ yr. We did the same calculation, this time using spherical coordinates, to estimate the penetration of the magnetic field in the dense, degenerate primary. The use of spherical coordinates is perfectly justified because the departures of the compact primary from sphericity are very small. For this calculation we followed the procedure outlined in Wendell et al. (1987). In this case the electrical conductivity is totally dominated by degenerate electrons, and depends on the adopted temperature of the isothermal white dwarf. If a temperature $T \approx 7.6 \times 10^7$ K is taken (Lorén-Aguilar et al., 2009) the diffusion timescale turns out to be $\tau_{\rm WD} \sim 4.3 \times 10^9$ yr. Since this timescale depends on the adopted initial temperature we computed, using an up-to-date stellar evolutionary code (Renedo et al., 2010), a cooling sequence for a white dwarf of the mass, $1.1\,M_\odot$, and chemical composition of the remnant, a carbon-oxygen core. The time to cool from 7.6×10^7 K to a value typical of field white dwarfs (say 3.0×10^6 K) is very short, $\tau_{\rm cool} \sim 3.0 \times 10^7$ yr. Hence, we can safely assume that as the white

dwarf cools, the rapid increase of the electrical conductivity does not allow the magnetic field to penetrate in the degenerate core of the primary, and remains confined to the surface layers.

Our model naturally predicts that the masses of high-field magnetic white dwarfs should be larger than average and that they should be observed as single white dwarfs, as observationally found — see, for instance, Valyavin & Fabrika (1999). However, high-field magnetic white dwarfs are generally found to be slow rotators (Wickramasinghe & Ferrario, 2000). This apparent contradiction of the model can be easily solved. If the rotation and magnetic axes are misaligned, magneto-dipole radiation rapidly spins down the white dwarf — see, however, Timokhin (2006) and Spitkovsky (2006), where the time evolution of magnetospheres for axisymmetric and oblique rotators is described in detail. The evolution of the rotational velocity when both axes are misaligned (Benacquista et al., 2003) is:

$$\dot{\omega} = -\frac{2\mu^2\omega^3}{3Ic^3}\sin^2\alpha, \tag{5.2}$$

where I is the moment of inertia of the white dwarf, α is the angle between the magnetic and rotation axes and $\mu = BR_{\rm WD}^3$. Thus, the spin-down timescale is simply $\tau_{\rm MDR} = \omega/2\dot{\omega}$. Adopting the values resulting from our SPH simulations (Lorén-Aguilar et al., 2009) we obtain $\tau_{\rm MDR} \sim 2.4\times10^8/\sin^2\alpha$ yr, for a field strength $B = 10^7$ G. Hence, if both axes are perfectly aligned the remnant of the coalescence will be a high-field, rapidly rotating magnetic white dwarf. On the contrary, if both axes are nearly perpendicular magneto-dipole radiation efficiently brakes the remnant. Consequently, the very young, hot, ultramassive, slowly rotating magnetic white dwarfs 1RXS J0823.6−2525 and PG 1658+441, which have fields $\sim 3.5\times10^6$ G can be accommodated in our model. For instance, PG 1658+441 has an effective temperature $T_{\rm eff} \sim 30\,000$ K and a mass $M \sim 1.3\,M_\odot$ (Dupuis et al., 2003), which corresponds to a cooling age of $\sim 3.7\times10^8$ yr, while the time needed to brake the white dwarf equals to $\sim 8.4\times10^7$ yr if $\sin\alpha = 1$ is adopted. Thus, our model can account for the slow rotation rate of PG 1658+441, provided that the rotation and magnetic axes are misaligned. We also note at this point that given the small radii — or, equivalently, the small radiating surfaces — of massive white dwarfs, their cooling ages increase markedly for effective temperatures smaller than $\log T_{\rm eff} \lesssim 4.7$.

On the other hand, rapidly rotating magnetic white dwarfs — of which an example is RE J 0317−853, a very massive ($\sim 1.3\,M_\odot$) white dwarf belonging to a wide binary system (Külebi et al., 2010) — could be the result of nearly equal-mass mergers in which both axes are aligned. In this case no Keplerian disk is formed, so these white dwarfs will not show infrared excesses. If, on the contrary, the masses of the coalescing white dwarfs are different, the axes are not aligned, and the disk is able to survive for long enough times, a second-generation planetary system could be eventually formed (García-Berro et al., 2007) and tidal disruption and accretion of minor planets may contaminate the atmosphere of the white dwarf, resulting in

magnetic DAZ or DAZd white dwarfs possibly showing infrared excesses. Examples of such white dwarfs are NLTT 10480 (Kawka & Vennes, 2011) and G77−50 (Farihi et al., 2011), for which a satisfactory explanation is still lacking.

The geometry of the surface magnetic fields of white dwarfs has been investigated over the years using spectro-polarimetric observations. The available wealth of observations shows that, in almost all cases, magnetic white dwarfs have fields deviating strongly from dipolar structure. In particular, it appears that in most cases the geometry of the surface magnetic field corresponds to quadrupolar or higher multipoles — e.g., PG 1031+234 (Schmidt et al., 1986), REJ 0317−855 (Ferrario et al., 1997), HE 0241−0155 (Reimers et al., 2004), HE 1045−0908 (Euchner et al., 2005), or PG 1015+014 (Euchner et al., 2006). This means that the toroidal component of the magnetic field must be stable, and that a poloidal component should also be present. Our mechanism can also qualitatively reproduce these observations. Indeed, in the $\alpha\omega$ mechanism, convection is responsible for the generation of poloidal fields, whereas rotation is responsible for the generation of toroidal fields. Specifically, the energy available to generate the poloidal field component is $\rho v_{\rm conv}^2/2 \sim 4.0\times10^{20}$ erg, which is $\sim 10\%$ of the energy available to build the toroidal component, $\rho(\omega R)^2/2 \sim 5.5\times10^{21}$ erg. Thus, we expect that the magnetic field generated by the fast rotating convective shell will have both toroidal and poloidal field components. Moreover, it is well known that purely toroidal fields are unstable due to instability (Tayler, 1973). However, the existence of a small poloidal component is a sufficient condition for stability. Actually, recent numerical studies (Braithwaite, 2009) show that the energy stored in the poloidal field component can be as high as 80% of the total magnetic energy, and that even poloidal components 10^{-6} times smaller than the toroidal one are enough to warrant stability. Thus, toroidal fields generated by the rotating, convective shell produced in the merger of two double degenerates are stable, and moreover we expect that the magnetic fields generated in this way will have a complex geometry, in agreement with observations.

5.3 Magnetic white dwarfs in the solar neighborhood

To assess if our scenario can reproduce the observed number of high-field magnetic white dwarfs we have expanded an existing, state-of-the-art Monte Carlo code (García-Berro et al., 1999; Torres et al., 2002; García-Berro et al., 2004) designed to study the Galactic populations of single white dwarfs to deal with those of double degenerates. In our simulations we assumed that 50% of stars belong to binaries, and we normalized to the local disk density (Holmberg & Flynn, 2000). The initial primary masses were obtained using a standard initial mass function (Kroupa et al., 1993), and the initial mass ratios according to a flat distribution. Also, a constant star formation rate and a disk age of 10^{10} yr were adopted. Orbital separations and eccentricities were randomly drawn according to a logarithmic probability

distribution (Nelemans et al., 2001) and to a thermal distribution (Heggie, 1975), respectively. For each of the components of the binary analytical fits to detailed stellar evolutionary tracks were used (Hurley et al., 2000), which provide full coverage from the main sequence until advances stages of evolution. For the white dwarf stage the most recent cooling tracks of Renedo et al. (2010) were employed. The orbital evolution of each binary was computed taking into account circularization and synchronization (Hurley et al., 2002). We also considered mass losses through stellar winds. Specifically, we assumed that the evolution during the main sequence is conservative, and only after it we included stellar winds. The adopted mass-loss rate is that of Kudritzki & Reimers (1978) except on the AGB, for which the rate of Vassiliadis & Wood (1993) was used. Angular momentum losses due to magnetic braking and gravitational radiation were also included (Schreiber & Gänsicke, 2003; Zorotovic et al., 2010). The Roche lobe radius was computed using the most commonly used approximation (Eggleton, 1983), and during the overflow episodes both rejuvenation and ageing were taken into account (Hurley et al., 2002). For the common envelope phase we considered standard prescriptions for the common envelope efficiency and for the fraction of gravitational binding energy of the donor available to eject the envelope — see, e.g., Dewi & Tauris (2000). Specifically, we adopted $\alpha_{\rm CE} = 0.25$ and a variable value for the binding energy parameter λ (Zorotovic et al., 2010)). With all these ingredients we found that the fraction of merged double degenerate cores in the solar neighborhood is $\sim 2.9\%$ of the total synthetic population. This number includes not only white dwarf mergers ($\sim 0.3\%$), but also the coalescence of a white dwarf and a giant star with a degenerate core ($\sim 1.1\%$), and the merger of two giants with degenerate cores ($\sim 1.5\%$). In these two last cases — namely, the merger of a white dwarf and a giant, and the merger of two giant stars — the coalescences occur during the common envelope phase, while the merger of two white dwarfs is driven by gravitational wave radiation. Finally, we emphasize that the number of white dwarf mergers we obtain is in line with those obtained using completely different approaches (Bogomazov & Tutukov, 2009) — see below for a detailed comparison with our results for the solar neighborhood — and that the distribution of remnant masses is nearly flat, in accordance with the observed distribution of masses of magnetic white dwarfs (Należyty & Madej, 2004).

To better illustrate this last issue, Fig. 5.2 shows the frequency distribution of remnant masses of the different merger channels for a sample of 10^3 mergers. We assumed that the remnant of each coalescence has a mass $M = M_1 + M_2/2$, where M_1 and M_2 stand, respectively, for the masses of the primary and secondary degenerate cores. This choice is in accordance with the results of the SPH simulations of Lorén-Aguilar et al. (2009), which show that approximately half of the secondary is accreted onto the primary, while the rest of the mass of the disrupted secondary forms a debris region and little mass is ejected during the merger. We also eliminated all those remnants that have masses larger than Chandrasekhar's limit, while for the mergers producing a helium white dwarf we adopted the procedure of Hurley et al.

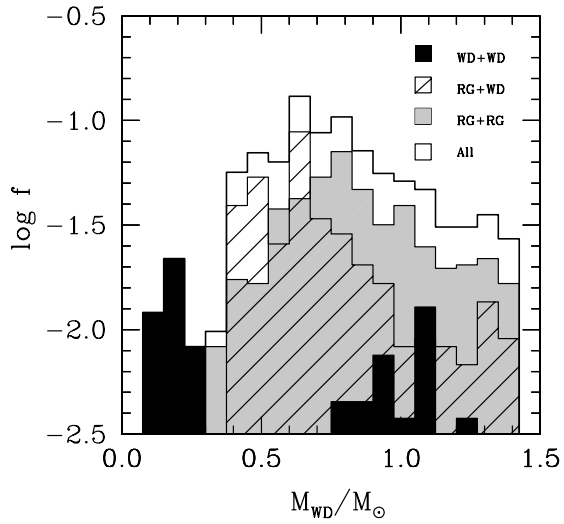

Figure 5.2: Mass distribution of the remnants of the mergers. The distribution shows the frequency of the different merger channels. The black histogram shows the masses of the remnants of the mergers of double white dwarf binaries, the dashed histogram that of the mergers of a binary system composed of a red giant and a white dwarf, the shaded histogram that of the mergers of two red giants, while the total mass distribution is shown using a solid line.

(2002). As can be seen, the total mass distribution (open histogram) presents a first peak for masses smaller than $\sim 0.4\,M_{\odot}$, corresponding to mergers in which a helium white dwarf is produced, then sharply increases for increasing remnant masses and afterwards smoothly decreases for masses larger than $\sim 0.6\,M_{\odot}$. When this distribution is sampled for ~ 26 objects with masses ranging from $0.8\,M_{\odot}$ to $1.4\,M_{\odot}$ we usually obtain fairly flat distributions, although the scarce number of objects and the subsequent large deviations prevent a sound comparison with the observational data.

Within 20 pc of the Sun there are 122 white dwarfs (Holberg et al., 2008), and several of them are magnetic (Kawka et al., 2007). This sample is 80% complete, but subject to poor statistics. However, it is useful because for it we have a reliable determination of the true incidence of magnetism in white dwarfs. Mass determinations are available for 121 of them. In the local sample there are 14 magnetic white dwarfs, 8 have magnetic fields in excess of 10^7 G, and 3 have masses larger than $0.8\,M_{\odot}$ — a value which is $\sim 2.5\sigma$ away from the average mass of field white dwarfs. The selection of this mass cut is somewhat arbitrary but, given the strong bias introduced by the initial mass function, we expect that the vast majority of high-field magnetic white dwarfs more massive than $0.8\,M_{\odot}$ would be the result of stellar mergers. This is indeed the case, since our population synthesis calculations

predict that ~ 4 white dwarfs are the result of double degenerate mergers, and have masses larger than $0.8\,M_{\odot}$, in good agreement with observations. Additionally, our simulations predict that the fraction of white dwarfs more massive than $\sim 0.8\,M_{\odot}$ resulting from single stellar evolution is $\sim 10\%$. Consequently, the expected number of massive white dwarfs in the local sample should be ~ 12. Instead, the local sample contains 20, pointing towards a considerable excess of massive white dwarfs, which could be the progeny of mergers. The rest of the population of magnetic white dwarfs (~ 5) would be well the result of the evolution of single stars (Aznar Cuadrado et al., 2004). In this case the magnetic field could have been generated during the red giant phase (Blackman et al., 2001), or could be a fossil of the evolution of magnetic Ap or Bp stars — see, for instance, Mathys et al. (2001) and references therein. Note, nevertheless, that it has been recently suggested that these massive main-sequence stars are also the result of stellar mergers (Tutukov & Fedorova, 2010).

The number of coalescing binaries previously discussed compares well with the results obtained using very different population synthesis codes. For instance, Bogomazov & Tutukov (2009), using a completely independent code, obtain $\sim 7 \pm 1$, where we have assumed poissonian errors, white dwarf mergers within 20 pc of the Sun — see their Table 1 — whereas we obtain $\sim 4 \pm 2$. Thus, within the sampling uncertainties, both numbers agree qualitatively, despite the very small number of objects and the existing theoretical uncertainties, which include, among others, the completely different approaches used to simulate a representative sample of binaries, the ingredients necessary to model the Galaxy as a whole, and the parameters adopted in the calculation of the common envelope phase.

5.4 Discussion

We have shown that the hot, convective, differentially rotating corona predicted by detailed three-dimensional simulations of the merger of two degenerate stellar cores is able to produce very high magnetic fields. We have also shown that these magnetic fields are confined to the outer layers of the remnant of the coalescence, and do not propagate neither to the interior of the white dwarf or to the debris region. Our model naturally predicts that high-field magnetic white dwarfs should preferentially have high masses, and should be observed as single white dwarfs, as observationally found. Moreover, if the rotation and magnetic axes are not aligned magnetodipole radiation rapidly spins down the magnetic white dwarf in short timescales. Thus, high-field magnetic white dwarfs may have a large variety of rotation periods. Moreover, in the case in which the masses of the coalescing white dwarfs are not equal the heavy rotationally supported disk can survive for long periods of time, and a planetary system could eventually form. Disruption of small planets could then contaminate the very outer layers of the magnetic white dwarf, explaining the recently discovered population of metallic magnetic white dwarfs. If, on the contrary, the

masses of the merging white dwarfs are similar the remnant has spherical symmetry and rotates very rapidly, as observed in some high-field magnetic white dwarfs. Also, the geometry of the surface magnetic fields can be well explained by our model. Finally, we have also shown that the expected number of double degenerate mergers is roughly consistent with the number of high-field magnetic white dwarfs in the local sample. In summary, our calculations indicate that a sizable fraction of all high-field magnetic white dwarfs could be the result of double degenerate mergers, in accordance with previous suggestions (Wickramasinghe & Ferrario, 2000) not hitherto proven.

Chapter 6

A white dwarf merger as progenitor of the Anomalous X-ray Pulsar 4U 0142+61?

It has been recently proposed that massive fast-rotating highly-magnetized white dwarfs could describe the observational properties of some Soft Gamma-Ray Repeaters (SGRs) and Anomalous X-Ray Pulsars (AXPs). Moreover, it has also been shown that high-field magnetic white dwarfs can be the outcome of white dwarf binary mergers. The products of these mergers consist of a hot central white dwarf surrounded by a rapidly rotating disk. Here we show that the merger of a double degenerate system can explain the characteristics of the peculiar AXP 4U 0142+61. This scenario accounts for the observed infrared excess. We also show that the observed properties of 4U 0142+61 are consistent with a $\sim 1.2\,M_{\odot}$ white dwarf, remnant of the coalescence of an original system made of two white dwarfs of masses $0.6\,M_{\odot}$ and $1.0\,M_{\odot}$. Finally, we infer a post-merging age $\tau_{\rm WD} \approx 64$ kyr, and a magnetic field $B \approx 2 \times 10^8$ G. Evidence for such a magnetic field may come from the possible detection of the electron cyclotron absorption feature observed between the B and V bands at $\approx 10^{15}$ Hz in the spectrum of 4U 0142+61.

6.1 Introduction

SGRs are sources of short ($\sim$ 100 ms), repeating bursts of soft γ-ray and X-ray radiation at irregular intervals, and share with AXPs several similarities, like rotation periods clustered between 2 and 12 s, and high magnetic fields. Their observed spindown rates range from $\dot{P} \sim (10^{-15}$ to $10^{-10})$, and have typical X-ray luminosities in quiescent state $L_X \sim 10^{35}$ ergs^{-1}. Currently, it is widely accepted that these objects are magnetars (Duncan & Thompson, 1992; Thompson & Duncan, 1995), although there are competing scenarios that challenge this model — see, for instance,

Table 6.1: Bounds for the mass, radius and moment of inertia of 4U 0142+61.

	Minimum	Maximum
M ($M_\odot$)	1.16	1.39
$R_{\rm eq}$ (10^8 cm)	1.05	6.66
$\langle R \rangle$ (10^8 cm)	1.05	6.03
I (g cm^2)	2.9×10^{48}	1.4×10^{50}

the excellent and recent review of Mereghetti (2008), and references therein. Recently, Malheiro et al. (2012), following the pioneering works of Morini et al. (1988) and Paczynski (1990), have suggested an alternative model that could explain some properties of these sources. This model involves highly-magnetized white dwarfs. For this model to be viable the masses of the white dwarfs need to be rather large ($M \gtrsim 1.2\,M_\odot$), their magnetic fields should range from $B \approx 10^7$ G all the way to 10^{10} G, and the rotation periods should be rather small, of the order of a few seconds. The most apparent drawback of this scenario, namely the rotational stability of fast rotating white dwarfs, has been recently analyzed. Specifically, the crucial question of whether rotating white dwarfs can have rotation periods as short as the ones observed in AXPs has been recently addressed by Boshkayev et al. (2013b), who found that the minimum rotation period of typical carbon-oxygen white dwarfs is ~ 0.5 s. Thus, since AXPs have rotation periods larger than this value they could be white dwarfs.

The existence of white dwarfs with magnetic fields ranging from 10^7 G up to 10^9 G is solidly confirmed by observations (Külebi et al., 2009). Observations show that most high-field magnetic white dwarfs are massive, and moreover, that none of them belongs to a non-interacting binary system, pointing towards a binary origin. However, although long-suspected (Wickramasinghe & Ferrario, 2000), it has only been recently shown that they might be the result of white dwarf mergers. SPH simulations of the coalescence process indicate that the result of the merger is a white dwarf that contains the mass of the undisrupted primary, surrounded by a hot corona made of about half of the mass of the disrupted secondary. In addition, a rapidly rotating Keplerian disk which contains the rest of the material of the secondary is also formed, as little mass is ejected from the system during the coalescence process. The rapidly-rotating hot corona is convective and an efficient $\alpha\omega$ dynamo can produce magnetic fields of up to $B \sim 10^{10}$ G, as shown in chapter 5.

In view of these considerations it is natural to ask ourselves if such binary mergers could also explain the properties of some AXPs. Here we explore such possibility for the specific case of the peculiar AXP 4U 0142+61. This AXP is by far the best observed source in the near-infrared (NIR), optical, and ultraviolet (UV) bands

and has two characteristics that make it a peculiar object. The first one is that 4U 0142+61 presents a confirmed infrared excess (Hulleman et al., 2000) that might be attributed to an accretion disk, whereas the second one is that it is too bright for its cooling age, thus challenging the conventional magnetar model. Here we show that the properties of this AXP can be well explained by a model in which the central compact remnant is a massive magnetized white dwarf resulting from the merger of two otherwise ordinary white dwarfs, surrounded by the heavy accretion disk produced during the merger.

6.2 A model for 4U 0142+61

To start with, we compute the approximate mass and radius of 4U 0142+61. The stability of general relativistic uniformly rotating white dwarfs has been recently studied (Boshkayev et al., 2013b), and it has been shown that constant rotation period sequences intersect the stability region of white dwarfs in two points that determine lower and upper bounds for the mass, equatorial/polar radii and moment of inertia. In Table 6.1 we show the bounds for 4U 0142+61. In this table $\langle R\rangle = (2R_{\rm eq} + R_{\rm p})/3$ denotes the mean-radius, where $R_{\rm eq}$ and $R_{\rm p}$ are, respectively, the equatorial and polar radii.

6.2.1 IR, optical and UV photometry

We next fitted the spectrum of 4U 0142+61 as the sum of two components. The first one is a black body:

$$F_{\rm BB} = \pi \frac{2h}{c^2}\left(\frac{R_{\rm WD}}{d}\right)^2 \frac{\nu^3}{e^{h\nu/(k_{\rm B}T_{\rm eff})}-1}\,, \tag{6.1}$$

where $R_{\rm WD}$ and $T_{\rm eff}$ are, respectively, the radius and effective temperature of the white dwarf. As it will be shown in Sect. 6.2.2, the system now behaves as an ejector, inhibiting the accretion of the disk material onto the central white dwarf. Thus, for the second component we adopted the black body disk model of Chiang & Goldreich (1997), which is more appropriate for these systems (García-Berro et al., 2007):

$$F_{\rm disk} = 12\pi^{1/3}\cos i\left(\frac{R_{\rm WD}}{d}\right)^2\left(\frac{2k_{\rm B}T_{\rm eff}}{3h\nu}\right)^{8/3}\left(\frac{h\nu^3}{c^2}\right)\times\int_{x_{\rm in}}^{x_{\rm out}}\frac{x^{5/3}}{e^x-1}dx\,, \tag{6.2}$$

where i is the inclination angle of the disk, which we assume to be face-on, and $x = h\nu/(k_{\rm B}T)$. In this model the disk temperature T varies as $r^{-3/4}$ (Chiang & Goldreich, 1997), with r the distance from the center of the white dwarf. It is worth mentioning that in previous studies of 4U 0142+61 (Hulleman et al., 2000; Wang et al., 2006) the irradiated disk model of Vrtilek et al. (1990) has been used instead, but this model is more appropriate for accreting sources.

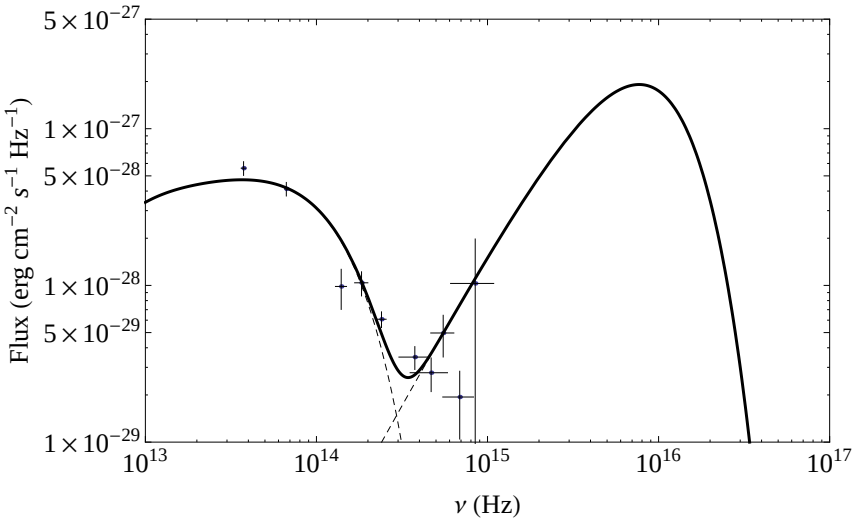

Figure 6.1: Observed and fitted spectrum of 4U 0142+61. Due to the high variability of the source in the optical bands we average all the existing data of the source in the different bands. All these data come from observations from 31 October 1994 up to 26 July 2005 (Hulleman et al., 2000, 2004; Dhillon et al., 2005; Morii et al., 2005; Durant & van Kerkwijk, 2006c; Morii et al., 2009). The result of the average is $V = 25.66$, $R = 25.25$, $I = 23.76$, $J = 22.04$, $H = 20.70$, $K = 19.97$. There are upper limits in the U and B bands, $U = 25.8$ (Dhillon et al., 2005) and $B = 28.1$ (Hulleman et al., 2004), respectively. We also consider the observations of Wang et al. (2006) with the Spitzer/IRAC instrument at wavelengths 4.5 μm and 8.0 μm. The fluxes are 36.3 μJy and 51.9 μJy, respectively. We corrected the data for the interstellar extinction, using the estimated distance $d = 3.6$ kpc (Durant & van Kerkwijk, 2006a) and an absorption in the V band $A_V = 3.5$ (Durant & van Kerkwijk, 2006b). For the rest of the bands we used $A_U = 1.569A_V$, $A_B = 1.337A_V$, $A_R = 0.751A_V$, $A_I = 0.479A_V$, $A_J = 1.569A_V$, $A_J = 0.282A_V$, $A_H = 0.190A_V$, and $A_K = 0.114A_V$ (Cardelli et al., 1989). The extinction in the Spitzer/IRAC bands for $A_K < 0.5$ are $A_{4.5\mu\mathrm{m}} = 0.26A_K$ and $A_{8.0\mu\mathrm{m}} = 0.21A_K$ (Chapman et al., 2009).

We computed the best-fit of the spectrum parameters, finding $R_{\mathrm{WD}} \approx 0.006\,R_\odot$, $T_{\mathrm{eff}} \approx 1.31 \times 10^5$ K, inner and outer disk radii $R_{\mathrm{in}} = 0.97\,R_\odot$, $R_{\mathrm{out}} = 51.1\,R_\odot$ and correspondingly inner and outer disk temperatures $T_{\mathrm{in}} \approx 1950$ K and $T_{\mathrm{out}} \approx 100$ K, respectively. In Fig. 6.1 we show the photometric data of 4U 0142+61 and our best-fit composite spectrum. The agreement of the composite spectrum with the observational data is quite good, taking into account that the high variability of the source in these bands can lead to changes in the optical fluxes of up to one order of magnitude (Durant & van Kerkwijk, 2006c). Thus, the white dwarf model is compatible with the observed photometry of 4U 0142+61, as it seems to occur for SGR 0418+5729, Swift J1822.3–1606, and 1E 2259+586 (Boshkayev et al., 2013a).

To check whether this is a realistic and consistent model for 4U 0142+61, we ran

a SPH simulation of the merger of a $0.6 + 1.0\,M_\odot$ binary white dwarf, which results in a central remnant of $\approx 1.1\,M_\odot$, with a radius $R_{\rm WD} \approx 0.006\,R_\odot$, in agreement with the photometric value. We recall that the central white dwarf will accrete some material from the surrounding disk (of mass $M_{\rm disk} \approx 0.5\,M_\odot$) and, thus, will shrink a little. Moreover, the rotation period is $P \approx 15.7$ s and the moment of inertia of the central white dwarf and the hot corona is $I \approx 2.0 \times 10^{50}$ g cm^2, which is slightly larger than our maximum estimate — see Table 6.1. Furthermore, the magnetic field generated in the differentially-rotating hot corona produced in the aftermath of the merger amounts to $B \sim 10^{10}$ G (García-Berro et al., 2012) which amply explains the magnetic field of 4U 0142+61, see section 6.2.2.

6.2.2 The age and magnetic field of 4U 0142+61

The presence of a disk around the magnetized white dwarf plays a key role in the evolution of its rotation period. This results from a delicate interplay between the interaction of the disk with the magnetosphere of the star, and accretion of disk matter onto the surface of the white dwarf. A solution of the magneto-hydrodynamic equations including the explicit coupling of magnetosphere-disk system and the mass and angular momentum transfer from the disk to the star is not yet available. For this reason the torque acting on the star it is often followed using a phenomenological treatment. We adopt the model of Armitage & Clarke (1996), which assumes that the magnetic field lines threading the disk are closed. In this model the evolution of ω is dictated by

$$\dot{\omega} = -\frac{2B^2\langle R\rangle^6\omega^3}{3Ic^3}\sin^2\theta + \frac{B^2\langle R\rangle^6}{3I}\left[\frac{1}{R_{\rm mag}^3} - \frac{2}{(R_{\rm c}R_{\rm mag})^{3/2}}\right] + \frac{\dot{M}R_{\rm mag}^2\omega}{I}, \qquad (6.3)$$

where θ is the angle between the rotation axis and the magnetic dipole moment, $R_{\rm mag} = [B^2\langle R\rangle^6/(\dot{M}\sqrt{2GM})]^{2/7}$ is the magnetospheric radius (Chatterjee et al., 2000; Toropina et al., 2012; Matt et al., 2012; Rueda & Ruffini, 2012), and $R_{\rm c} = (GM/\omega^2)^{1/3}$ is the corotation radius. The first term in Eq. (6.3) describes the traditional magneto-dipole braking, the second one is the star-disk coupling, while the last one describes the angular momentum transfer from the disk to the white dwarf. We adopt an accretion rate corresponding to a Shakura-Sunyaev viscosity parameter $\alpha_{\rm SS} = 0.1$ (Cannizzo et al., 1990; Chatterjee et al., 2000; Ertan et al., 2009). Adopting a misalignment angle $\theta = \pi/2$ and integrating Eq. (6.3) using the parameters resulting from our SPH simulation and it results that, for a wide range of magnetic field strengths, at early stages $R_{\rm mag} \approx R_{\rm WD}$. Thus, initially the star is spun-up due to the large accretion rates — see the insets of Fig. 6.2. However, after ~ 1 kyr, the inner radius of the disk — which is approximately given by the magnetospheric radius — becomes larger than the the light cylinder radius, $R_{\rm lc} = c/\omega$. Hence, the disk cannot torque any longer the white dwarf, the rotation period reaches a minimum, and from this point on the disk and the star evolve independently, and

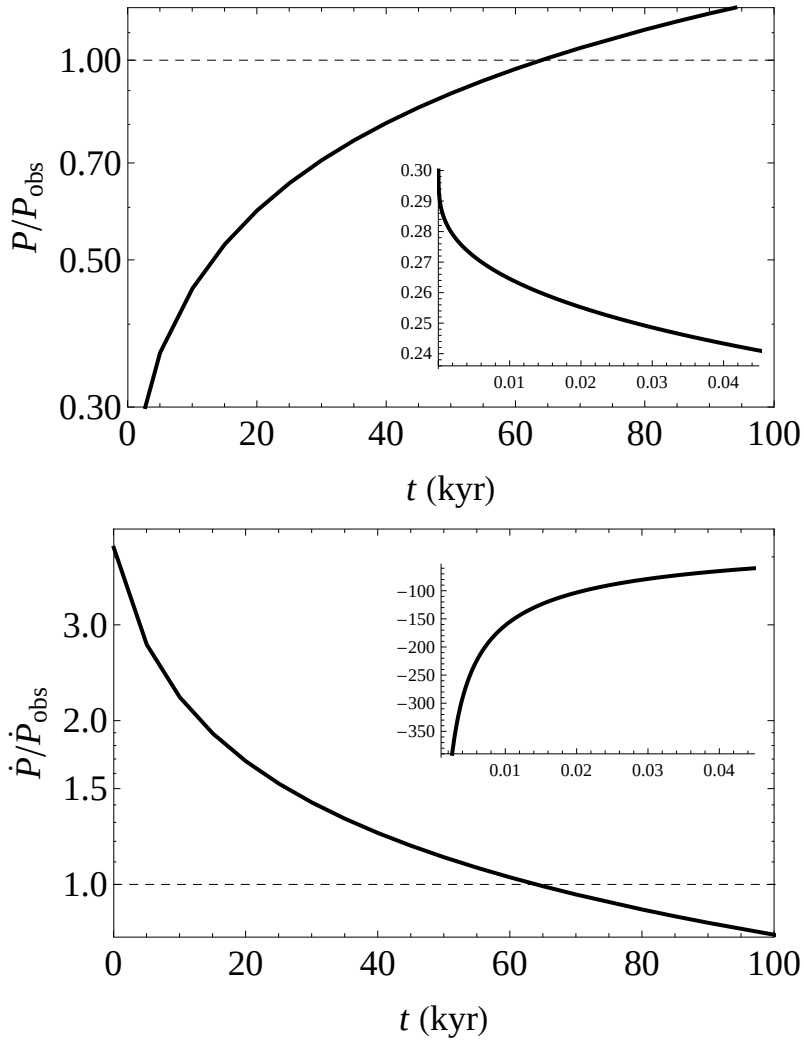

Figure 6.2: Time evolution of the period (top panel) and period derivative (bottom panel) of 4U 0142+61. The insets show to the early evolutionary phases of the system.

accretion onto the magnetic poles stops. Thus, the star behaves as a normal pulsar, spinning-down by magneto-dipole radiation (Lamb et al., 1973; Chatterjee et al., 2000). The surface magnetic field needed to fit the observed values of P and $\dot{P}$ when a mass $M = 1.2\,M_{\odot}$ is adopted is $B \approx 2.3 \times 10^8$ G at an age $\tau_{\rm sd} = 64$ kyr — see Figure 6.2. This age estimate compares well with the spin-down characteristic age $P/(2\dot{P}) \approx 68$ kyr. Moreover, the strength of the magnetic field can be compared with that directly derived using the traditional misaligned dipole expression

$$B = \sqrt{\frac{3c^3 I}{\langle R \rangle^6} \frac{P\dot{P}}{8\pi^2}}\,, \tag{6.4}$$

(Ferrari & Ruffini, 1969; Lamb et al., 1973) — which in our case is valid because $R_{\rm in} \approx R_\odot$ (see section 6.2.1) is larger than the radius of the light cylinder $R_{\rm lc} \approx 0.6\,R_\odot$. From the observed values $P = 8.69$ s and $\dot{P} = 2.03 \times 10^{-12}$ (Hulleman et al., 2000), we obtain $B = 2.3 \times 10^8$ G for $M_{\rm min}$, and 6.2×10^9 G for $M_{\rm max}$, in agreement with the result obtained integrating Eq. (6.3). Additionally, there are other indications that the magnetic field derived in this way is sound. In particular, the spectrum of 4U 0142+61 exhibits a significant drop-off between the B and V bands, at a frequency $\nu \approx 10^{15}$ Hz, see Fig. 6.1. Hulleman et al. (2004) concluded that this feature is not due to variability and, moreover, they advanced that it is consistent with the electron cyclotron emission of a magnetic field $B \sim 10^8$ G. Adopting the minimum and maximum masses derived from our model we obtain electron cyclotron frequencies $\nu_{\rm cyc} = eB/(2\pi m_{\rm e} c) = 6.3 \times 10^{14}$ Hz and 1.7×10^{16} Hz, which correspond to wavelengths that fall between the NIR and the UV, 0.5 and 176 μm, respectively. This suggests that the magnetic field must be closer to the lower value, and therefore that the corresponding mass should be $\sim 1.2\,M_\odot$. Actually, it is interesting to realize that although the mass of the remnant of the coalescence is slightly smaller than our fiducial mass for 4U 0142+61 — ~ 1.1 and $\sim 1.2\,M_\odot$, respectively — the mass accreted during the spin-up phase is $M_{\rm acc} \sim 0.05\,M_\odot$, in good agreement with the mass derived from the photometric solution. It could be argued that this is the maximum possible accreted mass, since during these early stages super-Eddington accretion rates are needed to accrete all the material inflowing from the disk. Nevertheless, during the very early stages after the merger the temperature of the coalesced system is very high, and the emission of neutrinos is not negligible (García-Berro et al., 2012).

We now compute the cooling age of 4U 0142+61, and compare it with the spin-down age. As the hot, convective corona resulting from the merger is very short-lived (García-Berro et al., 2012) the evolution of the surface luminosity of the white dwarf can be estimated using Mestel's cooling law (Mestel, 1952):

$$\tau_{\rm cool} = \frac{1}{\langle A \rangle} \left(\frac{bMZ^{2/5}}{L_{\rm WD}} \right)^{1/x} - 0.1\,, \tag{6.5}$$

where $\langle A \rangle$ is the average atomic weight of the core of the white dwarf, Z is the metallicity of its envelope, $x = 1.4$, $b = 635$ (Hurley & Shara, 2003), and the rest of the symbols have their usual meaning. Adopting a carbon-oxygen core and $Z \approx 0.001$, which is a reasonable value (Althaus et al., 2010), we obtain a cooling age $\tau_{\rm cool} \approx 64$ kyr, in good agreement with the spin-down age.

6.2.3 X-ray luminosity

For a distance $d = 3.6$ kpc, Durant & van Kerkwijk (2006a) estimated an isotropic X-ray luminosity $L_X = 4\pi d^2 f_X^{\rm unabs} \approx 1.3 \times 10^{35}$ erg s^{-1}, using the unabsorbed X-ray flux $f_X^{\rm unabs} = 8.3 \times 10^{-11}$ erg s^{-1} cm^{-2} obtained by Patel et al. (2003). We use the result of the latest observations of 4U 0142+61 with the EPIC cameras onboard *XMM-Newton*, $f_X^{\rm unabs} = 7.2 \times 10^{-11}$ erg s^{-1} cm^{-2} (Göhler et al., 2005), obtaining $L_X \approx 1.1 \times 10^{35}$ erg s^{-1} when the same distance is adopted. The loss of rotational energy associated with the spin-down of 4U 0142+61, $\dot{E}_{\rm rot} = -4\pi^2 I \dot{P}/P^3$ gives $|\dot{E}_{\rm rot}| = 1.7 \times 10^{37}$ erg s^{-1} for $M_{\rm min}$ and 3.4×10^{35} erg s^{-1} for $M_{\rm max}$, that cover the estimated X-ray luminosity.

The time integrated X-ray spectrum of 4U 0142+61 is well described by a black body and a power-law model with $k_{\rm B}T_{\rm BB} = 0.4$ keV and photon index $\Gamma = 3.62$ (Göhler et al., 2005). The black body component corresponds to a temperature $T_{\rm BB} \sim 4.6 \times 10^6$ K, which is higher than the surface temperature of a hot white dwarf. However, these systems may have coronal temperatures much higher than that of the surface (Malheiro et al., 2012), and thus the X-ray emission would be of magnetospheric origin. Because the inner radius of the disk is larger than the radius of the light cylinder $R_{\rm lc}$ (see section 6.2.2) the mechanisms producing such radiation are similar to those of pulsars. In particular, a possible mechanism was delineated by Usov (1993), who showed that reheating of the magnetosphere by the bombardment of positrons moving backward to the surface of the star can produce large X-ray luminosities. Positrons are produced the interaction of high-energy photons with ultra-relativistic electrons, resulting in the creation of electron-positron pairs. Following closely the calculations of Usov (1993) we computed the theoretically expected X-ray luminosity of 4U 0142+61. We found that the reheating of polar caps produces a persistent X-ray luminosity $L_X \sim 2 \times 10^{35}$ erg s^{-1}, in agreement with observations. Nonetheless, there are other possibilities. If the conventional magnetar interpretation is adopted, the X-ray luminosity would be due to the neutron star. Alternatively, it could also be due to ongoing accretion from a fossil disk onto the neutron star (Alpar, 2001). In such cases the white dwarf product of the merger would have accreted enough material to undergo accretion induced collapse to a neutron star.

6.3 Conclusions

We studied the possibility that the peculiar AXP 4U 0141+61 is a massive, fast-rotating, highly magnetized white dwarf, and we explored the viability of this object being the result of the coalescence of a binary white dwarf. Specifically, from its observed rotational velocity we first derived bounds for the mass, radius, and moment of inertia. Afterwards, we fitted the IR, optical, and UV data of 4U 0142+61 with a composite spectrum made of two components, a black body and a dust disk, finding a

good agreement with the observations. Moreover, we showed that the characteristics of the disk are consistent with the results of a SPH simulation of the merger of a $0.6 + 1.0\,M_{\odot}$ binary system. We then estimated the age and the magnetic field of this AXP. Adopting the results of our SPH simulation we obtained a magnetic field $B = 2.3 \times 10^8$ G, and a post-merger age ≈ 64 kyr. The cyclotron frequency of this magnetic field $\nu_{\rm cyc} \sim 6 \times 10^{14}$ Hz would explain an absorption feature observed in the spectrum of 4U 0142+61 at $\nu \sim 10^{15}$ Hz. Furthermore, our age estimate is in excellent agreement with the white dwarf cooling age. We also showed that the X-ray luminosity of 4U 0142+61 can be well explained by the rotational energy loss, and we inferred a theoretical estimate $L_X \approx 2 \times 10^{35}$ erg s^{-1}, which agrees with the observed value, $L_X \approx 1.09 \times 10^{35}$ erg s^{-1}. All these findings may support the hypothesis that the peculiar AXP 4U 0141+61 was originated in a white dwarf binary merger.

Chapter 7

Conclusions

The aim of the present thesis was to study some unexplored interactions between two white dwarfs. In particular, we have studied the core-degenerate scenario for Type Ia supernovae and the possibility that some white dwarf collisions might produce a thermonuclear supernova. The latter scenario is a variant of the double-degenerate scenario, while the former was never investigated before. We have also considered the possibility that some white dwarf merger remnants could be associated to some high-field magnetic white dwarfs and to anomalous X-ray pulsars, of which 4U 0142+61 is the leading example.

To this end, we have firstly improved an existing Smoothed Particle Hydrodynamics code used in previous simulations of this kind. Since the simulations presented here require, in some cases, very short integration timesteps ($\sim 10^{-5}$ s) to ensure energy conservation, one of the most important tasks performed in this work consisted of parallelizing the existing code. This has lead to a considerable reduction of the computational time, when Message Passing Interface (MPI) libraries are employed. We also utilized some modules and a set of libraries for vector operations. All the calculations presented in this work were done on a newly implemented computer cluster, with improved hardware. Details about the parallization procedure can be found in the appendix of this thesis, where we also describe the hardware characteristics of the computer cluster. Additionally, we have also improved the accuracy of the results, by introducing a new algorithm to preserve energy and angular momentum conservation to the best possible accuracy. This is explained in more detail in the appendix, where we describe how the energy is best conserved by following simultaneously the evolution of the temperature and of the internal energy, as well as some other interesting technical details. This new algorithm turned out to be essential to ensure the consistency of the results when long runs were needed. Specifically, adopting the prescriptions explained in the appendix, energy is conserved at the level of 1%, and angular momentum at the level of 10^{-3}% in all simulations for very long integration times. Lastly, we also updated some key physical ingredients needed

for the calculation of up-to-date simulations. In particular, for those simulations in which the temperatures are such that nuclear reactions play a leading role, an accurate and complete nuclear network is also important. Within the framework of this thesis we implemented such an updated nuclear network, based on the most recent nuclear cross sections. Not only that, we also modified the existing SPH code to implement the Helmholtz equation of state, which is the most accurate one and has become a "de facto" standard, since it warrants thermodynamic consistency.

Having explained the most important improvements made to our numerical code we elaborate on the most salient results of our simulations. To start with, it is particularly relevant to mention that we have performed the first set of realistic simulations of the core-degenerate scenario. This scenario shares some similarities with the core-degenerate scenario, but at odds with the latter, one of the coalescing stars is not a white dwarf, but instead the core of an AGB star. It is thought that during the final stages of the common envelope phase, when the envelope surrounding the cold white dwarf and the hot AGB core is ejected, up to $\sim 10\%$ of the envelope falls back and forms a circumbinary disk. If the disk is massive enough, its interaction with the binary increases the eccentricity of the orbit and decreases its semi-major axis to such an extent that a merger between both stars seems to be unavoidable. On the contrary, if the disk is not massive enough, most of its mass is ejected from the system before the orbit of the binary system is close enough to drive a merger. In this case, both stars are brought closer by the emission of gravitational waves. This mechanism acts for much longer timescales and does not ensure that the core of the AGB star is going to be hot once the coalescence begins. Most importantly, in this case it has been shown that the orbit is nearly circular, hence very similar to that adopted in the existing simulations of the core-degenerate scenario. Adopting the procedure employed by Kashi & Soker (2011) to compute the orbital evolution of the binary system, we have first calculated at which stage the stars are close enough to start mass transfer. These orbital parameters were used as initial conditions to simulate the merger process itself. Moreover, in order to quantify the influence of the temperature of the core of the AGB star, we compute for both eccentricities a simulation for which the core of the AGB star is cold, and another one in which we adopt a larger temperature.

Our results demonstrate that the eccentricity of the binary system plays an important role on the dynamics of the merger and also in shaping the final remnant, whereas the initial temperature does not. Eccentric mergers last for much longer times, typically hours, than those of almost circular events, but the number of mass transfer episodes at closest approach is smaller, and more mass is transferred to the primary during each one of these episodes. This results in larger ejected and fallback masses, of the order of $10^{-2}\,M_{\odot}$. In the almost circular mergers that is, with eccentricities $e \sim 0.1$, the mass transfer episodes, and therefore the evolution of the coalescence, is less violent. In these cases the mass of the ejecta is $\sim 10^{-4}\,M_{\odot}$, and the mass of the fallback material is $\sim 10^{-3}\,M_{\odot}$. We have also found that the

general structure of the merged remnants is the same found for double-degenerate coalescences. It consists of the almost unperturbed core of the AGB star, surrounded by a hot differentially rotating corona. The corona contains $\sim 18\%$ of the disrupted white dwarf for eccentric mergers, and is somewhat larger, $\sim 27\%$, for mergers with nearly circular orbits. Surrounding this central compact object a heavy Keplerian disk and an extended shroud, both formed by the rest of the mass of the disrupted white dwarf, can be found. In mergers with eccentric orbits the debris region has ellipsoidal shape, whereas for mergers with nearly circular orbits little mass is found in the polar regions around the central object. The conversion of the orbital angular momentum to rotational one results in sizable rotational velocities of the central compact object, which rotates as a rigid body at $\sim 18\ \mathrm{s}^{-1}$ and $\sim 22\ \mathrm{s}^{-1}$, respectively, for mergers resulting from the evolution of massive circumstellar disks and those resulting from less massive ones. Also the peak velocities of the corona are larger for the non-eccentric mergers, a consequence of the dynamical evolution during the merger.

For the case of white dwarf collisions, we enlarged the parameter space studied by Lorén-Aguilar et al. (2010), thus extending their work to cover more general possibilities. Specifically, we have considered 6 white dwarf masses and several different trajectories of the interacting white dwarfs, performing a total of 71 simulations. As already discussed by Lorén-Aguilar et al. (2010) there are three possible outcomes for these dynamical interactions. The first possibility is that the interaction results in the formation of an eccentric binary. The second one is a lateral collision, in which several mass transfer episodes occur. Finally, the last possibility is a direct collision, in which only one catastrophic mass transfer episode takes place. For sufficiently small distances at closest approach of the interacting white dwarfs the outcome is a direct collision. For carbon-oxygen white dwarfs, this occurs when there is a substantial overlap (35%) of both stars at closest approach, resulting in a total disruption of the less massive star. In several direct collisions the material of the disrupted less massive secondary reaches the critical densities and temperatures to be ignited explosively, being this more frequent for helium white dwarfs, as it should be expected. As the distance at closest approach increases the outcome of the interaction is a lateral collision. Finally, for large distances at closest approach an eccentric binary is formed. The transition between these regimes is naturally related to the Roche lobe of the less massive white dwarf, R_{L}. In particular, when the radius of the secondary star is larger than $0.95\,R_{\mathrm{L}}$ at closest approach, a lateral collision occurs, whereas if it is smaller an eccentric binary is formed.

We analyzed as well the possible observational signatures of these dynamical interactions. In short, we studied the emission of gravitational waves, the neutrino signal, the light curves and the X-ray luminosity produced by the fallback material. For the case of those interactions in which an eccentric binary is formed we demonstrated that the gravitational wave emission would be detectable by eLISA in all cases but in those interactions in which the merging stars have small masses

and the eccentricity of the binary system is small. This is not the case for the lateral collisions. However, the remnants of lateral collisions have a strong fall-back X-ray emission that could be eventually detectable. Specifically, these interactions have peak X-ray luminosities of $\sim 10^{44}$ erg s^{-1}. Moreover, the light curve decays as a power law with index $-5/3$. In direct collisions the physical conditions for a detonation are met in several cases. This is not the case for lateral collisions. In most lateral collision a few SPH particles reach detonation conditions, but the detonation front is rapidly quenched and does not develop. At odds, in most direct collisions a vigorous detonation develops and the final explosion results in the total disruption of either the less massive white dwarf or both stars. For those dynamical interactions in which a powerful explosion develops we computed the late-time bolometric light curves, obtaining a broad range of variability, depending of course on the mass of synthesized nickel. For instance, direct collisions involving massive enough white dwarfs, such as the $0.8\,M_{\odot} + 1.0\,M_{\odot}$ and $0.8\,M_{\odot} + 1.2\,M_{\odot}$ systems, have peak luminosities typical of normal Type Ia supernovae. For these events, given that the temperatures and densities attained during the merger are rather high, we also assesed the possibility of detecting the neutrino signal in a Super-Kamiokande detector. However, we found that even for the most favorable conditions, when the energy threshold of noise is zero, just ~ 0.04 neutrinos would be detectable for the $0.8\,M_{\odot} + 1.0\,M_{\odot}$ direct collision at a maximum distance of 1 kpc. Finally, the single narrow pulse of gravitational wave radiation that is produced in direct collisions will not be detected by the current or planned gravitational wave detectors.

We also studied the possibility that some of the mergers studied in this work and in previously computed double-degenerate mergers may be the progenitors of high-field magnetic white dwarfs. We have proved that the material accreted by the unperturbed more massive star has a hot, differentially-rotating corona. The temperature gradients in this region are large, and convection sets in. This region is therefore prone to magneto-rotational instability. The resulting $\alpha\omega$ dynamo produces high magnetic fields, with typical values of $\sim 10^7$ G, which moreover do not diffuse outwards neither penetrate in the primary, remaining confined to the surface layers. This model naturally answers one observational property of high-field magnetic white dwarfs. In particular, it predicts that on average high-field magnetic white dwarfs should be more massive than regular field white dwarfs. However, it is also observationally found that, in general, high-field magnetic white dwarfs are slow rotators, while we found that the remnants of double-degenerate mergers rotate fast initially. To solve this eventual discrepancy we argued that the merger remnant can be braked to a large extent through magneto-dipole radiation, if the rotation and magnetic axes are misaligned. Moreover, in a follow-up paper Külebi et al. (2013) found that, even if magneto-dipole radiation is not efficient enough to slow down the remnants to the observed rotation periods, the magnetospheric interaction of the white dwarfs with the Keplerian disk results in a significant spin-down. They reproduce the observed rotation periods for magnetic white dwarfs of $\sim 10^7$ G with

this braking mechanism. Finally, we have also shown that in the local sample the expected number of double-degenerate mergers is roughly consistent with the number of high-field magnetic white dwarfs.

Having shown the feasibility of generating high-field magnetic white dwarfs in double-degenerate mergers, we also studied the possibility of reproducing the observational properties of the anomalous X-ray pulsar 4U 0142+61, assuming that it is the remnant of the coalescence of a binary white dwarf system. To this end we used the results of Boshkayev et al. (2013b) to approximate the mass and radius of this star. This study is the more recent calculation of the theoretical mass-radius relationship of general-relativistic, uniformly rotating white dwarfs. With these data we were able to fit simultaneously the IR, optical and UV fluxes of this AXP employing a composite spectrum of a black blody and a dust disk. Having done so, we obtained that the mass of the white dwarf, and found that the characteristics of the disk resemble those obtained from our simulated remnant of the coalescence of a $0.6\,M_\odot + 1.0\,M_\odot$ white dwarf binary system. Using the results all the above mentioned data we were able to estimate the age, the magnetic field and the X-ray luminosity from rotational energy loss. The inferred age, ≈ 64 kyr, is in agreement with the white dwarf cooling age, and the X-ray luminosity, $\approx 2\times10^{35}$ erg s^{-1} agrees with the observed value, while the magnetic field needed to explain the observations is $B \approx 2.3\times10^{8}$G. Finally, we also found that the cyclotron frequency associated to this magnetic fiel could explain the absorption feature observed in the spectrum at $\sim 10^{15}$ Hz, an interesting result.

In summary, in this work we have computed several coalescences of two white dwarfs, under different assumptions, and for various scenarios. We have also searched for the observational counterparts of these interactions, and found that both AXPs and high-field magnetic white dwarfs could be the result of mergers in which a powerful detonation does not occur. On the contrary, we have found as well that for some of our mergers a powerful detonation is very likely, leading to a thermonuclear (Type Ia) supernova outburst. Depending on the initial conditions, masses and physical characteristics of the coalescing stars the nickel masses synthesized during the most violent phases of the dynamical interaction show a large range of variation, and so do the peak bolometric luminosities. Moreover, for the interactions studied here we have characterized as well their observational properties. This includes not only the nucleosynthesis, but also the late-time light curve, the neutrino signal, the gravitational wave radiation pattern, and the fall-back luminosities, thus presenting a multimessenger picture of these processes. Of course, much remains still to be done, but the present work represents an important step forward that will need to be eventually expanded and completed in the future.

Appendix A

Characteristics of the SPH code

The hydrodynamic evolution of the interacting white dwarfs has been followed using a Smoothed Particle Hydrodynamics (SPH) code. SPH is a Lagrangian particle numerical method. It was first proposed by Lucy (1977) and, independently, by Gingold & Monaghan (1977). The basic principle of SPH methods consists in discretizing the fluid in a set of elements, referred to as particles. These particles are not point masses, but have a spatial dimension (known as the "smoothing length", h), over which their properties are smoothed using a kernel function, W. The code used in this work has been developed and used over the last ten years starting by Guerrero et al. (2004), and later used, among others, in Lorén-Aguilar et al. (2009) and Lorén-Aguilar et al. (2010). In this work, we have updated and made the necessary changes to follow appropiately the interactions presented previously. In the following we explain the main features that characterize our SPH code.

A.1 Kernel and tree

We use the standard cubic spline kernel of Monaghan & Lattanzio (1985):

$$W(r,h) = \frac{1}{\pi h^3} \begin{cases} 1 - \frac{3}{2}q^2 + \frac{3}{4}q^3, & 0 \leq q \leq 1 \\ \frac{1}{4}(2-q)^3, & 1 \leq q < 2 \\ 0 & q \geq 2, \end{cases} \tag{A.1}$$

where $q = r/h$ and r is the distance.

The search of neighbors and the evaluation of the gravitational forces are performed using an octree (Barnes & Hut, 1986). This is a tree method which allows to directly calculate the force in the gravitational N-body problem. The computational load of this method grows only as $N \log N$. In this approximation, the gravitational force and potential for a given particle due to distant nodes is computed using quadrupole corrections. When distant particles are considered, the gravitational interactions are softened using the kernel (Hernquist & Katz, 1989).

A.2 The calculation of the density

The density of a particle i is computed using a summation over neighbouring particles j. Specifically, we use the following expression:

$$\rho_{\mathrm{sum},i}(h_i) = \sum_j m_j W(|\mathbf{r}_i - \mathbf{r}_j|, h_i), \tag{A.2}$$

where $\mathbf{r}_i$ is the possition of particle i, m_i its mass, and $\rho_{\mathrm{sum},i}$ the SPH density. To determine the smoothing length of each particle we use the iteration method of Price & Monaghan (2007) to ensure that the SPH density is consistent with the standard prescription of the smoothing length:

$$h_i = \eta \left(\frac{m_i}{\rho_i}\right)^{1/3}, \tag{A.3}$$

where $\eta \sim 1.2$ is a dimensionless parameter which specifies the size of the smoothing length in terms of the average particle spacing. To this end, the root of the equation

$$\rho_i(h_i) - \rho_{i,\mathrm{sum}}(h_i) = 0 \tag{A.4}$$

is computed using a Newton-Raphson iteration method. We also consider the effect of the gradient of the smoothing length on the SPH equations, which is given by:

$$\Omega_i = \left(1 - \frac{\partial h_i}{\partial \rho_i} \sum_j m_j \frac{\partial W_{ij}(h_i)}{\partial h_i}\right). \tag{A.5}$$

A.3 Artificial viscosity

To deal numerically with shocks, where on the macroscopic scales of a simulation the very steep gradients appear as discontinuous, artificial viscosity is usually added to the SPH equations. The SPH code employed in the simulations uses a prescription for the artificial viscosity, Π, based in Riemann-solvers (Monaghan, 1997):

$$\Pi_{ij} = -\overline{\alpha}_{ij} \frac{v_{ij}^{\mathrm{sig}}}{\overline{\rho}_{ij}} \mathbf{v}_{ij} \cdot \hat{e}_{ij} \tag{A.6}$$

where the signal velocity is taken as $v_{ij}^{\mathrm{sig}} = \overline{c}_{ij} - \min\{0, \mathbf{v}_{ij} \cdot \hat{\mathbf{e}}_{ij}\}$, $\overline{c}_{ij} = (cs_i + cs_j)/2$ is the averaged sound speed, $\overline{\rho}_{ij} = (\rho_i + \rho_j)/2$ is the average density, $\mathbf{v}_i$ is the velocity vector of particle i, $\mathbf{v}_{ij} = \mathbf{v}_i - \mathbf{v}_j$, $\hat{\mathbf{e}}_{ij} = \mathbf{r}_{ij}/|\mathbf{r}_{ij}|$ and $\mathbf{r}_{ij} = \mathbf{r}_i - \mathbf{r}_j$. $\overline{\alpha}_{ij}$ is the average of the variable viscosity parameters α_i of Morris & Monaghan (1997),

$$\frac{d\alpha_i}{dt} = -\frac{\alpha_i - \alpha^*}{\tau_i} + S_i, \tag{A.7}$$

where $\alpha^* = 0.1$, $\tau_i = \frac{h_i}{l\, cs_i}$, $l \sim 0.2$ and $S_i = \max(-\nabla\cdot\mathbf{v_i}, 0)$. Additionally, to suppress artificial viscosity forces in pure shear flows the viscosity switch of Balsara (1995) is also used:

$$f_i = \frac{|\nabla \cdot \mathbf{v}|_i}{\mid \nabla \cdot \mathbf{v} \mid_i + \mid \nabla \times \mathbf{v} \mid_i + 10^{-4} cs_i/h_i}. \tag{A.8}$$

In this way the dissipative terms are largely reduced in most parts of the fluid and are only used where they are really necessary to resolve a shock, if present.

A.4 Evolution equations

Within this approach, the SPH equations for the momentum and energy conservation read respectively

$$\begin{aligned} \frac{d\mathbf{v}_i}{dt} = & - \sum_j m_j \Big[\frac{P_i}{\rho_i^2 \Omega_i} F_{ij}(h_i) + \frac{P_j}{\rho_j^2 \Omega_j} F_{ij}(h_j) \\ & + \overline{f}_{ij} \frac{\Pi_{ij}}{2} \left(\frac{1}{\Omega_i} F_{ij}(h_i) + \frac{1}{\Omega_j} F_{ij}(h_j) \right) \Big] \mathbf{r}_{ij} - \nabla \Phi_i \end{aligned} \tag{A.9}$$

$$\frac{du_i}{dt} = \frac{1}{\Omega_i} \sum_j m_j F_{ij}(h_i) \left(\frac{P_i}{\rho_i^2} + \frac{\Pi_{ij}}{2} \overline{f}_{ij} \right) \mathbf{v}_{ij} \cdot \mathbf{r}_{ij} + \varepsilon_i \tag{A.10}$$

where we have used a function $F(r/h)$ such that the gradient of the kernel is $\nabla_i W_{ij}(h) = F_{ij}(h)\mathbf{r}_{ij}$. We also take into account the energy released by nuclear reactions ε, P is the pressure and Φ the gravitational potential. However, sometimes it is advisable to use a different formulation of the equation of energy conservation (Guerrero et al., 2004; Lorén-Aguilar et al., 2005, 2009). Accordingly, for each timestep the variation of the internal energy is computed using Eq. (A.10) and simultaneously the variation of temperature is computed using:

$$\begin{aligned} \frac{dT_i}{dt} = & \frac{1}{\Omega_i} \sum_{j=1}^{N} \frac{m_j}{C_{vi}} F_{ij}(h_i) \left(\frac{T_i}{\rho_i^2} \left[\left(\frac{\partial P}{\partial T} \right)_\rho \right]_i + \frac{\Pi_{ij}}{2} \overline{f}_{ij} \right) \\ & \mathbf{v}_{ij} \cdot \mathbf{r}_{ij} + \frac{\varepsilon_i}{C_{vi}} \end{aligned} \tag{A.11}$$

where C_v is the specific heat. In order to avoid errors made when computing the temperature from the internal energy in degenerate regions, we compare the temperatures obtained when using Eqs. (A.10) and (A.11). If the difference between this temperature and that of Eq. (A.11) is larger than 5%, we consider the temperature obtained using Eq. (A.11). Otherwise, we follow the temperature evolution of the SPH particles using Eq. (A.10). Using this prescription energy is best conserved.

Regarding the integration method, a predictor-corrector numerical scheme with variable timestep (Serna et al., 1996), which turns out to be quite accurate, is used. The sequence initiates by predicting variable values (denoted by primes) at t_{n+1} according to

$$\begin{aligned}
\mathbf{r}'_{n+1} &= \mathbf{r}_n + \mathbf{v}_n \Delta t_n + \mathbf{a}'_n (\Delta t_n)^2/2 \\
\mathbf{v}'_{n+1} &= \mathbf{v}_n + \mathbf{a}'_n \Delta t_n \\
\mathbf{u}'_{n+1} &= \mathbf{u}_n + \dot{\mathbf{u}}'_n \Delta t_n \\
\mathbf{T}'_{n+1} &= \mathbf{T}_n + \dot{\mathbf{T}}'_n \Delta t_n
\end{aligned}$$

The above predicted quantities are then used to compute $\mathbf{a}'_{n+1}$, $\dot{\mathbf{u}}'_{n+1}$ and $\dot{\mathbf{T}}'_{n+1}$ at $\mathbf{r_{n+1}}'$ using Eqs. (A.9), (A.10) and (A.11) respectively. The predicted quantities are then used to correct the positions, velocities, thermal energies and temperatures:

$$\begin{aligned}
\mathbf{r}_{n+1} &= \mathbf{r}'_{n+1} + A(\mathbf{a}'_{n+1} - \mathbf{a}'_n)(\Delta t_n)^2/2 \\
\mathbf{v}_{n+1} &= \mathbf{v}'_{n+1} + B(\mathbf{a}'_{n+1} - \mathbf{a}'_n)\Delta t_n \\
\mathbf{u}_{n+1} &= \mathbf{u}'_{n+1} + C(\dot{\mathbf{u}}'_{n+1} - \dot{\mathbf{u}}'_n)\Delta t_n \\
\mathbf{T}_{n+1} &= \mathbf{T}'_{n+1} + C(\dot{\mathbf{T}}'_{n+1} - \dot{\mathbf{T}}'_n)\Delta t_n
\end{aligned}$$

where $B = 1/2$ is required to obtain accurate velocities to second order and the values of A and C are somewhat arbitrary. We adopt $A = 1/3$ and $C = 1/2$.

A.5 Equation of state and nuclear network

In our calculations we consider 14 nuclear species. These are He, C, O, Ne, Mg, Si, S, Ar, Ca, Ti, Cr, Fe, Ni and Zn. The thermodynamical properties of matter are computed using the Helmhotz equation of state (Timmes & Swesty, 2000). This equation of state assumes planckian photons, an ideal gas of ions, and an electron-positron gas with an arbitrary relativistic and degeneracy degrees. To return the electron-positron thermodynamic quantities, interpolation in a table of the helmholtz free energy is used (Timmes & Swesty, 2000). All other derivatives are analytic (chapter 24 of Cox & Giuli (1968)). The most salient feature of this equation of state is its thermodynamical consistency.

The nuclear network adopted considers captures of α particles, and the associated back reactions (photo-disintegrations), the fusion of two carbon nuclei and two oxygen nuclei and the reaction between carbon and oxygen nuclei. All the thermonuclear reaction rates are taken from the REACLIB data base (Cyburt et al., 2010). The screening factors adopted in this work are those of Itoh et al. (1979). The nuclear energy release is computed independently of the dynamical evolution

with much shorter timesteps, assuming that the dynamical variables do not change during these time steps. An hydrostatic nuclear network is a good approximation for exothermic reactions at SPH resolutions, since otherwise the $\sim 10^{27}$ g massive particles become rapidly explosive on time-scales approaching the Courant limit. Nevertheless, when photo-disintegrations occur the temperatures and the specific heat are updated, following the procedure detailed in Raskin et al. (2010). Nuclear abundances are obtained by means of an iterative pseudo-Gaussian elimination technique based on a two-step linearization procedure (Wagoner, 1969).

A.6 Timesteps

The timesteps (Δt_n) are the same for all SPH particles. They are determined comparing the local sound velocity with the local acceleration and imposing that none of the SPH particles travels a distance larger than its corresponding smoothing length. Also the change in the internal energy is taken into account. This is done specially to limit the excessive remove of internal energy from the nuclear network when material undergoing photo-desintegration experiences a kind of abrupt phase change through a strongly endothermic reaction. Therefore, the timesteps are computed in the following way:

$$\begin{aligned} \Delta t^{n+1} &= \min_i \Delta t_i^{n+1} \\ \Delta t_i^{n+1} &= \min\left(f_h \sqrt{\frac{h_i^n}{|\mathbf{a}_i^n|}}, f_h \frac{h_i^n}{v_i^{\mathrm{sig},n}}, f_u \Delta t^n \frac{u_i^{n-1}}{u_i^n - u_i^{n-1}} \right) \end{aligned}$$

with $f_h = 0.5$ and $f_u = 0.3$. Adopting all these prescriptions, energy is conserved at the level of 1%, and angular momentum at the level of 10^{-3}% in all simulations.

A.7 Parallelization

In order to perform simulations with a large number of SPH particles the code needs to be parallized. Our code uses the Message Passage Interface (MPI) libraries, and adopts a conservative strategy for the parallization. This strategy consists of parallizing just the most computationally-expensive subroutines. These are those subroutines involving summations over the neighbouring particles, for each particle. The procedure followed to handle these computations is the next one. First the complete tree structure is calculated in all processors. Then, each processor performs the corresponding tree walk and neighbour search for just the number of particles it is responsible for. We equally distribute particles into processors in order to balance the computational work of every processor. So, for simulations with N particles ran in m processors, each processor has the list of neighbours for N/m particles. During the tree walk, also the gravitational forces and potentials are computed. The neighbour

Figure A.1: Picture of the computer cluster.

list is then used to compute the density equation, Eq. (A.2) first. After using the equation of state to compute the necessary thermodynamic variables, a data transfer is needed before computing Eqs. (A.9) and (A.10). After performing additional computations, as the nuclear network calculation, a final MPI communication before finishing the time iteration is performed, so that all processors start the next iteration with the necessary data. We conducted a set of tests to assess if this approach is efficient, and we found that large computing time savings were obtained. The current version of the code incorporates the MPI libraries together with shared memory (OpenMP) functions in order to obtain faster computations, which will allow to increase the resolution in our simulations.

A.8 Computer cluster

The SPH simulations described in this work were done in a computer cluster built by ourselves. We started its construction in 2 011 and since then it has been continously upgraded, becoming an essential tool for performing our calculations. Figure A.1 shows a recent image of the computer cluster, named `atria`.

The cluster is composed of 55 computers with Intel Sandy Bridge processors with velocities of 3.1 GHz and 4 Gb of RAM. The computers are linked with Gigabite switches that ensure fast enough communications, an essential feature for parallel computations. We have installed a Linux operating system in all the nodes. A

master node has been defined to which external connection is possible. Moreover, the master node makes a virtual copy of the users home to every node through NFS in order to make the information accessible from every of them. Since, fortunately, the number of users of the cluster is limited, at most two people running processes at the same time, we have not installed any quee system to prioritize the jobs yet. Nevertheless, we judge that possibly in the future installing such a system will be necessary. The number of computers, however, is sufficiently large to dissipate a considerable amount of heat, thus increasing the temperature of the cluster room. At high temperatures computers run slower and some warning messages are issued. All this required studying the most appropriate position of the air conditioning unit in order to generate an efficient air flow, allowing to cool efficiently the front part of the nodes. Doing so, we managed to keep all the magines within the temperature margins recommended in the manual.

Bibliography

Abbasi, R., Abdou, Y., Abu-Zayyad, T., Ackermann, M., Adams, J., Aguilar, J. A., Ahlers, M., Allen, M. M., Altmann, D., Andeen, K. & et al., 2011. IceCube sensitivity for low-energy neutrinos from nearby supernovae. *A&A*, **535**, A109.

Ahrens, J., Bai, X., Barouch, G., Barwick, S. W., Bay, R. C. et al., 2002. Search for supernova neutrino bursts with the AMANDA detector. *Astroparticle Physics*, **16**, 345–359.

Alpar, M. A., 2001. On Young Neutron Stars as Propellers and Accretors with Conventional Magnetic Fields. *ApJ*, **554**, 1245–1254.

Althaus, L. G., Córsico, A. H., Isern, J. & García-Berro, E., 2010. Evolutionary and pulsational properties of white dwarf stars. *A&A Rev.*, **18**, 471–566.

Amaro-Seoane, P., Aoudia, S., Babak, S., Binétruy, P., Berti, E. et al., 2013. eLISA: Astrophysics and cosmology in the millihertz regime. *GW Notes, Vol. 6, p. 4-110*, **6**, 4–110.

Angel, J. R. P., Borra, E. F. & Landstreet, J. D., 1981. The magnetic fields of white dwarfs. *ApJS*, **45**, 457–474.

Armitage, P. J. & Clarke, C. J., 1996. Magnetic braking of T Tauri stars. *MNRAS*, **280**, 458–468.

Arnett, W. D., 1979. On the theory of Type I supernovae. *ApJ*, **230**, L37–L40.

Arnett, W. D., 1982. Type I supernovae. I - Analytic solutions for the early part of the light curve. *ApJ*, **253**, 785–797.

Artymowicz, P., Clarke, C. J., Lubow, S. H. & Pringle, J. E., 1991. The effect of an external disk on the orbital elements of a central binary. *ApJ*, **370**, L35–L38.

Aznar Cuadrado, R., Jordan, S., Napiwotzki, R., Schmid, H. M., Solanki, S. K. & Mathys, G., 2004. Discovery of kilogauss magnetic fields in three DA white dwarfs. *A&A*, **423**, 1081–1094.

Aznar-Siguán, G., García-Berro, E., Magnien, M. & Lorén-Aguilar, P., 2014. On the possible observational signatures of white dwarf dynamical interactions. *MNRAS*, **443**, 2372–2383.

Badenes, C. & Maoz, D., 2012. The Merger Rate of Binary White Dwarfs in the Galactic Disk. *ApJ*, **749**, L11.

Balsara, D. S., 1995. von Neumann stability analysis of smooth particle hydrodynamics–suggestions for optimal algorithms. *J. Comp. Phys.*, **121**, 357–372.

Barnes, J. & Hut, P., 1986. A Hierarchical O(NlogN) Force-Calculation Algorithm. *Nature*, **324**, 446–449.

Benacquista, M., Sedrakian, D. M., Hairapetyan, M. V., Shahabasyan, K. M. & Sadoyan, A. A., 2003. Gravitational Radiation from Pulsating White Dwarfs. *ApJ*, **596**, L223–L226.

Benz, W., Cameron, A. G. W., Press, W. H. & Bowers, R. L., 1990. Dynamic mass exchange in doubly degenerate binaries. I - 0.9 and 1.2 solar mass stars. *ApJ*, **348**, 647–667.

Benz, W., Thielemann, F.-K. & Hills, J. G., 1989. Three-dimensional hydrodynamical simulations of stellar collisions. II - White dwarfs. *ApJ*, **342**, 986–998.

Berger, L., Koester, D., Napiwotzki, R., Reid, I. N. & Zuckerman, B., 2005. Rotation velocities of white dwarfs determined from the Ca II K line. *A&A*, **444**, 565–571.

Blackman, E. G., Frank, A., Markiel, J. A., Thomas, J. H. & Van Horn, H. M., 2001. Dynamos in asymptotic-giant-branch stars as the origin of magnetic fields shaping planetary nebulae. *Nature*, **409**, 485–487.

Bogomazov, A. I. & Tutukov, A. V., 2009. Merging of components in close binaries: Type Ia supernovae, massive white dwarfs, and Ap stars. *Astronomy Reports*, **53**, 214–222.

Boshkayev, K., Izzo, L., Rueda Hernandez, J. A. & Ruffini, R., 2013a. SGR 0418+5729, Swift J1822.3-1606, and 1E 2259+586 as massive, fast-rotating, highly magnetized white dwarfs. *A&A*, **555**, A151.

Boshkayev, K., Rueda, J. A., Ruffini, R. & Siutsou, I., 2013b. On General Relativistic Uniformly Rotating White Dwarfs. *ApJ*, **762**, 117.

Braithwaite, J., 2009. Axisymmetric magnetic fields in stars: relative strengths of poloidal and toroidal components. *MNRAS*, **397**, 763–774.

Branch, D., 1992. The Hubble constant from nickel radioactivity in type IA supernovae. *ApJ*, **392**, 35–40.

Briggs, G. P., Ferrario, L., Tout, C. A., Wickramasinghe, D. T. & Hurley, J. R., 2015. MNRAS, in press.

Cannizzo, J. K., Lee, H. M. & Goodman, J., 1990. The disk accretion of a tidally disrupted star onto a massive black hole. *ApJ*, **351**, 38–46.

Cardelli, J. A., Clayton, G. C. & Mathis, J. S., 1989. The relationship between infrared, optical, and ultraviolet extinction. *ApJ*, **345**, 245–256.

Cassisi, S., Potekhin, A. Y., Pietrinferni, A., Catelan, M. & Salaris, M., 2007. Updated Electron-Conduction Opacities: The Impact on Low-Mass Stellar Models. *ApJ*, **661**, 1094–1104.

Chapman, N. L., Mundy, L. G., Lai, S.-P. & Evans, I. N. J., 2009. The Mid-Infrared Extinction Law in the Ophiuchus, Perseus, and Serpens Molecular Clouds. *ApJ*, **690**, 496–511.

Charpinet, S., Fontaine, G. & Brassard, P., 2009. Seismic evidence for the loss of stellar angular momentum before the white-dwarf stage. *Nature*, **461**, 501–503.

Chatterjee, P., Hernquist, L. & Narayan, R., 2000. An Accretion Model for Anomalous X-Ray Pulsars. *ApJ*, **534**, 373–379.

Chiang, E. I. & Goldreich, P., 1997. Spectral Energy Distributions of T Tauri Stars with Passive Circumstellar Disks. *ApJ*, **490**, 368.

Clayton, G. C., Geballe, T. R., Herwig, F., Fryer, C. & Asplund, M., 2007. Very Large Excesses of ^{18}O in Hydrogen-deficient Carbon and R Coronae Borealis Stars: Evidence for White Dwarf Mergers. *ApJ*, **662**, 1220–1230.

Colgate, S. A., 1967. Stellar Coalescence and the Multiple Supernova Interpretation of Quasi-Stellar Sources. *ApJ*, **150**, 163.

Colgate, S. A. & McKee, C., 1969. Early Supernova Luminosity. *ApJ*, **157**, 623.

Cox, J. & Giuli, R., 1968. *Principles of Stellar Structure: Physical principles*. No. v. 1 in Principles of Stellar Structure. Gordon and Breach. URL `https://books.google.es/books?id=TdhEAAAAIAAJ`.

Crowder, J. & Cornish, N. J., 2005. Beyond LISA: Exploring future gravitational wave missions. *Phys. Rev. D*, **72**(8), 083005.

Cyburt, R. H., Amthor, A. M., Ferguson, R., Meisel, Z., Smith, K., Warren, S., Heger, A., Hoffman, R. D., Rauscher, T., Sakharuk, A., Schatz, H., Thielemann, F. K. & Wiescher, M., 2010. The JINA REACLIB Database: Its Recent Updates and Impact on Type-I X-ray Bursts. *ApJS*, **189**, 240–252.

Dan, M., Rosswog, S., Brüggen, M. & Podsiadlowski, P., 2014. The structure and fate of white dwarf merger remnants. *MNRAS*, **438**, 14–34.

Dan, M., Rosswog, S., Guillochon, J. & Ramirez-Ruiz, E., 2011. Prelude to A Double Degenerate Merger: The Onset of Mass Transfer and Its Impact on Gravitational Waves and Surface Detonations. *ApJ*, **737**, 89.

Dan, M., Rosswog, S., Guillochon, J. & Ramirez-Ruiz, E., 2012. How the merger of two white dwarfs depends on their mass ratio: orbital stability and detonations at contact. *MNRAS*, **422**, 2417–2428.

Dautray, R. & L., L. J., 2000. *Mathematical Analysis and Numerical Methods for Science and Technology*. Springer Verlag. (vol. 6).

Davies, M., 2002. The astrophysics of crowded places. *Roy. Soc. of London Phil. Trans. Series A*, **360**, 2773–2786.

De Marco, O., Passy, J.-C., Moe, M., Herwig, F., Mac Low, M.-M. & Paxton, B., 2011. On the α formalism for the common envelope interaction. *MNRAS*, **411**, 2277–2292.

Dewi, J. D. M. & Tauris, T. M., 2000. On the energy equation and efficiency parameter of the common envelope evolution. *A&A*, **360**, 1043–1051.

Dhillon, V. S., Marsh, T. R., Hulleman, F., van Kerkwijk, M. H., Shearer, A., Littlefair, S. P., Gavriil, F. P. & Kaspi, V. M., 2005. High-speed, multicolour optical photometry of the anomalous X-ray pulsar 4U 0142+61 with ULTRACAM. *MNRAS*, **363**, 609–614.

Duncan, R. C. & Thompson, C., 1992. Formation of very strongly magnetized neutron stars - Implications for gamma-ray bursts. *ApJ*, **392**, L9–L13.

Dupuis, J., Chayer, P., Vennes, S., Allard, N. F. & Hébrard, G., 2003. Far Ultraviolet Spectroscopic Explorer Observation of the Ultramassive White Dwarf PG 1658+441. *ApJ*, **598**, 486–491.

Durant, M. & van Kerkwijk, M. H., 2006a. Distances to Anomalous X-Ray Pulsars Using Red Clump Stars. *ApJ*, **650**, 1070–1081.

Durant, M. & van Kerkwijk, M. H., 2006b. Extinction Columns and Intrinsic X-Ray Spectra of the Anomalous X-Ray Pulsars. *ApJ*, **650**, 1082–1090.

Durant, M. & van Kerkwijk, M. H., 2006c. Multiwavelength Variability of the Magnetar 4U 0142+61. *ApJ*, **652**, 576–583.

Eggleton, P. P., 1983. Approximations to the radii of Roche lobes. *ApJ*, **268**, 368.

Ertan, Ü., Ekşi, K. Y., Erkut, M. H. & Alpar, M. A., 2009. On the Evolution of Anomalous X-ray Pulsars and Soft Gamma-ray Repeaters with Fall Back Disks. *ApJ*, **702**, 1309–1320.

Euchner, F., Jordan, S., Beuermann, K., Reinsch, K. & Gänsicke, B. T., 2006. Zeeman tomography of magnetic white dwarfs. III. The 70-80 Megagauss magnetic field of PG 1015+014. *A&A*, **451**, 671–681.

Euchner, F., Reinsch, K., Jordan, S., Beuermann, K. & Gänsicke, B. T., 2005. Zeeman tomography of magnetic white dwarfs. II. The quadrupole-dominated magnetic field of HE 1045-0908. *A&A*, **442**, 651–660.

Fabian, A. C., Pringle, J. E. & Rees, M. J., 1975. Tidal capture formation of binary systems and X-ray sources in globular clusters. *MNRAS*, **172**, 15P.

Farihi, J., Dufour, P., Napiwotzki, R. & Koester, D., 2011. The magnetic and metallic degenerate G77-50. *MNRAS*, **413**, 2559–2569.

Ferrari, A. & Ruffini, R., 1969. Theoretical Implications of the Second Time Derivative of the Period of the Pulsar NP 0532. *ApJ*, **158**, L71+.

Ferrario, L., Vennes, S., Wickramasinghe, D. T., Bailey, J. A. & Christian, D. J., 1997. EUVE J0317-855 A rapidly rotating, high-field magnetic white dwarf. *MNRAS*, **292**, 205.

Fink, M., Hillebrandt, W. & Röpke, F. K., 2007. Double-detonation supernovae of sub-Chandrasekhar mass white dwarfs. *A&A*, **476**, 1133–1143.

García-Berro, E., Lorén-Aguilar, P., Aznar-Siguán, G., Torres, S., Camacho, J., Althaus, L. G., Córsico, A. H., Külebi, B. & Isern, J., 2012. Double Degenerate Mergers as Progenitors of High-field Magnetic White Dwarfs. *ApJ*, **749**, 25.

García-Berro, E., Lorén-Aguilar, P., Pedemonte, A. G., Isern, J., Bergeron, P., Dufour, P. & Brassard, P., 2007. Evidence of a Merger of Binary White Dwarfs: The Case of GD 362. *ApJ*, **661**, L179–L182.

García-Berro, E., Torres, S., Isern, J. & Burkert, A., 1999. Monte Carlo simulations of the disc white dwarf population. *MNRAS*, **302**, 173–188.

García-Berro, E., Torres, S., Isern, J. & Burkert, A., 2004. Monte Carlo simulations of the halo white dwarf population. *A&A*, **418**, 53–65.

Giacomazzo, B., Rezzolla, L. & Baiotti, L., 2011. Accurate evolutions of inspiralling and magnetized neutron stars: Equal-mass binaries. *Phys. Rev. D*, **83**(4), 044014.

Gingold, R. A. & Monaghan, J. J., 1977. Smoothed particle hydrodynamics - Theory and application to non-spherical stars. *MNRAS*, **181**, 375–389.

Göhler, E., Wilms, J. & Staubert, R., 2005. XMM-Newton observation of the anomalous X-ray pulsar 4U 0142+61. *A&A*, **433**, 1079–1083.

Grindlay, J., Gursky, H., Schnopper, H., Parsignault, D. R., Heise, J., Brinkman, A. C. & Schrijver, J., 1976. Discovery of intense X-ray bursts from the globular cluster NGC 6624. *ApJ*, **205**, L127–L130.

Guerrero, J., García-Berro, E. & Isern, J., 2004. Smoothed Particle Hydrodynamics simulations of merging white dwarfs. *A&A*, **413**, 257–272.

Hamuy, M., Phillips, M. M., Suntzeff, N. B., Schommer, R. A., Maza, J., Smith, R. C., Lira, P. & Aviles, R., 1996. The Morphology of Type IA Supernovae Light Curves. *AJ*, **112**, 2438.

Han, Z. & Podsiadlowski, P., 2004. The single-degenerate channel for the progenitors of Type Ia supernovae. *MNRAS*, **350**, 1301–1309.

Hawley, W. P., Athanassiadou, T. & Timmes, F. X., 2012. Zero Impact Parameter White Dwarf Collisions in FLASH. *ApJ*, **759**, 39.

Heggie, D. C., 1975. Binary evolution in stellar dynamics. *MNRAS*, **173**, 729–787.

Hernquist, L. & Katz, N., 1989. TREESPH – A unification of SPH with the hierarchical tree method. *ApJS*, **70**, 419–446.

Hillebrandt, W., Kromer, M., Röpke, F. K. & Ruiter, A. J., 2013. Towards an understanding of Type Ia supernovae from a synthesis of theory and observations. *Frontiers of Physics*, **8**, 116–143.

Hills, J. G. & Day, C. A., 1976. Stellar Collisions in Globular Clusters. *ApJ*, **17**, 87.

Holberg, J. B., Sion, E. M., Oswalt, T., McCook, G. P., Foran, S. & Subasavage, J. P., 2008. A New Look at the Local White Dwarf Population. *AJ*, **135**, 1225–1238.

Holmberg, J. & Flynn, C., 2000. The local density of matter mapped by Hipparcos. *MNRAS*, **313**, 209–216.

Hulleman, F., van Kerkwijk, M. H. & Kulkarni, S. R., 2000. An optical counterpart to the anomalous X-ray pulsar 4U0142+61. *Nature*, **408**, 689–692.

Hulleman, F., van Kerkwijk, M. H. & Kulkarni, S. R., 2004. The Anomalous X-ray Pulsar 4U 0142+61: Variability in the infrared and a spectral break in the optical. *A&A*, **416**, 1037–1045.

Hurley, J. R., Pols, O. R. & Tout, C. A., 2000. Comprehensive analytic formulae for stellar evolution as a function of mass and metallicity. *MNRAS*, **315**, 543–569.

Hurley, J. R. & Shara, M. M., 2003. White Dwarf Sequences in Dense Star Clusters. *ApJ*, **589**, 179–198.

Hurley, J. R., Tout, C. A. & Pols, O. R., 2002. Evolution of binary stars and the effect of tides on binary populations. *MNRAS*, **329**, 897–928.

Iben, J. I. & Tutukov, A. V., 1984. Supernovae of type I as end products of the evolution of binaries with components of moderate initial mass (M not greater than about 9 solar masses). *ApJS*, **54**, 335–372.

Ilkov, M. & Soker, N., 2012. Type Ia supernovae from very long delayed explosion of core-white dwarf merger. *MNRAS*, **419**, 1695–1700.

Ilkov, M. & Soker, N., 2013. The number of progenitors in the core-degenerate scenario for Type Ia supernovae. *MNRAS*, **428**, 579–586.

Itoh, N., Hayashi, H., Nishikawa, A. & Kohyama, Y., 1996. Neutrino Energy Loss in Stellar Interiors. VII. Pair, Photo-, Plasma, Bremsstrahlung, and Recombination Neutrino Processes. *ApJS*, **102**, 411.

Itoh, N., Totsuji, H., Ichimaru, S. & Dewitt, H. E., 1979. Enhancement of thermonuclear reaction rate due to strong screening. II - Ionic mixtures. *ApJ*, **234**, 1079–1084.

Izzard, R. G., Jeffery, C. S. & Lattanzio, J., 2007. Origin of the early-type R stars: a binary-merger solution to a century-old problem? *A&A*, **470**, 661–673.

Jackson, J. D., 1998. *Classical Electrodynamics, 3rd Edition*. John Wiley and Sons-VCH.

Kashi, A. & Soker, N., 2011. A circumbinary disc in the final stages of common envelope and the core-degenerate scenario for Type Ia supernovae. *MNRAS*, **417**, 1466–1479.

Katz, B. & Dong, S., 2012. The rate of WD-WD head-on collisions may be as high as the SNe Ia rate. *ArXiv e-prints*.

Kawka, A. & Vennes, S., 2011. The cool magnetic DAZ white dwarf NLTT 10480. *A&A*, **532**, A7.

Kawka, A., Vennes, S., Schmidt, G. D., Wickramasinghe, D. T. & Koch, R., 2007. Spectropolarimetric Survey of Hydrogen-rich White Dwarf Stars. *ApJ*, **654**, 499–520.

Kemp, J. C., Swedlund, J. B., Landstreet, J. D. & Angel, J. R. P., 1970. Discovery of Circularly Polarized Light from a White Dwarf. *ApJ*, **161**, L77.

Kern, B. & Martin, C., 2002. Optical pulsations from the anomalous X-ray pulsar 4U0142+61. *Nature*, **417**, 527–529.

King, A. R., Pringle, J. E. & Wickramasinghe, D. T., 2001. Type Ia supernovae and remnant neutron stars. *MNRAS*, **320**, L45–L48.

Kleinman, S. J., Kepler, S. O., Koester, D., Pelisoli, I., Peçanha, V., Nitta, A., Costa, J. E. S., Krzesinski, J., Dufour, P., Lachapelle, F.-R., Bergeron, P., Yip, C.-W., Harris, H. C., Eisenstein, D. J., Althaus, L. & Córsico, A., 2013. SDSS DR7 White Dwarf Catalog. *ApJS*, **204**, 5.

Kozai, Y., 1962. Secular perturbations of asteroids with high inclination and eccentricity. *AJ*, **67**, 591.

Kroupa, P., Tout, C. A. & Gilmore, G., 1993. The distribution of low-mass stars in the Galactic disc. *MNRAS*, **262**, 545–587.

Kudritzki, R. P. & Reimers, D., 1978. . *A&A*, **70**, 227.

Kuiper, G. P., 1934. Two new white dwarfs of large parallax. *Pub. Ast. Soc. Pacific*, **46**(287).

Külebi, B., Ekşi, K. Y., Lorén-Aguilar, P., Isern, J. & García-Berro, E., 2013. Magnetic white dwarfs with debris discs. *MNRAS*, **431**, 2778–2788.

Külebi, B., Jordan, S., Euchner, F., Gänsicke, B. T. & Hirsch, H., 2009. Analysis of hydrogen-rich magnetic white dwarfs detected in the Sloan Digital Sky Survey. *A&A*, **506**, 1341–1350.

Külebi, B., Jordan, S., Nelan, E., Bastian, U. & Altmann, M., 2010. Constraints on the origin of the massive, hot, and rapidly rotating magnetic white dwarf RE J 0317-853 from an HST parallax measurement. *A&A*, **524**, A36.

Kunugise, T. & Iwamoto, K., 2007. Neutrino Emission from Type Ia Supernovae. *PASJ*, **59**, L57.

Kushnir, D., Katz, B., Dong, S., Livne, E. & Fernández, R., 2013. Head-on Collisions of White Dwarfs in Triple Systems Could Explain Type Ia Supernovae. *ApJ*, **778**, L37.

Lamb, F. K., Pethick, C. J. & Pines, D., 1973. A Model for Compact X-Ray Sources: Accretion by Rotating Magnetic Stars. *ApJ*, **184**, 271–290.

Lee, H. M. & Ostriker, J. P., 1986. Cross sections for tidal capture binary formation and stellar merger. *ApJ*, **310**, 176–188.

Leibundgut, B., 2000. Type Ia Supernovae. *A&A Rev.*, **10**, 179–209.

Leloudas, G., Stritzinger, M. D., Sollerman, J., Burns, C. R., Kozma, C. et al., 2009. The normal Type Ia SN 2003hv out to very late phases. *A&A*, **505**, 265–279.

Levanon, N., Soker, N. & García-Berro, E., 2015. MNRAS, in press.

Lira, P., Suntzeff, N. B., Phillips, M. M., Hamuy, M., Maza, J. et al., 1998. Optical light curves of the Type IA supernovae SN 1990N and 1991T. *AJ*, **115**, 234.

Livio, M. & Riess, A. G., 2003. Have the Elusive Progenitors of Type Ia Supernovae Been Discovered? *ApJ*, **594**, L93–L94.

Livne, E., 1990. Successive detonations in accreting white dwarfs as an alternative mechanism for type I supernovae. *ApJ*, **354**, L53–L55.

Longland, R., Lorén-Aguilar, P., José, J., García-Berro, E., Althaus, L. G. & Isern, J., 2011. Nucleosynthesis during the Merger of White Dwarfs and the Origin of R Coronae Borealis Stars. *ApJ*, **737**, L34.

Lorén-Aguilar, P., Guerrero, J., Isern, J., Lobo, J. A. & García-Berro, E., 2005. Gravitational wave radiation from the coalescence of white dwarfs. *MNRAS*, **356**, 627–636.

Lorén-Aguilar, P., Isern, J. & García-Berro, E., 2009. High-resolution smoothed particle hydrodynamics simulations of the merger of binary white dwarfs. *A&A*, **500**, 1193–1205.

Lorén-Aguilar, P., Isern, J. & García-Berro, E., 2010. Smoothed particle hydrodynamics simulations of white dwarf collisions and close encounters. *MNRAS*, **406**, 2749–2763.

Lucy, L. B., 1977. A numerical approach to the testing of the fission hypothesis. *AJ*, **82**, 1013–1024.

Malheiro, M., Rueda, J. A. & Ruffini, R., 2012. SGRs and AXPs as Rotation-Powered Massive White Dwarfs. *Publications of the Astronomical Society of Japan*, **64**, 56.

Malov, I. F., 2010. The drift model for AXPs and SGRs in the light of new observtional data. *Astronomy Reports*, **54**, 925–931.

Maoz, D., Mannucci, F. & Nelemans, G., 2014. Observational Clues to the Progenitors of Type Ia Supernovae. *ARA&A*, **52**, 107–170.

Marsden, D., Lingenfelter, R. E., Rothschild, R. E. & Higdon, J. C., 2001. Nature versus Nurture: The Origin of Soft Gamma-Ray Repeaters and Anomalous X-Ray Pulsars. *ApJ*, **550**, 397–409.

Mathys, G., Solanki, S. K. & Wickramasinghe, D. T., eds., 2001. *Magnetic Fields Across the Hertzsprung-Russell Diagram*, vol. 248 of *Astronomical Society of the Pacific Conference Series*.

Matt, S. P., Pinzón, G., Greene, T. P. & Pudritz, R. E., 2012. Spin Evolution of Accreting Young Stars. II. Effect of Accretion-powered Stellar Winds. *ApJ*, **745**, 101.

Mereghetti, S., 2008. The strongest cosmic magnets: soft gamma-ray repeaters and anomalous X-ray pulsars. *A&A Rev.*, **15**, 225–287.

Mestel, L., 1952. On the theory of white dwarf stars. I. The energy sources of white dwarfs. *MNRAS*, **112**, 583.

Minkowski, R., 1938. Mount Wilson Observatory Annual Report. *Ann. Rep. Dir. Mt. Wilson Obs.*, **28**, 38.

Misner, C. W., Thorne, K. S. & Wheeler, J. A., 1973. *Gravitation*. W.H. Freeman and Co.

Moll, R., Raskin, C., Kasen, D. & Woosley, S. E., 2014. Type Ia Supernovae from Merging White Dwarfs. I. Prompt Detonations. *ApJ*, **785**, 105.

Monaghan, J. J., 1997. SPH and Riemann Solvers. *J. Comp. Phys.*, **136**, 298–307.

Monaghan, J. J. & Lattanzio, J. C., 1985. A refined particle method for astrophysical problems. *A&A*, **149**, 135–143.

Morii, M., Kawai, N., Kataoka, J., Yatsu, Y., Kobayashi, N. & Terada, H., 2005. Near-infrared, optical, and X-ray observations of the anomalous X-ray pulsar 4U 0142 + 61. *Advances in Space Research*, **35**, 1177–1180.

Morii, M., Kobayashi, N., Kawai, N., Terada, H., Tanaka, Y. T., Kitamoto, S. & Shibazaki, N., 2009. Search for Near-Infrared Pulsation of the Anomalous X-Ray Pulsar 4U 0142+61. *PASJ*, **61**, 51–.

Morini, M., Robba, N. R., Smith, A. & van der Klis, M., 1988. EXOSAT observations of the supernova remnant G109.1-1.0 and the X-ray pulsar 1E 2259+586. *ApJ*, **333**, 777–787.

Morris, J. P. & Monaghan, J. J., 1997. A Switch to Reduce SPH Viscosity. *Journal of Computational Physics*, **136**, 41–50.

Nakahata, M., Fukuda, Y., Hayakawa, T., Ichihara, E., Inoue, K. et al., 1999. Calibration of Super-Kamiokande using an electron LINAC. The Super-Kamiokande Collaboration. *Nuclear Instruments and Methods in Physics Research A*, **421**, 113–129.

Należyty, M. & Madej, J., 2004. A catalogue of isolated massive white dwarfs. Mass distribution of massive star. *A&A*, **420**, 507–513.

Nelemans, G., Yungelson, L. R., Portegies Zwart, S. F. & Verbunt, F., 2001. Population synthesis for double white dwarfs . I. Close detached systems. *A&A*, **365**, 491–507.

Nomoto, K., 1982. Accreting white dwarf models for type I supernovae. I - Presupernova evolution and triggering mechanisms. *ApJ*, **253**, 798–810.

Nordhaus, J., Wellons, S., Spiegel, D. S., Metzger, B. D. & Blackman, E. G., 2011. Formation of high-field magnetic white dwarfs from common envelopes. *Proceedings of the National Academy of Science*, **108**, 3135–3140.

Odrzywolek, A. & Plewa, T., 2011. Probing thermonuclear supernova explosions with neutrinos. *A&A*, **529**, A156.

Paczynski, B., 1990. X-ray pulsar 1E 2259 + 586 - A merged white dwarf with a 7 second rotation period? *ApJ*, **365**, L9–L12.

Pakmor, R., Hachinger, S., Röpke, F. K. & Hillebrandt, W., 2011. Violent mergers of nearly equal-mass white dwarf as progenitors of subluminous Type Ia supernovae. *A&A*, **528**, A117.

Pakmor, R., Kromer, M., Röpke, F. K., Sim, S. A., Ruiter, A. J. & Hillebrandt, W., 2010. Sub-luminous type Ia supernovae from the mergers of equal-mass white dwarfs with mass ˜0.9M_*solar*. *Nature*, **463**, 61–64.

Pakmor, R., Kromer, M., Taubenberger, S., Sim, S. A., Röpke, F. K. & Hillebrandt, W., 2012. Normal Type Ia Supernovae from Violent Mergers of White Dwarf Binaries. *ApJ*, **747**, L10.

Patel, S. K., Kouveliotou, C., Woods, P. M., Tennant, A. F., Weisskopf, M. C., Finger, M. H., Wilson, C. A., Göğüş, E., van der Klis, M. & Belloni, T., 2003. Chandra Observations of the Anomalous X-Ray Pulsar 4U 0142+61. *ApJ*, **587**, 367–372.

Piersanti, L., Tornambé, A. & Yungelson, L. R., 2014. He-accreting white dwarfs: accretion regimes and final outcomes. *MNRAS*, **445**, 3239–3262.

Potter, A. T. & Tout, C. A., 2010. Magnetic field evolution of white dwarfs in strongly interacting binary star systems. *MNRAS*, **402**, 1072–1080.

Press, W. H. & Teukolsky, S. A., 1977. On formation of close binaries by two-body tidal capture. *ApJ*, **213**, 183–192.

Price, D. J., 2007. splash: An Interactive Visualisation Tool for Smoothed Particle Hydrodynamics Simulations. *PASA*, **24**, 159–173.

Price, D. J. & Monaghan, J. J., 2007. An energy-conserving formalism for adaptive gravitational force softening in smoothed particle hydrodynamics and N-body codes. *MNRAS*, **374**, 1347–1358.

Raskin, C., Kasen, D., Moll, R., Schwab, J. & Woosley, S., 2013. Type Ia Supernovae from Merging White Dwarfs II) Post-Merger Detonations. *ArXiv e-prints*.

Raskin, C., Scannapieco, E., Rockefeller, G., Fryer, C., Diehl, S. & Timmes, F., 2010. Ni Production in Double Degenerate White Dwarf Collisions^{56}. *ApJ*, **724**, 111.

Raskin, C., Timmes, F. X., Scannapieco, E., Diehl, S. & Fryer, C., 2009. On Type Ia supernovae from the collisions of two white dwarfs. *MNRAS*, **399**, L156–L159.

Reimers, D., Jordan, S. & Christlieb, N., 2004. HE0241-0155 - Evidence for a large scale homogeneous field in a highly magnetic white dwarf. *A&A*, **414**, 1105–1108.

Renedo, I., Althaus, L. G., Miller Bertolami, M. M., Romero, A. D., Córsico, A. H., Rohrmann, R. D. & García-Berro, E., 2010. New Cooling Sequences for Old White Dwarfs. *ApJ*, **717**, 183–195.

Rosswog, S., 2007. Fallback accretion in the aftermath of a compact binary merger. *MNRAS*, **376**, L48–L51.

Rosswog, S., Kasen, D., Guillochon, J. & Ramirez-Ruiz, E., 2009. Collisions of white dwarfs as a new progenitor channel for type Ia supernovae. *ApJ*, **705**, L128.

Rosswog, S., Piran, T. & Nakar, E., 2013. The multimessenger picture of compact object encounters: binary mergers versus dynamical collisions. *MNRAS*, **430**, 2585–2604.

Rueda, J. A. & Ruffini, R., 2012. On the Induced Gravitational Collapse of a Neutron Star to a Black Hole by a Type Ib/c Supernova. *ApJ*, **758**, L7.

Ruiter, A. J., Belczynski, K., Sim, S. A., Hillebrandt, W., Fryer, C. L., Fink, M. & Kromer, M., 2011. Delay times and rates for Type Ia supernovae and thermonuclear explosions from double-detonation sub-Chandrasekhar mass models. *MNRAS*, **417**, 408–419.

Saio, H. & Nomoto, K., 1985. Evolution of a merging pair of C + O white dwarfs to form a single neutron star. *A&A*, **150**, L21–L23.

Saio, H. & Nomoto, K., 2004. Off-Center Carbon Ignition in Rapidly Rotating, Accreting Carbon-Oxygen White Dwarfs. *ApJ*, **615**, 444–449.

Sandquist, E. L., Taam, R. E., Chen, X., Bodenheimer, P. & Burkert, A., 1998. Double Core Evolution. X. Through the Envelope Ejection Phase. *ApJ*, **500**, 909–922.

Schmidt, G. D., Bergeron, P., Liebert, J. & Saffer, R. A., 1992. Two ultramassive white dwarfs found among candidates for magnetic fields. *ApJ*, **394**, 603–608.

Schmidt, G. D., Harris, H. C., Liebert, J., Eisenstein, D. J., Anderson, S. F. et al., 2003. Magnetic White Dwarfs from the Sloan Digital Sky Survey: The First Data Release. *ApJ*, **595**, 1101–1113.

Schmidt, G. D., West, S. C., Liebert, J., Green, R. F. & Stockman, H. S., 1986. The new magnetic white dwarf PG 1031 + 234 - Polarization and field structure at more than 500 milion Gauss. *ApJ*, **309**, 218–229.

Schreiber, M. R. & Gänsicke, B. T., 2003. The age, life expectancy, and space density of Post Common Envelope Binaries. *A&A*, **406**, 305–321.

Schwab, J., Shen, K. J., Quataert, E., Dan, M. & Rosswog, S., 2012. The viscous evolution of white dwarf merger remnants. *MNRAS*, **427**, 190–203.

Segretain, L., Chabrier, G. & Mochkovitch, R., 1997. The Fate of Merging White Dwarfs. *ApJ*, **481**, 355–362.

Seitenzahl, I. R., Meakin, C. A., Townsley, D. M., Lamb, D. Q. & Truran, J. W., 2009. Spontaneous Initiation of Detonations in White Dwarf Environments: Determination of Critical Sizes. *ApJ*, **696**, 515–527.

Serna, A., Alimi, J.-M. & Chieze, J.-P., 1996. Adaptive Smooth Particle Hydrodynamics and Particle-Particle Coupled Codes: Energy and Entropy Conservation. *ApJ*, **461**, 884.

Shara, M. M. & Hurley, J. R., 2002. Star Clusters as Type Ia Supernova Factories. *ApJ*, **571**, 830–842.

Shara, M. M. & Regev, O., 1986. Hydrodynamic simulation of a white dwarf-main-sequence star collision in a globular cluster core. *ApJ*, **306**, 543–551.

Shara, M. M. & Shaviv, G., 1977. White dwarf - main sequence star collisions. *MNRAS*, **179**, 705–718.

Shen, K. J. & Bildsten, L., 2009. Unstable Helium Shell Burning on Accreting White Dwarfs. *ApJ*, **699**, 1365–1373.

Silvestri, N. M., Lemagie, M. P., Hawley, S. L., West, A. A., Schmidt, G. D., Liebert, J., Szkody, P., Mannikko, L., Wolfe, M. A., Barentine, J. C., Brewington, H. J., Harvanek, M., Krzesinski, J., Long, D., Schneider, D. P. & Snedden, S. A., 2007. New Close Binary Systems from the SDSS-I (Data Release Five) and the Search for Magnetic White Dwarfs in Cataclysmic Variable Progenitor Systems. *AJ*, **134**, 741–748.

Soker, N., Kashi, A., García-Berro, E., Torres, S. & Camacho, J., 2013. Explaining the Type Ia supernova PTF 11kx with a violent prompt merger scenario. *MNRAS*, **431**, 1541–1546.

Soker, N., Regev, O., Livio, M. & Shara, M. M., 1987. Massive disk formation resulting from the collision of a main-sequence star with a white dwarf in a globular cluster core. *ApJ*, **318**, 760–766.

Sparks, W. M. & Stecher, T. P., 1974. Supernova: The Result of the Death Spiral of a White Dwarf into a Red Giant. *ApJ*, **188**, 149.

Spitkovsky, A., 2006. Time-dependent Force-free Pulsar Magnetospheres: Axisymmetric and Oblique Rotators. *ApJ*, **648**, L51–L54.

Tayler, R. J., 1973. The adiabatic stability of stars containing magnetic fields-I.Toroidal fields. *MNRAS*, **161**, 365.

Thompson, C. & Duncan, R. C., 1995. The soft gamma repeaters as very strongly magnetized neutron stars - I. Radiative mechanism for outbursts. *MNRAS*, **275**, 255–300.

Thompson, T. A., 2011. Accelerating Compact Object Mergers in Triple Systems with the Kozai Resonance: A Mechanism for "Prompt" Type Ia Supernovae, Gamma-Ray Bursts, and Other Exotica. *ApJ*, **741**, 82.

Timmes, F. X. & Swesty, F. D., 2000. The Accuracy, Consistency, and Speed of an Electron-Positron Equation of State Based on Table Interpolation of the Helmholtz Free Energy. *ApJS*, **126**, 501–516.

Timokhin, A. N., 2006. On the force-free magnetosphere of an aligned rotator. *MNRAS*, **368**, 1055–1072.

Tornambé, A. & Piersanti, L., 2013. Pre-explosive observational properties of Type Ia supernovae. *MNRAS*, **431**, 1812–1822.

Toropina, O. D., Romanova, M. M. & Lovelace, R. V. E., 2012. Bondi-Hoyle accretion on to a magnetized neutron star. *MNRAS*, **420**, 810–816.

Torres, S., García-Berro, E., Burkert, A. & Isern, J., 2002. High-proper-motion white dwarfs and halo dark matter. *MNRAS*, **336**, 971–978.

Tout, C. A., Wickramasinghe, D. T., Liebert, J., Ferrario, L. & Pringle, J. E., 2008. Binary star origin of high field magnetic white dwarfs. *MNRAS*, **387**, 897–901.

Trümper, J. E., Zezas, A., Ertan, Ü. & Kylafis, N. D., 2010. The energy spectrum of anomalous X-ray pulsars and soft gamma-ray repeaters. *A&A*, **518**, A46.

Tsebrenko, D. & Soker, N., 2015a. MNRAS, in press.

Tsebrenko, D. & Soker, N., 2015b. MNRAS, submitted.

Tutukov, A. V. & Fedorova, A. V., 2010. Possible scenarios for the formation of Ap/Bp stars. *Astronomy Reports*, **54**, 156–162.

Usov, V. V., 1993. High-frequency emission of X-ray pulsar 1E 2259+586. *ApJ*, **410**, 761–763.

Valenti, S., Yuan, F., Taubenberger, S., Maguire, K., Pastorello, A. et al., 2014. PESSTO monitoring of SN 2012hn: further heterogeneity among faint Type I supernovae. *MNRAS*, **437**, 1519–1533.

Valyavin, G. & Fabrika, S., 1999. White dwarfs magnetic fields evolution. In S.-E. Solheim & E. G. Meistas, eds., *11th European Workshop on White Dwarfs*, vol. 169 of *Astronomical Society of the Pacific Conference Series*, 206.

van Kerkwijk, M. H., Chang, P. & Justham, S., 2010. Sub-Chandrasekhar White Dwarf Mergers as the Progenitors of Type Ia Supernovae. *ApJ*, **722**, L157–L161.

van Paradijs, J., Taam, R. E. & van den Heuvel, E. P. J., 1995. On the nature of the 'anomalous' 6-s X-ray pulsars. *A&A*, **299**, L41.

Vassiliadis, E. & Wood, P. R., 1993. Evolution of low- and intermediate-mass stars to the end of the asymptotic giant branch with mass loss. *ApJ*, **413**, 641–657.

Vrtilek, S. D., Raymond, J. C., Garcia, M. R., Verbunt, F., Hasinger, G. & Kurster, M., 1990. Observations of Cygnus X-2 with IUE - Ultraviolet results from a multiwavelength campaign. *A&A*, **235**, 162–173.

Wagoner, R. V., 1969. Synthesis of the Elements Within Objects Exploding from Very High Temperatures. *ApJS*, **18**, 247.

Wahlquist, H., 1987. The Doppler response to gravitational waves from a binary star source. *General Relativity and Gravitation*, **19**, 1101–1113.

Wang, B. & Han, Z., 2012. Progenitors of type Ia supernovae. *NewAR*, **56**, 122–141.

Wang, Z., Chakrabarty, D. & Kaplan, D. L., 2006. A debris disk around an isolated young neutron star. *Nature*, **440**, 772–775.

Webbink, R. F., 1984. Double white dwarfs as progenitors of R Coronae Borealis stars and Type I supernovae. *ApJ*, **277**, 355–360.

Wells, L. A., Phillips, M. M., Suntzeff, B., Heathcote, S. R., Hamuy, M. et al., 1994. The Type IA supernova 1989B in NGC 3627 (M66). *AJ*, **108**, 2233–2250.

Wendell, C. E., van Horn, H. M. & Sargent, D., 1987. Magnetic field evolution in white dwarfs. *ApJ*, **313**, 284–297.

Whelan, J. & Iben, J. I., 1973. Binaries and Supernovae of Type I. *ApJ*, **186**, 1007–1014.

Wickramasinghe, D. T. & Ferrario, L., 2000. Magnetism in Isolated and Binary White Dwarfs. *Publications of the Astronomical Society of the Pacific*, **112**, 873–924.

Willems, B., Kalogera, V., Vecchio, A., Ivanova, N., Rasio, F. A., Fregau, J. M. & Belczynski, K., 2007. Eccentric Double White Dwarfs as LISA Sources in Globular Clusters. *ApJ*, **665**, L59–L62.

Yamanaka, M., Kawabata, K. S., Kinugasa, K., Tanaka, M., Imada, A. et al., 2009. Early Phase Observations of Extremely Luminous Type Ia Supernova 2009dc. *ApJ*, **707**, L118–L122.

Yoon, S.-C. & Langer, N., 2004. Presupernova evolution of accreting white dwarfs with rotation. *A&A*, **419**, 623–644.

Yoon, S.-C. & Langer, N., 2005. On the evolution of rapidly rotating massive white dwarfs towards supernovae or collapses. *A&A*, **435**, 967–985.

Yoon, S.-C., Podsiadlowski, P. & Rosswog, S., 2007. Remnant evolution after a carbon-oxygen white dwarf merger. *MNRAS*, **380**, 933–948.

Zanotti, O., Rezzolla, L. & Font, J. A., 2003. Quasi-periodic accretion and gravitational waves from oscillating 'toroidal neutron stars' around a Schwarzschild black hole. *MNRAS*, **341**, 832–848.

Zorotovic, M., Schreiber, M. R., Gänsicke, B. T. & Nebot Gómez-Morán, A., 2010. Post-common-envelope binaries from SDSS. IX: Constraining the common-envelope efficiency. *A&A*, **520**, A86.